Structural and Superconducting Properties of High-Tc Superconductors

Frello, Thomas

Publication date:
2000

Document Version
Publisher's PDF, also known as Version of record

Risø–R–1086(EN)

Structural and Superconducting Properties of High-T_c Superconductors

Thomas Frello

Risø National Laboratory, Roskilde, Denmark
January 2000

Abstract The structural and superconducting properties of high-T_c compounds are investigated by use of hard x-ray diffraction and neutron diffraction, magneto-optical imaging, susceptibility measurements and gas volumetric sample preparation. The systems studied are single crystal samples of $ReBa_2Cu_3O_{6+x}$ and $La_{2-x-y}Re_ySr_xCuO_4$ (Re=Rare Earth element), and Ag-clad $Bi_2Sr_2Ca_2Cu_3O_{10+x}$ tapes for power transmission applications.

The four major topics covered are:

1. **Oxygen ordering in the $ReBa_2Cu_3O_{6+x}$ system**
   The ordering of the oxygen atoms in the basal plane of $ReBa_2Cu_3O_{6+x}$ has profound influence on the superconducting properties. The work presented in this thesis represents the most systematic study performed so far of the oxygen superstructure formation in $YBa_2Cu_3O_{6+x}$ (YBCO) as function of oxygen concentration x and temperature. High-purity single crystals have been prepared to oxygen concentrations in the superconducting orthorhombic distorted state. Dopings from $0.35 \geq x \geq 0.87$ are investigated. The dynamic behavior of the dominant ortho-II superstructure phase is studied over time periods ranging from seconds to months, and we demonstrate that dynamical scaling applies to the superstructure formation. A highly unusual YBCO sample with $x = 0.62$ and an anomalous tetragonal symmetry is characterized by x-ray diffraction and magneto-optical imaging, and we find that it is bulk superconducting.
   Oxygen ordering has also been investigated for other systems with Re=La,Nd. For nonsuperconducting $NdBa_2Cu_3O_{6+x}$ with $x = 0.5$ we observe a mixture of several oxygen superstructures coexisting in the same sample. The configurations are of a nature that cannot give rise to charge transfer and the observations are consistent with the different $T_c(x)$ dependence for $YBa_2Cu_3O_{6+x}$ and $NdBa_2Cu_3O_{6+x}$.

2. **Flux turbulence in $ReBa_2Cu_3O_{6+x}$**
   By magneto-optical imaging turbulent features of the boundary zone dividing flux of opposite polarity has been observed in high-quality single crystals of YBCO. We demonstrate the existence of flux turbulence in underdoped YBCO and near-optimally doped $NdBa_2Cu_3O_{6+x}$ single crystals. It is shown that the temperature for which the turbulence is maximum scales with T_c and that the chemical purity is important for the turbulent behavior. A number of materials parameters like critical current density, electrical anisotropy and oxygen ordering have only little or no influence on the turbulence. There are indications that a sample in the turbulent state displays incomplete flux shielding behavior.

3. **Stripe phases in nickelates and cuprates**
   Anomalous suppression of superconductivity occurs in $La_{2-x}Ba_xCuO_4$ and $La_{2-x-y}Nd_ySr_xCuO_4$ when the hole doping (Ba,Sr content) is close to 1/8. Neutron scattering experiments indicate that at low temperatures charges and spins order in stripes similar to what is seen in nickelates. We have investigated the scattering associated with charge ordering with hard x-rays, and in $La_{1.775}Sr_{0.225}NiO_4$ and $La_{1.6-x}Nd_{0.4}Sr_xCuO_4$ with $x = 0.12$ we find reflections consistent with the neutron data. Weak charge scattering is also observed in $La_{1.6-x}Nd_{0.4}Sr_xCuO_4$ with $x = 0.15$, and for the cuprates additional information on the stripe symmetry transverse to the CuO_2 planes is obtained, and next- nearest-neighbor-plane correlations are observed. In Eu-doped $La_{1.68-x}Eu_{0.2}Sr_{0.12}CuO_4$ surprisingly strong superstructure reflections are observed at the positions expected for charge ordering peaks. The reflections are essentially temperature-independent and of unknown origin.

4. **Phase development and texture formation in BSCCO/Ag tapes**
   The solid state chemical reactions and microstructural changes taking place in the ceramic core of Ag-clad BSCCO tapes during annealing are monitored *in-situ* using hard x-ray diffraction. We observe that the texture of the Bi-2212 phase begins to improve already during the initial heating and that the final texture of the 2212 and 2223 phases are identical. The phase transformation involves the secondary phases $(Ca,Sr)_2PbO_4$, $(Ca,Sr)_2CuO_3$, the 3321 and 2201 phase and a liquid phase which appears during annealing. We observe no finite-size broadening of the 2212 phase reflections during the transformation process, and this is discussed in relation to various transformation mechanisms.
   Magneto-optical imaging is combined with hard x-ray diffraction to investigate the influence of the thermomechanical processing steps on the overall tape performance. The magneto-optical results show how defect structures play a major role as a current limiting factor. The major importance of additional thermomechanical processing steps is to improve the grain connectivity.

The scope of this thesis has been rather broad, dealing with studies of selected aspects in a variety of systems rather than focusing on exhaustive investigations of one single system. The thesis consists of a basic text and eight papers attached at the end. This division does not represent a difference in involvement of the different subjects, but merely that the topics described only in the text part have been studied so recently that they have not yet been written in a form suitable for publication. I recommend that text and papers are not read separately but that a paper is read the first time it is mentioned in the main text. Especially the information in papers 1,3,5 and 6 is a prerequisite to appreciate the content following in the main text.

The experiments have been performed at Risø National Laboratory (Denmark), at the HASYLAB synchrotron facility in Hamburg (Germany) and at University of Oslo (Norway). Some additional studies were performed at Brookhaven National Laboratory (USA). The thesis constitutes part of the requirement for obtaining the Ph.D. degree at the Technical University of Denmark. My supervisor at Risø was senior scientist Niels Hessel Andersen and my formal supervisor at the Technical University of Denmark was associate professor Jakob Weiland Høj. My Ph.D. study was financed by a grant from the Danish Technical Research Council.

Resumé Strukturelle og superledende egenskaber af høj-T_c superledere er undersøgt ved anvendelse af højenergi røntgendiffraktion med synkrotronstråling med en fotonenergi på 100 keV og neutron diffraktion, magneto-optisk afbildning, susceptibilitetsmålinger og gasvolumetrisk prøvepræparation. De studerede systemer er énkrystaller af $ReBa_2Cu_3O_{6+x}$ og $La_{2-x-y}Re_ySr_xCuO_4$ (Re=sjælden jordart), og $Ag/Bi_2Sr_2Ca_2Cu_3O_{10+x}$ tapes til strømtransport applikationer.

De fire hovedemner som er studeret omhandler:

1. **Iltorden i $ReBa_2Cu_3O_{6+x}$ systemet**
   Den spontane orden af iltatomerne i basalplanet af $ReBa_2Cu_3O_{6+x}$ har afgørende indflydelse på de superledende egenskaber. Resultaterne som præsenteres i denne afhandling udgør det hidtil mest systematiske studie af iltsuperstruktur dannelse i $YBa_2Cu_3O_{6+x}$ (YBCO) som funktion af iltindhold x og temperatur. Énkrystaller af høj kemisk renhed er blevet præpareret til iltindhold i den superledende orthorombiske tilstand. Iltindhold fra $0.35 \geq x \geq 0.87$ er blevet undersøgt. Den dynamiske opførsel af den dominerende ortho-II superstruktur fase er blevet studeret på tidsskalaer som strækker sig fra sekunder til måneder, og vi viser at superstruktur dannelsen følger en dynamisk skalering. En højst usædvanlig YBCO krystal med $x = 0.62$ og en anomal tetragonal symmetri er blevet karakteriseret med røntgendiffraktion og magneto-optisk afbildning, og vi finder at den er bulk superledende.
   Iltorden i andre systemer med Re=La,Nd er også blevet undersøgt. For ikkesuperledende $NdBa_2Cu_3O_{6+x}$ med $x = 0.5$ observerer vi en blanding af adskillige ilt-superstrukturer i den samme prøve. Konfigurationerne af iltatomerne er af en type som ikke kan give anledning til ladningsoverførsel, og observationerne forklarer hvorfor $T_c(x)$ afhængigheden er forskellig for $YBa_2Cu_3O_{6+x}$ and $NdBa_2Cu_3O_{6+x}$.

2. **Fluks turbulens i $ReBa_2Cu_3O_{6+x}$**
   Ved hjælp af magneto-optisk afbildning kan man i højkvalitets YBCO énkrystaller observere turbulent opførsel af den zone som afgrænser områder med magnetisk fluks af modsat polaritet. Vi påviser at fluks turbulens eksisterer i underdopet YBCO og i $NdBa_2Cu_3O_{6+x}$ énkrystaller nær optimal doping. Vi finder at den temperatur hvor turbulensen er maksimal skalerer med T_c og at den kemiske renhed er vigtig for turbulensen. Materialeegenskaber som kritisk strømtæthed, elektrisk anisotropi og iltorden har kun lille eller slet ingen indflydelse på turbulensen. Der er indikationer af at en prøve i den turbulente tilstand ikke kan afskærme et ydre felt perfekt.

3. **Stribe faser i nikkelater og kuprater**
   I $La_{2-x}Ba_xCuO_4$ og $La_{2-x-y}Nd_ySr_xCuO_4$ optræder der en anomal undertrykkelse af superledningen når hul-dopningsgraden (Ba,Sr indholdet) er nær 1/8. Neutronsprednings målinger peger på at ladninger og spin ordner sig i striber som man ser det i nikkelaterne. Ved hjælp af højenergi røntgendiffraktion har vi undersøgt spredning relateret til ladningsorden, og i $La_{1.775}Sr_{0.225}NiO_4$ og $La_{1.6-x}Nd_{0.4}Sr_xCuO_4$ med $x = 0.12$ finder vi reflektioner som er konsistente med neutronmålingerne. Svage diffraktionsmønstre fra ladningsordningen ses også i $La_{1.6-x}Nd_{0.4}\ Sr_xCuO_4$ med $x = 0.15$. For kupraterne får vi desuden ny information om symmetrien af ladningsstriberne vinkelret på CuO_2 planerne, hvor vi observerer korrelationer mellem de næstnærmeste naboplaner. I Eu-dopet $La_{1.68-x}Eu_{0.2}Sr_{0.12}CuO_4$ finder vi overraskende kraftige superstruktur reflektioner ved de forventede positioner for ladningsspredning. Reflektionerne er stort set uafhængige af temperaturen og af ukendt oprindelse.

4. **Fase transformationer og teksturudvikling i BSCCO/Ag tapes**
   De faststofkemiske reaktioner og mikrostrukturelle ændringer som finder sted i den keramiske kerne af Ag/BSCCO tapes under varmebehandling er blevet undersøgt *in-situ* ved hjælp af højenergi røntgendiffraktion. Observationerne viser at der sker en forbedring af teksturen af 2212 fasen allerede under opvarmningen, og at den endelige tekstur af 2212 og 2223 faserne er identiske. Fase transformationerne involverer de sekundære faser $(Ca,Sr)_2PbO_4$, $(Ca,Sr)_2CuO_3$, 3321 og 2201 samt en flydende fase som viser sig i løbet af varmebehandlingen. Der optræder ingen størrelsesforbredring af 2212 fase reflektionerne under fasetransformationen, og dette diskuteres i relation til forskellige transformations mekanismer.
   Indflydelsen af de termomekaniske bearbejdningstrin på strømtransport egenskaberne er blevet undersøgt ved at kombinere magneto-optisk afbildning og højenergi røntgendiffraktion. De magneto-optiske resultater viser at defektstrukturer er en af de betydeligste strømbegrænsende faktorer. Hovedindflydelsen af ekstra trin i den termomekaniske bearbejdning er en forbedring af den elektriske kobling mellem de superledende korn.

Denne afhandling dækker en forholdsvis bred emnekreds med studier af udvalgte aspekter af forskellige systemer snarere end et udtømmende studie af et enkelt system. Afhandlingen består af en grundtekst og otte vedlagte artikler. Denne opdeling er ikke en repræsententation af i hvor høj grad jeg har været involveret i de forskellige emner, men blot at de emner som kun er omtalt i hovedteksten er studeret så nyligt, at de endnu ikke er blevet nedfældet i en form som er velegnet til publikation i et tidsskrift. Jeg anbefaler at teksten og artiklerne ikke læses separat, men at en artikel læses første gang den nævnes i hovedteksten. Specielt artiklerne 1,3,5 og 6 indeholder information som er nødvendig for at få det fulde udbytte af det efterfølgende indhold i hovedteksten.

Eksperimenterne er foretaget på Forskningscenter Risø (Danmark), ved HASYLAB synkrotronen i Hamborg (Tyskland) og ved Oslo Universitet (Norge). Nogle supplerende studier blev foretaget ved Brookhaven National Laboratory (USA). Afhandlingen udgør en del af kravet for at opnå en Ph.D. grad ved Danmarks Tekniske Universitet DTU. Vejleder på Risø har været seniorforsker Niels Hessel Andersen og formel vejleder på DTU har været lektor Jakob Weiland Høj. Mit Ph.D. stipendium er financieret af Statens Teknisk-Videnskabelige Forskningsråd.

ISBN 87–550–2476–9
ISBN 87–550–2477–7 (internet)
ISSN 0106–2840

Information Service Department · Risø · 2000

Contents

1 Introduction

There are few absolutes in physics. Most concepts and ideas are approximations, often excellent, but rarely something you would claim to be absolutely exact. But the state of absolute zero resistance does exist. It is even a common thing: more than half of the metallic elements in the periodic table are superconductors [1], and superfluidity occurs in liquid Helium. When high-temperature superconductivity was discovered in 1986 By Bednorz and Müller [2] the superconducting state became both more exotic and at the same time opened for an everyday occurrence. *Exotic* because high-T_c superconductivity challenges our understanding of the otherwise well-established phenomena of superconductivity [3] and metallic behavior, and *everyday occurrence* because the high transition temperatures open for technological applications on a scale that could never be achieved by the low-temperature superconductors.

Due to the fascinating scientific challenges and application perspectives of high-T_c superconductivity, enormous efforts have been directed towards high-T_c research from the moment this new category of solids appeared. The main research efforts have gradually shifted away from transition temperature to current density; as the condensation of electron pairs into a superconducting state is a second-order phase transition, a superconductor will have to be cooled significantly below T_c in order to achieve an useful current-carrying capacity. Until a T_c considerably higher than room temperature is more than science-fiction [4], most work will be focused on the critical current density at liquid nitrogen temperatures or lower.

This thesis describes studies of structure and superconductivity of high-T_c materials. The basic properties of model systems and application materials have been investigated. The model systems were high-quality single crystal samples, and the applied system was superconducting tapes. The thesis consists of a basic text and eight attached papers. I recommend that text and papers are not read separately but that a paper is read the first time it is mentioned in the main text. Especially the information in papers 1,3,5 and 6 is a prerequisite to appreciate the content following in the basic text.

1.1 High-T_c superconductors

The parent compound for the high-T_c superconductors is the antiferromagnetic insulator La_2CuO_4. Replacing La^{3+} by Sr^{2+} or Ba^{2+} will introduce holes into the CuO_2 planes, thereby making the compound metallic and, eventually, superconducting. It is also possible to make an electron doped high-T_c superconductor by substituting La^{3+} with e.g. Ce^{4+}, but most high-T_c compounds are hole-doped.

Two major pending questions in the field of creating a microscopic theory for high-T_c superconductivity is the coupling mechanism responsible for creating Cooper pairs in the CuO_2 planes, and the mechanism responsible for the charge transfer from the charge reservoir units into the CuO_2 planes. Many theories dealing with these topics have appeared right from the emergence of high-temperature superconductivity, but there is not yet a consensus in the scientific community on one single theory. Maybe the correct explanation that can account for all the phenomena observed in the cuprates can be found in one of the many theories that have been constructed over the last decade, but the general picture is blurred by strong variations from one compound to another. Many of these individual differences arise from major or minor variations in the structural properties of the high-T_c compounds.

The "canonical" phase diagram is shown in Fig. 1 for $La_{2-x}Sr_xCuO_4$ (La-214), showing the transition from a 3D antiferromagnetic insulator to a quasi-2D metal-

lic superconductor by increasing hole doping. As seen in the figure T_c reaches a maximum around $x = 0.15$ which is called *optimal doping*, while lower or higher Sr-contents are referred to as the *underdoped* and *overdoped* region, respectively. This phase diagram gives the basic features of high-temperature superconductivity, but closer inspection of other high-T_c compounds quickly reveals a vast variety of modifications to the canonical behavior. For example, merely replacing Sr with Ba as dopant will significantly alter both the electronic and structural properties. this will be discussed in more detail in chapter 5.

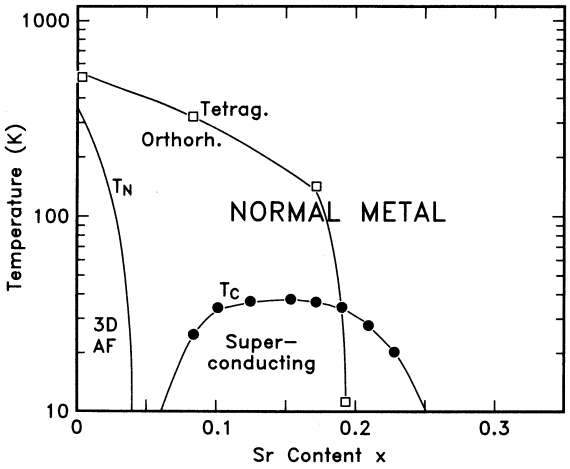

Figure 1. Schematic phase diagram of the electronic and structural variations with x in the parent high-T_c compound $La_{2-x}Sr_xCuO_4$. Néel Temperature (T_N), superconducting transition temperature (T_c). From Ref. [5]

The superconducting properties are intimately related to the crystal structure in all the high-T_c compounds, and a proper understanding of the fascinating phenomenon of high-T_c superconductivity cannot be obtained without a rather detailed knowledge of the material's structure.

1.2 Flux penetration in superconductors

Superconductivity and magnetism are generally considered mutually exclusive phenomena. A magnetic field will induce superconducting currents running in such a way as to screen off the external field and keep the interior free of magnetic flux. Superconductors do not only display such a flux shielding behavior that would be expected for a conductor of zero resistance. When they are cooled below the critical transition temperature any field already present in the superconductor will be expelled - a sign that a superconductor is not the same as a perfect conductor. With respect to the magnetic shielding properties two categories of superconductors exist - Type-I and Type-II. A Type-I superconductor will totally exclude an external field until it reaches a critical value H_c, whereafter superconductivity will break down. This is called the *Meissner-Ochsenfeld* effect. In a Type-II superconductor there is a similar exclusion of low fields up to a critical value H_{c1}. When the field is further increased it will begin to penetrate as quantized flux lines (also called vortices), each surrounded by a circulating supercurrent and each carrying a flux quanta Φ of value $\Phi = \frac{h}{2e}$ with h being Planck's constant and $2e$ the charge of a Cooper pair. This is called the *mixed state* or *vortex state*. This state exists until the field reaches another critical value H_{c2} whereafter the sample enters the normal state. The magnetic phase diagram for a Type-II superconductor is shown

schematically in Fig. 2.

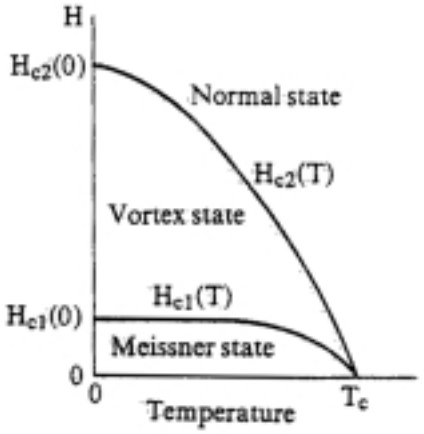

Figure 2. Magnetic phase diagram of a Type-II superconductor.

If the flux lines are free to move in the superconductor they will arrange to form a two-dimensional Flux-Line-Lattice (FLL) of hexagonal symmetry known as the *Abrikosov Lattice*. In anisotropic superconducting materials however, the FLL can assume very exotic symmetries [6]. Spatial variations in the density of superconducting electrons can be treated by the Ginzburg-Landau theory [7], which is a phenomenological theory of superconductivity based on Landau's theory on second-order phase transitions. The Ginzburg-Landau parameter κ is defined as $\kappa \equiv \lambda/\xi$ where ξ is the superconducting coherence length and λ the magnetic penetration depth. Abrikosov showed [8] that for $\kappa < 1/\sqrt{2}$ the superconductor will be Type-I and for $\kappa > 1/\sqrt{2}$ it will be Type-II. Most low-T_c superconductors have values $\lambda \sim 500$Å and $\xi \sim 4000$Å, and they are Type-I. The high-T_c superconductors have extremely short coherence lengths, $\xi \sim 10$Å, and they are all Type-II.

Flux-Line-Lattice melting, pinning and j_c

When a current flows in a Type-II superconductor in the mixed state the flux lines present will experience a Lorentz force. If the Lorentz force is sufficiently strong to make the flux lines move it will cause energy dissipation resulting in an effective resistance. Avoiding this *flux flow state* is a key issue for application purposes, as it governs the critical current density j_c of the material. The flux lines can be *pinned* by potential barriers where the superconductivity is suppressed or destroyed on the same length scale as a single flux line. Here the ability to form a rigid FLL is essential: if all the flux lines are acting as a magnetic solid in principle only two pinning centers are needed to avoid flux flow. If the flux lines move rather independently of each other we have something more resembling a magnetic liquid, and in principle a pinning center for every flux line is required. At sufficiently high temperatures thermal excitations can "melt" the FLL and a crossover between a dissipation-free and resistive regime occurs. The FLL melting temperature can be very different for the various high-T_c compounds, depending especially on the anisotropy. For very anisotropic materials with $\xi_{ab} \gg \xi_c$ the coupling along the c-axis is weak and the flux lines tend to form a disordered 3D "pancake" structure

Try to pin an amount of H_2O above and below 273K using two nails, and the difference is quite evident

rather than a 2D columnar structure.

1.3 The Bean model

A simple but useful model that describes flux penetration in Type-II superconductors was introduced by Bean [9, 10]. It assumes that there is always pinning present, intrinsically or in form as pinning centers, and that the flux lines thus experience a force preventing them from freely entering the interior of the superconductor. The Bean critical state model further assumes that the shielding currents induced by the external field will have the critical current density j_c. According to this the critical current density can be found from the slope of the penetrating field using Maxwell's equations:

$$\mu_0 j_c(B) = \frac{\mathrm{d}B}{\mathrm{d}x} \tag{1.1}$$

where $\mathrm{d}B$ is the difference in magnetic induction over the distance $\mathrm{d}x$ from the surface of a planar superconductor. j_c can be determined by DC magnetization from the width of the hysteresis loop ΔM or from the slope $\frac{\mathrm{d}B}{\mathrm{d}x}$ measured by Hall probes or magneto-optical imaging (cf. Fig. 3 and section 2.4). For magnetization measurements a knowledge of the sample dimensions is required to determine an intrinsic value of j_c [11] and, depending on sample geometry, demagnetization factors may have a significant influence on the field profile, e.g. for thin films.

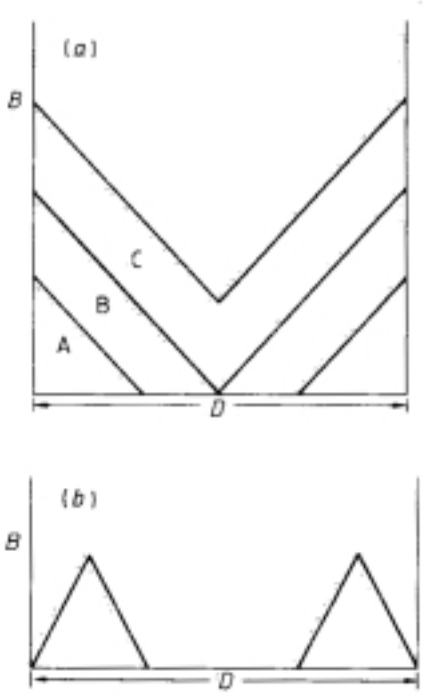

Figure 3. (a) Profiles of the magnetic induction B in a Type-II superconductor in a specimen taken as a slab of thickness D placed in a parallel applied field. A,B and C represent the profile across the sample for increasing fields. (b) Profile after the applied field has been first increased and then decreased to zero (remanent state).

Qualitatively the assumption of the Bean model is that the field is always penetrating from the edges; the supercurrents run to shield the interior from the external fields.

2 Experimental techniques and apparatus used

The main part of the structural investigations described in this thesis was performed by scattering experiments with high-energy synchrotron x-ray diffraction. For some additional experiments neutron diffraction was used. A gas volumetric oxidation technique was used to control the oxygen concentration of the single crystals. The superconducting properties were investigated by magneto-optical imaging and susceptibility measurements. The techniques and apparatus will be described in the following.

2.1 Diffraction studies

A major part of the experimental investigations were made with either x-ray diffraction or neutron diffraction. If the wavelength of the radiation is comparable to the interatomic distances in solid matter, the crystal structure can be investigated by scattering techniques. The basis of diffraction is the famous Bragg equation:

$$\mathrm{n}\lambda = 2d\sin\theta \tag{2.1}$$

with λ being the wavelength of the neutron/x-ray beam, d the spacing between the lattice planes, θ the Bragg angle and n an integer number. The scattered radiation will be observed at the angle 2θ with respect to the incoming beam. For powder diffraction studies where the sample investigated consists of a great number of randomly oriented crystallites the scattered radiation will be distributed on the so-called Debye-Scherrer cone. For single crystal studies another and often more useful way of expressing the scattering is normally used. It is based on the concept of the *reciprocal lattice*. If the three lattice vectors of the unit cell in direct space are given by $\boldsymbol{a}, \boldsymbol{b}$ and $\boldsymbol{c}$ the reciprocal lattice vectors are defined as

$$\boldsymbol{a}^* = 2\pi\frac{\boldsymbol{b}\times\boldsymbol{c}}{V} \tag{2.2}$$

$$\boldsymbol{b}^* = 2\pi\frac{\boldsymbol{c}\times\boldsymbol{a}}{V} \tag{2.3}$$

$$\boldsymbol{c}^* = 2\pi\frac{\boldsymbol{a}\times\boldsymbol{b}}{V} \tag{2.4}$$

where $V = \boldsymbol{a}\cdot\boldsymbol{b}\times\boldsymbol{c}$ is the unit cell volume. The wave vector $\boldsymbol{k}$ and the reciprocal lattice vector $\boldsymbol{\tau}$ are defined as $\boldsymbol{k} = 2\pi/\lambda$ and $\boldsymbol{\tau} = 2\pi/d$. Using these definitions scattered radiation in the outgoing direction $\boldsymbol{k_s}$ is observed when the scattering vector $\boldsymbol{\kappa} \equiv \boldsymbol{k_i} - \boldsymbol{k_s}$ is equal to a reciprocal lattice vector $\boldsymbol{\tau}$ as depicted in Fig. 4. This statement can be elegantly written as

$$\boldsymbol{\kappa} = h\boldsymbol{a}^* + k\boldsymbol{b}^* + l\boldsymbol{c}^* \tag{2.5}$$

with h, k, l being integer numbers denoted the *Miller indices*. The limit of the number of reciprocal lattice points that can diffract incoming radiation is given by the length of the incoming wave vector $\boldsymbol{k_i}$ and the accessible scattering angle 2θ ($<180°$).

If the unit cell contains more than one atom the radiation scattered from the individual atoms within the unit cell can interfere to alter the intensity of the

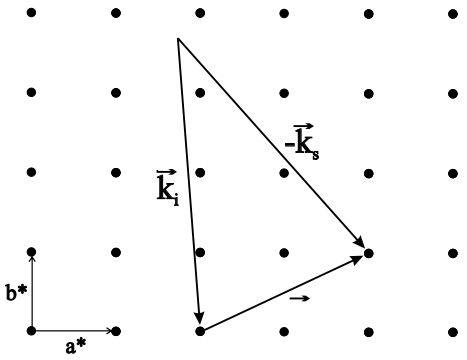

Figure 4. Constructive interference of scattered radiation occurs only if the scattering vector $\boldsymbol{\kappa} \equiv \boldsymbol{k_i} - \boldsymbol{k_s}$ equals a reciprocal lattice vector $\boldsymbol{\tau}$, here shown for the ab-plane. This is the so-called Ewald construction.

different reflections, and even to make them vanish. The structure factor F is given by

$$F = \sum_{n=1}^{m} b_n e^{i2\pi(hx_n+ky_n+lz_n)} \qquad \text{for neutrons} \tag{2.6}$$

$$F = \sum_{n=1}^{m} f_n e^{i2\pi(hx_n+ky_n+lz_n)} \qquad \text{for x-rays} \tag{2.7}$$

where x, y, z are the fractional coordinates of the atoms within the unit cell, b_n is the scattering length of the n'th atom, f_n is the atomic scattering factor of the n'th atom and the sum is over all atoms in the unit cell. Normally the scattered intensity is described by the differential scattering cross section $\frac{\mathrm{d}\sigma}{\mathrm{d}\Omega}$ giving the number of scattered neutrons/photons into the solid angle $\mathrm{d}\Omega$ per second, divided by the incoming neutron/photon flux. This is written as

$$\frac{\mathrm{d}\sigma}{\mathrm{d}\Omega} = NV^* \sum_{\tau} |F(\boldsymbol{\tau})|^2 \delta(\boldsymbol{\kappa} - \boldsymbol{\tau}) \tag{2.8}$$

Here N is the total number of scatterers and V^* is the reciprocal unit cell volume.

The diffraction pattern can also be regarded as a Fourier transform of the scattering density ρ, in which the Fourier coefficients are the structure factors F_{hkl}:

$$\rho(x,y,z) = \frac{1}{V} \sum_h \sum_k \sum_l F_{hkl} \mathrm{e}^{-2\pi i[h(x/a)+k(y/b)+l(z/c)]} \tag{2.9}$$

Unfortunately the structure in direct space cannot be solved directly from equation (2.9) because in a diffraction experiment we have access only to a limited number of $|F_{hkl}|$, and since we measure $|F_{hkl}|^2$ the information of the phases are lost. Additional information of the system studied is often required to unambiguously solve the structure.

Peak shape

In equation (2.8) the scattered signal is described as infinitely sharp delta functions centered at the reciprocal lattice points. This is a good approximation when the number of coherently scattering elements is large, but if the number is small the delta function should be replaced with

For the oxygen superstructures studied here the correlation lengths are always limited

$$\frac{\sin^2 \frac{N_a}{2}\boldsymbol{\kappa}\cdot\boldsymbol{a}}{\sin^2 \frac{1}{2}\boldsymbol{\kappa}\cdot\boldsymbol{a}} \times \frac{\sin^2 \frac{N_b}{2}\boldsymbol{\kappa}\cdot\boldsymbol{b}}{\sin^2 \frac{1}{2}\boldsymbol{\kappa}\cdot\boldsymbol{b}} \times \frac{\sin^2 \frac{N_c}{2}\boldsymbol{\kappa}\cdot\boldsymbol{c}}{\sin^2 \frac{1}{2}\boldsymbol{\kappa}\cdot\boldsymbol{c}} \tag{2.10}$$

If we, as an example, only consider scattering along the a-axis, the function peaks for all $\boldsymbol{\kappa}\cdot\boldsymbol{a} = 2\pi h$ with h an integer number, corresponding to the reciprocal lattice points. The peak value is proportional to N_a^2 and the FWHM $\Delta h = \frac{\sqrt{6}}{N_a a}$ is inversely proportional to the domain size $N_a a$.

The peak shape depends on the nature of the correlations. For example an exponentially decaying correlation, as in the critical scattering region, will give a Lorentzian peak shape [12]. By measuring the peak shape and width we obtain information on the correlation lengths and the nature of the correlations involved. These properties can be highly anisotropic when measured along the different symmetry axes.

Basic properties of neutrons and photons

The basic scattering mechanisms described above are exactly the same for neutrons and x-rays. There are differences arising from the nature of the neutron and the photon: while both thermal neutrons and x-rays have the short wavelength in common, the neutrons scatter from the nuclei through the short range ($\sim 10^{-12}$ cm) weak nuclear interactions, and the x-rays scatter from the electron cloud surrounding the atoms. This difference is seen in equations (2.6) and (2.7). The neutron scattering cross section consists of a coherent and an incoherent part, originating from a mixture of different isotopes and from the spin states of the nucleus. The incoherent scattering is isotropic and gives rise to enhanced background radiation. There is only a coherent scattering contribution for x-rays, but the background signal is enhanced by Compton scattering and x-ray excited fluorescence.

The energies of thermal neutrons and x-rays are widely different. The neutron energy E_n, momentum p_n and wavelength λ_n are given by

$$E_n = \frac{\hbar^2 k^2}{2M_n} \qquad p_n = \hbar k \qquad \lambda_n = \frac{2\pi\hbar}{p_n} \tag{2.11}$$

while for the photon

$$E_p = \hbar\omega \qquad p_p = \frac{E_p}{c} = \frac{h}{\lambda} \qquad \lambda_p = \frac{hc}{E_p} \tag{2.12}$$

Thus, a wavelength of 1 Å corresponds to neutron energies of $E_n = 82$ meV and photon energies of $E_p = 1.24$ keV.

All x-ray scattering experiments described in this thesis were performed using very high photon energies of E_p=100 keV, corresponding to a wavelength of ≈0.1 Å. The high-energy photons and thermal neutrons both have a high penetration power and are therefore both bulk-probing techniques. The penetrating abilities also permit *in-situ* studies where the samples of interest can be placed in various environments such as furnaces or cryostats.

Spectrometers

The neutron scattering experiments were performed at the TAS1 triple-axis spectrometer at Risø National Laboratory research reactor DR3. The principle of the

triple-axis spectrometer is shown in Fig. 5. The incoming neutrons from the neutron source are monochromatized by a pyrolytic graphite monochromator. The angular spread of the neutrons incident on the sample is defined by collimators. The sample is centered on a rotation table, with the rotation angle denoted ω. The diffracted signal is scattered from the analyzer crystal, also made of pyrolytic graphite, before it is detected by a He^3 gas detector. If the angle of the analyzer crystal is the same as for the monochromator, only scattered neutrons with the same energy as the incoming neutrons will be reflected into the detector, i.e., we only measure the elastic scattering processes in the crystal. Since the energy of the thermal neutrons is of the same magnitude as that of the phonon processes typically taking place in solid (a few meV) the inelastic processes will change the momentum and wavelength of the neutron considerably, and the various energies can be analyzed by changing the angle of the analyzer crystal. This is a large and extremely interesting field in neutron scattering, but in this thesis only the elastic processes will be considered. For x-rays the photon energies are six to seven orders of magnitude larger than the phonon energies, and effectively one is always integrating over all energy transfers.

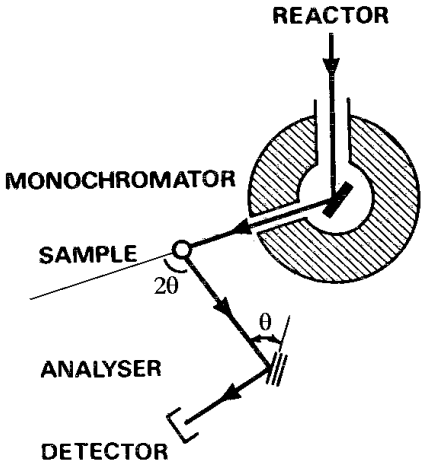

Figure 5. Schematic drawing of the triple-axis-spectrometer for neutron scattering. Collimators are inserted before and after the sample to define the beam direction.

X-ray scattering experiments were performed at the dedicated high-energy wiggler beamline BW5 at the HASYLAB synchrotron in Hamburg, Germany. The triple-crystal diffractometer is shown schematically in Fig. 6. A detailed description of the instrument can be found in Ref. [13]. For single crystal studies the sample was mounted on a Eulerian cradle (four-circle). The definition of the angles ω, ϕ, χ and 2θ is given in Fig. 7. By using the four-circle setup it is possible to quickly switch between different scattering planes without having to remount the sample. The highest resolution is obtained for scanning in the horizontal plane with a rotation of the ω and 2θ angles only.

The "analyzer" crystal used in triple-axis x-ray spectrometers only serves to improve the resolution. It has got nothing to do with analyzing inelastic scattering processes.

Instrumental resolution

The best resolution in reciprocal space is obtained in the nondispersive Laue (transmission) geometry, where the monochromator, sample and analyzer crystals have a perfect lattice match of the reflections chosen. In the dispersive geometry at least one of the crystals (typically the sample) scatters from a different lattice spacing. The resolution function of the triple axis spectrometer for high-energy

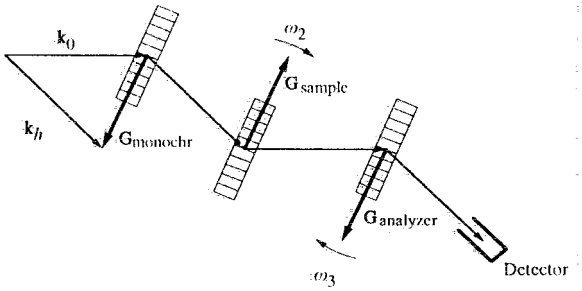

Figure 6. Schematic drawing of a triple-crystal diffractometer for high-energy synchrotron radiation. In reality, the Bragg angles are only of the order of 2°. The monochromator crystal diffracts the wavevector k_h out of the white incident beam. The sample can be rotated and tilted so that arbitrary scans through the scattering distribution in reciprocal space are possible. ω_1 represents the angle of rotation of the monochromator, ω_2 that of the sample (see also Fig. 7) and ω_3 that of the analyzer crystal. From Ref. [13].

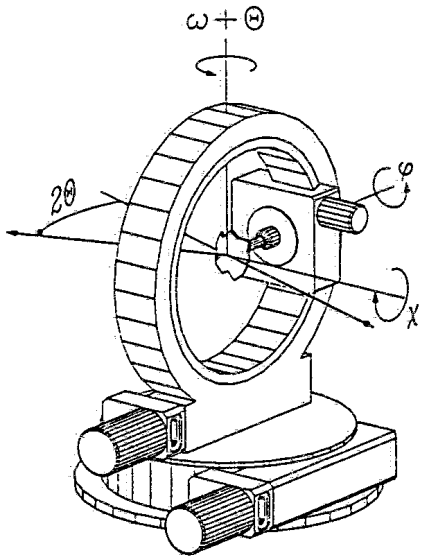

Figure 7. The Eulerian cradle (four-circle) for orientation of the sample in the scattering experiments. The angles ω, ϕ, χ and 2θ are defined as shown in the figure.

synchrotron radiation has been calculated for nondispersive Laue geometry by Neumann *et al.* [14] and for dispersive Laue geometry by Rütt *et al.* [15]. The resolution function was calculated numerically as it cannot be solved analytically. In the vertical plane the resolution is of the order 8×10^{-2} Å^{-1}, which is two to three orders of magnitude lower than in the horizontal scattering plane. The vertical resolution is normally defined by the opening of the vertical slit in front of the detector, and mostly this is set to integrate over the vertical intensity distribution of the peak of interest.

In the horizontal plane the resolution function is strongly asymmetric. For the nondispersive Laue geometry, where a perfect lattice match for the monochromator, sample and analyzer crystals is assumed, the optimum resolution is of the

order 10^{-4} Å^{-1} along the reciprocal lattice vector $\boldsymbol{\tau}$ (longitudinal direction) and 10^{-5} Å^{-1} perpendicular to $\boldsymbol{\tau}$ (transverse direction) using perfect Si crystals. This is because there is a large difference between the length of the wave vector $\boldsymbol{k} \approx 50$ Å^{-1} and the reciprocal lattice vector $\boldsymbol{\tau} \approx 2$ Å^{-1}. To a first approximation the resolution parallel to $\boldsymbol{\tau}$ is independent of the wavelength, but in the perpendicular direction it is proportional to λ. Accurate numerical calculations show that the resolution function actually is slightly star shaped, as shown in Fig. 8, but for most situations it is fully sufficient to consider the resolution to have an elongated "cigar" shape.

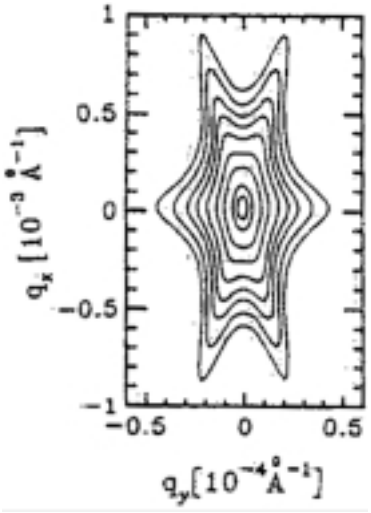

Figure 8. Intensity distribution of the Si(1 1 1) reciprocal lattice point calculated for 80 keV radiation diffracted from three perfect crystals in nondispersive Laue geometry. The peak intensity is normalized to 1, the contour levels are 0.8, 0.5, 0.2, 0.1, 0.05, 0.03, 0.02 and 0.0125. Note that the q_y scale perpendicular to $\boldsymbol{\tau}$ is stretched by a factor of ten. From Ref. [14].

In the dispersive setting where the lattice spacing of the sample differs from that of the monochromator and analyzer crystals the transverse resolution perpendicular to $\boldsymbol{\tau}$ is to a good approximation similar to the nondispersive case. The longitudinal resolution parallel to $\boldsymbol{\tau}$ is Lorentzian with a FWHM of

$$\Delta q_x \simeq 2|\boldsymbol{k}| \left| \frac{\sin(\theta_{\mathrm{M/A}} - \theta_{\mathrm{S}})}{\sin(\theta_{\mathrm{M/A}})} \right| \Delta_{\mathrm{div}} \tag{2.13}$$

where $\boldsymbol{k}$ is the wave vector, $\theta_{\mathrm{M/A}}$, θ_{S} is the Bragg angle of the monochromator/analyzer and sample respectively, and Δ_{div} is the FWHM of the angular distribution of the beam incident onto the monochromator. For the BW5 beamline the horizontal beam divergence onto the monochromator is well described by a Gaussian of FWHM 38″. For $\theta_{\mathrm{S}} \simeq \theta_{\mathrm{M/A}}$ equation (2.13) does not give the correct description of the main feature of the resolution function.

For the study of weak diffuse scattering, a high photon flux is more important than an optimum resolution. For these studies the choice of monochromator/analyzer crystals have been imperfect, mosaic crystals. This improves the photon flux by several orders of magnitude, but it also results in a large beam divergence and a greater $\Delta\lambda$. The imperfect monochromator/analyzer crystals used were either $SrTiO_3$ (2 0 0) or $Si/TaSi_2$ (1 1 1) [16] having a mosaic spread

of typically 60″, giving a longitudinal resolution of 0.0075 Å^{-1} and a transverse resolution of 0.002 Å^{-1}. The transverse resolution was normally limited by the sample mosaicity of 0.05 to 0.1°.

For the neutron scattering experiments described in this thesis a knowledge of the instrumental resolution was of less importance, and it will not be discussed here.

2.2 Gas volumetric oxygen preparations

A well-controlled preparation of the oxygen concentration of the $ReBa_2Cu_3O_{6+x}$ samples is of course essential for systematic studies of the oxygen phase diagram. A gas volumetric method was used, where the oxygen content of fully oxidized samples is reduced under equilibrium conditions, until the desired oxygen concentration is obtained [17]. The experimental setup consists of a vacuum system where the leak rate does not exceed $\approx 10^{-10}$ mole/hour. Three known volumes are connected, where the two are kept at fixed temperatures and the third is inserted into a high-temperature furnace. The setup is schematically shown in Fig. 9. If all pressure changes in the system are caused by a molar change of the O_2 content, the changes in oxygen stoichiometry Δx can be calculated from the ideal gas equation $PV = nRT$ as

$$\Delta p \cdot V = \frac{1}{2}\Delta x \cdot n_{\mathrm{YBCO}} \cdot R \cdot T \tag{2.14}$$

The equilibrium oxygen partial pressure versus temperature for a given oxygen concentration x is well-known for $YBa_2Cu_3O_{6+x}$ [18] and constitutes an independent check of the oxygen content.

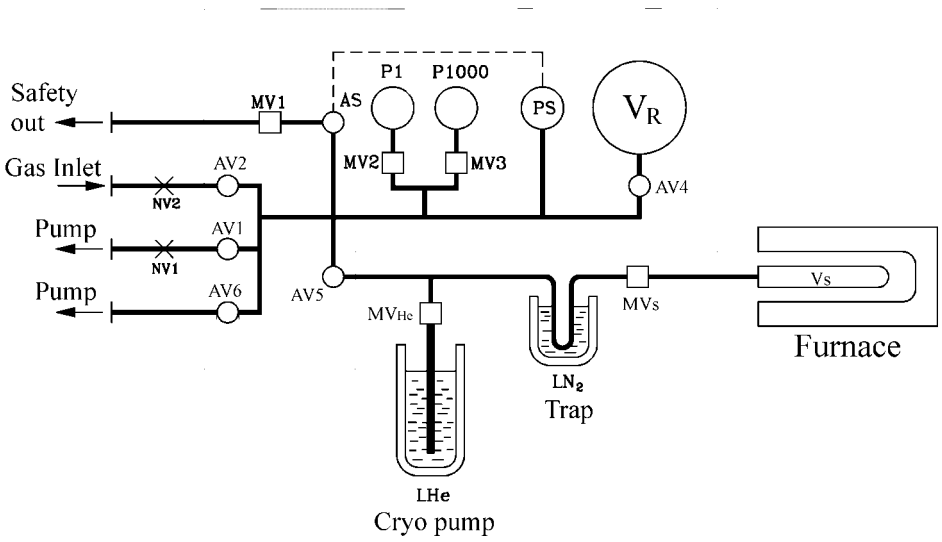

Figure 9. Gas volumetric setup used for controlling the oxygen concentration. The samples are contained in the volume $V_s \simeq 50$ cm^3 in a high-temperature furnace. $V_R \simeq 450$ cm^3 is a reference volume kept at a fixed temperature and the connecting vacuum tubes of volume $\simeq 200$ cm^3 are fixed at room temperature. Water vapor can be freezed out in the LN_2 trap. The pressure is monitored by the pressure gauges P1 and P1000. The LHe trap may be used to prepare fully reduced samples (not used in the work in this thesis).

As the single crystal samples available are typically only of 10 mg weight, an

exceedingly small pressure change in the furnace volume would correspond to a substantial change of oxygen concentration in the crystal. To better monitor and control the pressure changes several grams of pure YBCO powder were always used as buffer material, where it was assumed that the single crystal and the ceramic powder were in stoichiometric equilibrium at all time. As an example: for 10 mg YBCO a pressure change of 25 torr in the volume $V_R \simeq 450$ cm^3 at room temperature would correspond to $\Delta x = 0.08$.

During the oxygen preparations the crystals were always heated to above the orthorhombic-tetragonal transition and cooled at oxygen equilibrium pressures to room temperature. This will give the optimum conditions for obtaining an equal distribution of oxygen atoms throughout the sample, and for allowing the oxygen to form equilibrium superstructures.

Independent crystallographic determination [19] of the oxygen concentration for selected samples show that the accuracy of the gas volumetric preparations is $\Delta x \approx 0.02$.

2.3 Susceptibility measurements

When a superconductor is placed in an applied magnetic field supercurrents are induced to shield off the field. This exclusion of magnetic fields is one of the most basal signs of superconductivity. The superconducting transition temperature T_c can be measured by AC susceptibility using small magnetic fields, and flux pinning and critical current densities $j_c(B)$ can be determined from the hysteresis curve of high-field DC magnetization using the Bean critical state model, see chapter 1.3. The AC and DC susceptibility measurements were performed on a commercial Lake-Shore DCS-7000 magnetometer/susceptometer. The DC field was generated by a superconducting magnet capable of delivering magnetic fields up to 5 Tesla.

2.4 Magneto-optical technique

The field shielding response of a superconductor will give a strong spatial modulation of the total field just above the superconducting sample. By magneto-optical imaging one simply takes a picture of the magnetic field, and this will give information on defect structures in the superconductive response, flux penetration/trapping, pinning, critical current densities and current paths.

The Magneto-Optical (MO) technique is based on Faraday rotation in Bi-doped Yttrium-Iron-Garnets (Bi:YIG) grown on Gadolinium-Germanium-Garnet buffers (GGG). The rotation angle θ_F is given by

$$\theta_F = VHd \tag{2.15}$$

where the Verdet constant V is a materials constant expressing the rotation strength, H is the magnetic field and d is the distance traveled by the light in the active Faraday medium.

In the Bi:YIG layer the spins order spontaneously in the plane of the garnet film. An applied field will tilt the spins out of the plane, and the Faraday rotation will be proportional to the tilt angle. Once the spins are tilted 90° an increase of the field cannot give rise to any further rotation of the polarization vector, and the indicator plate has saturated. The saturation occurs around 100 mT. Only the field component perpendicular to the garnet film will be imaged. The Verdet constant is strongly wavelength dependent with maximum rotation around 500 nm, so selected spectral lines from a mercury lamp equipped with an optical interference filter was used to illuminate the indicator films. The basic principle of

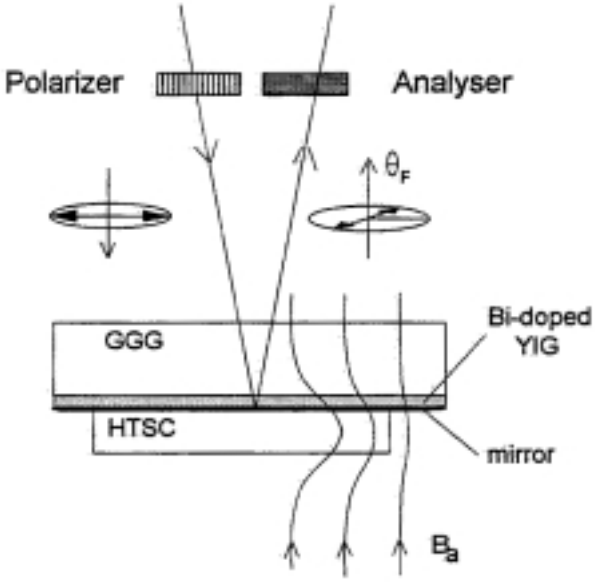

Figure 10. Configuration for detecting Faraday rotation in a Bi:YIG indicator film. The analyzer is just a second polarization filter rotated 90° with respect to the first. The mirror is a thin Al-layer. From Ref. [20].

the experimental setup is sketched in Fig. 10. The incoming light is sent through a polarization filter to make it linearly polarized. The polarization vector of the incoming light is rotated an angle θ_F when passing the Bi-doped layer of thickness d, it is reflected from the Al mirror and rotated θ_F again when passing back through the Bi-doped layer. In the configuration shown here the total Faraday rotation is then $\theta_F = 2VHd$. When observed through a second polarizer turned 90° with respect to the first, areas of zero flux will appear dark and areas of high magnetic flux will appear bright. The spatial resolution is given by the gap between the superconductor surface and the Bi:YIG film, and by the thickness of the Bi-doped layer itself. With perfectly flat samples a resolution of $\approx 2\mu m$ can be obtained. A review paper on the MO technique is given in [21].

The complete MO setup used is schematically depicted in Fig. 11. The continuous-flow He cryostat is combined with an optical microscope equipped with appropriate filters and beam splitters. The samples are glued to copper plates with low temperature varnish and mounted on the cold finger of the cryostat. The external field was applied by a Cu solenoid surrounding the cold finger. All images were recorded on a 8-bit CCD camera connected to a Personal Computer. The grey level response of the CCD images was calibrated to a range of well-known field values. The response can be well described by the function

$$g(B) = A_0 + \frac{A}{1 + \mathrm{e}^{(B-B_0)/dB}} \tag{2.16}$$

where $g(B)$ is the grey level in the CCD image, B is the field and all other variables are fitting parameters. Once the parameters have been determined the field profiles can be extracted from the MO images.

The MO technique is very fast and easy to use. It offers a high spatial and temporal resolution with response times of the Bi:YIG films of $\approx 10^{-1}$ sec [22]. It is very ideal for dynamical studies of flux penetration, flux creep and flux front instabilities. The last issue will be described in greater detail in chapter 4. The only requirement is that the samples should be reasonably flat, which is often the

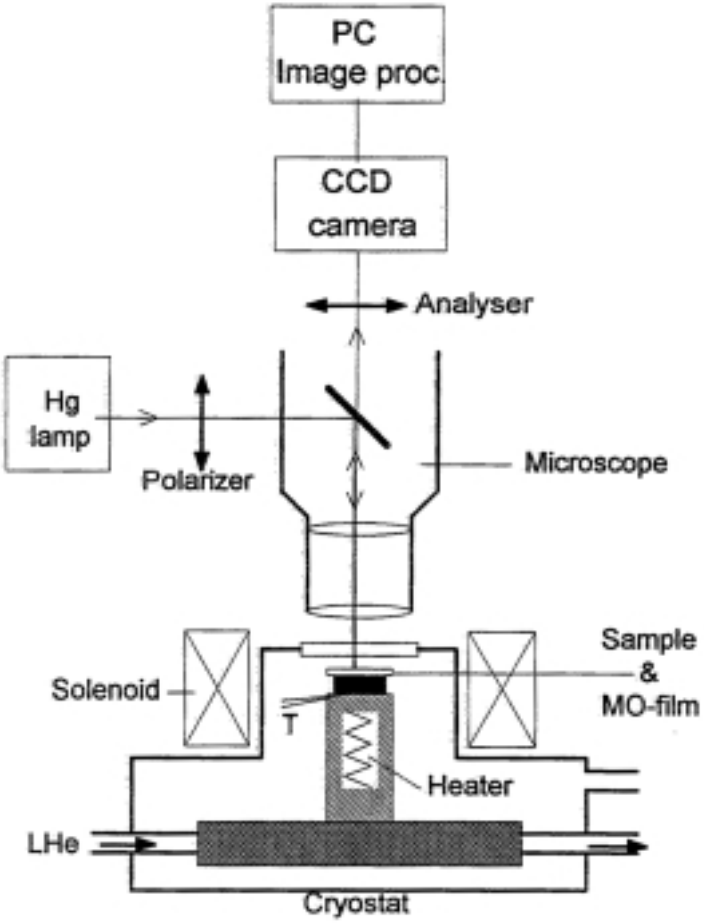

Figure 11. MO-setup. The temperature range of the continuous-flow He cryostat is 12-300K. From Ref. [20].

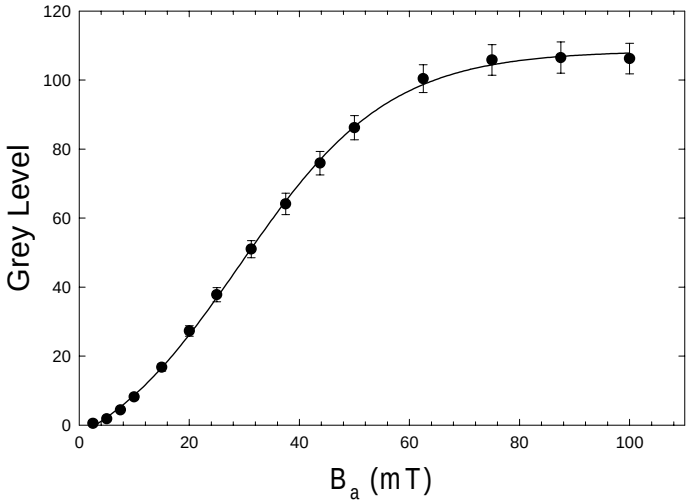

Figure 12. Grey level versus applied field. The line is a fit with equation (2.16).

case for the high-T_c cuprates. The two-dimensional character of high-T_c superconductivity means that the current distribution to a good approximation is also two-dimensional when the fields are applied along the c-axis. The major limitation of the technique is the relatively low saturation fields of the indicator films. It should be mentioned that for a 2D current distribution the resulting magnetic field is unique and the Biot-Savart law can be inverted by e.g. Fourier transforms [23, 24, 25]. In this way the current path can be determined directly from the MO images.

In my personal opinion magneto-optical investigations are the most fun you can have with a flat superconductor in a low field!

3 Oxygen ordering and charge transfer in the Re-123 system

The high-temperature superconductor $YBa_2Cu_3O_{6+x}$ (YBCO) was the first compound to display superconductivity above the boiling point of liquid nitrogen, thereby entering a new era in the history of superconductivity [26]. It was soon discovered that the replacement of Y with other rare earth (Re) elements, except Pr, Ce and Tb, do not alter the superconducting properties radically, although some changes occur, as will be described later. YBCO is no longer the only high-temperature superconductor to have a T_c above 77K, but it remains one of the most well-studied cuprates, and it is important both as a model system and for use in applications.

3.1 Variation of T_c with oxygen doping

The superconducting behaviour of YBCO depends strongly on the oxygen content x. For x <0.35 YBCO is an antiferromagnetic insulator, and the crystal structure is tetragonal. For $x \geq$0.35 the structure changes into an orthorhombic state, and the material becomes metallic and superconducting. The dependence of T_c on x is shown in Fig 13.

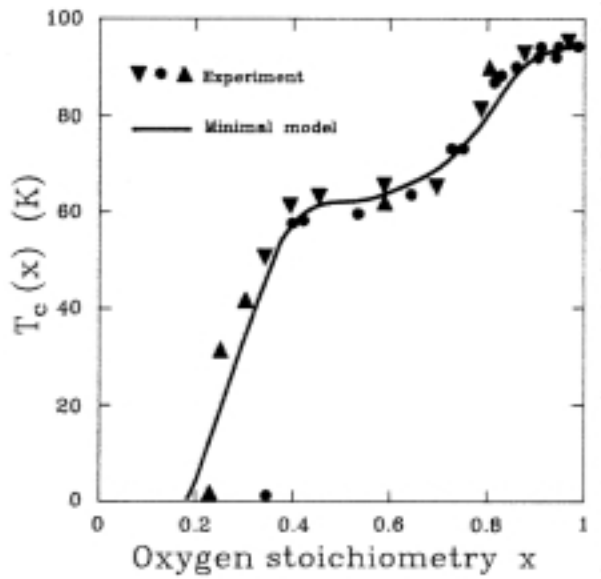

Figure 13. Variation of T_c with the oxygen content x in $YBa_2Cu_3O_{6+x}$. Symbols are from experiment, the full line is from theory [27]. Some of the data are old, the circles represent the presently accepted values.

For studies of the charge transfer mechanism responsible for the hole-doping into the CuO_2 planes (or electron-doping in the case of e.g. $La_{2-x}Ce_xCuO_4$), the $YBa_2Cu_3O_{6+x}$system is not the most simple, because is has two adjacent CuO_2 planes per unit cell. However, as the charge transfer depends on the oxygen content and oxygen ordering in the CuO_x plane it is not necessary to grow a new sample for each doping level as in the La-214 system. Instead the oxygen content can be altered in a well-controlled manner throughout the doping range for a single sample, thus one can be sure that changes in the superconducting properties are

only due to the change in oxygen stoichiometry.

3.2 Oxygen chains

It has been well established for more than a decade [28] that the oxygen atoms in the basal plane of the unit cell tend to align in chains along one of the crystal axes (by convention taken as the b-axis) when the oxygen content x exceeds $\approx$0.35. The chain formation is accompanied by the structural transition from a tetragonal state to a weakly distorted orthorhombic state. At room temperature the difference in the a and b axis length is $b - a = 0.035$ Å for $x = 0.50$ [17]. The orthorhombic distortion induces a twinning of the a and b axis with an interchange of the short and long axis in different domains of the crystal [29]. The 60K plateau in T_c around x=0.5 seen in Fig. 13 is coinciding with the formation of the so-called ortho-II structure. Here the oxygen occupancy is one oxygen atom per every second unit cell, and the oxygen chains arrange spontaneously in such a way, that every other oxygen site along the a-axis is unoccupied.

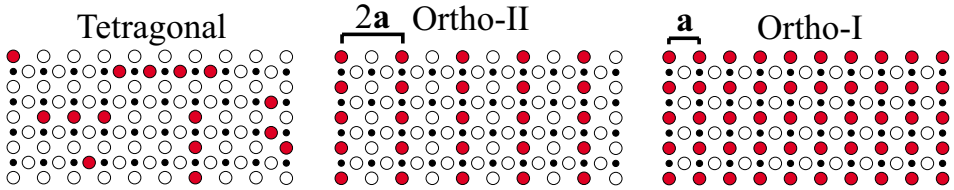

Figure 14. Oxygen configurations in the tetragonal state (x <0.35, disordered), in the orthorhombic state at half oxidation (x=0.5) and at full oxidation (x=1). Small filled circles are Cu atoms, large open and filled circles are empty and occupied oxygen sites, respectively.

A simple model of the basic charge transfer mechanism [30] from the CuO_x basal plane is shown in Fig 15. A single occupied oxygen site in the basal plane can accept two electrons from surrounding Cu ions, giving the oxygen a valence of O^{2-}. In oxygen chains only one electron is transferred to each oxygen ion, giving a valence of O^{-}. The oxygen ions are now able to accept another electron from the CuO_2 planes, thereby hole doping the planes and making them metallic rather than insulating. This is a simplified version of the charge transfer mechanism. It may not be sufficient to consider the length of the oxygen chains only. Model calculations indicate that two-dimensional domains of oxygen chains rather than just one-dimensional single chains play a role for the $T_c(x)$ behaviour [27].

A model that satisfactorily accounts for the oxygen arrangements is the ASYmmetric -Next-Nearest-Neighbor-Ising (ASYNNNI) model, originally introduced by de Fontaine *et al.* [31]. It describes the interaction forces by a number of interaction parameters, shown in Fig. 16. The model originally includes the interaction parameters V_1, V_2 and V_3 with V_1 and V_3 repulsive and V_2 attractive. By incorporating the ASYNNNI model into Monte-Carlo simulations the Ortho-I and Ortho-II phases as well as the tetragonal-orthorhombic phase transition could be reproduced in the simulations. However, the temperature of the tetragonal-orthorhombic phase transition predicted by the model is too high, and it also predicts long-range correlations of the Ortho-II phase, which are never seen experimentally. Modification of the ASYNNNI model [32] by introducing additional interaction parameters V_4 and V_5 reproduces most of the structural properties established by neutron, electron and x-ray diffraction. The Monte Carlo simulations are not a part of this thesis, but the simulations have been made concomitantly

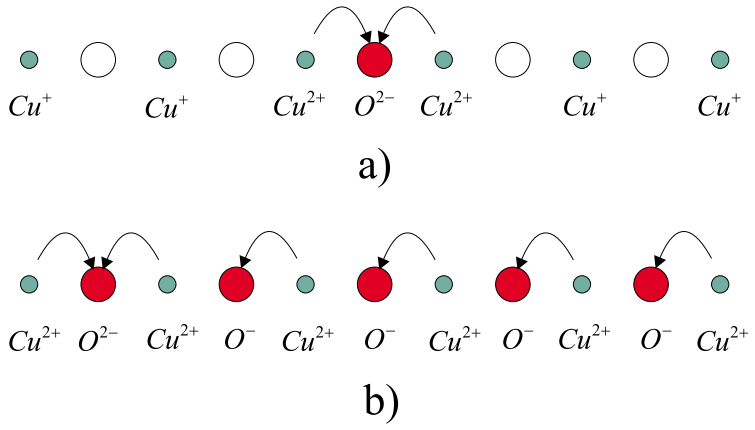

Figure 15. Charge transfer mechanism in the CuO_x basal plane. Small circles are Cu ions, large open circles are empty oxygen sites, large filled circles are occupied oxygen sites. a) single oxygen ions have a valence of O^{2-}. b) In isolated oxygen chains most oxygen ions have a valence of O^- and charge transfer is possible.

with the experimental work, and as the results of the simulations are of major importance to understand the details of the oxygen ordering properties, they will be referred to in the text whenever appropriate.

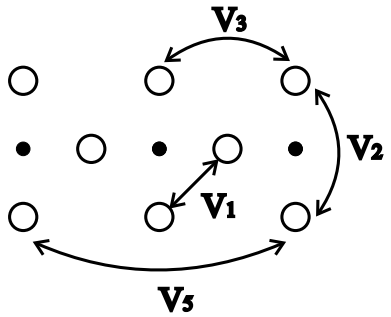

Figure 16. The ASYNNNI model of the basal plane oxygen interactions. Filled circles are Cu atoms, open circles are oxygen sites. The interaction parameters V_1 to V_5 are indicated by arrows. V_4 (not shown) is a weak coupling along the c-axis.

Since the charge transfer process is closely related to the detailed oxygen configuration in the basal plane, any theoretical predictions of the charge transfer mechanism will have to be consistent with the observed structural phase diagram of YBCO. In this context YBCO plays an important role as an extremely well-studied model system, where the forces and interactions governing the oxygen configuration on both shorter and longer length scales are known in great detail. It is also interesting as a lattice-gas system, where theory and experiment can be compared in a direct manner.

Single crystal studies

The use of single crystals is paramount to the success of studying weak superstructures with an intensity of typically 10^{-6} to 10^{-4} of the fundamental Bragg peaks. Using powder diffraction for these studies would be almost impossible for two reasons: first of all the intensity of every reflection is reduced by many orders

of magnitude, as the scattered radiation is distributed along the Debye-Scherrer cone rather than being concentrated in a narrow angle. Especially for neutron scattering the unavoidable incoherent background can quickly render any superstructure reflected intensity below the experimental detection limit. Secondly, the structural information perpendicular to the scattering vector is lost as powder diffraction only yields the scattered intensity as function of d-spacing. The transverse information is equally important in the studies.

3.3 The five orthorhombic superstructures

The structural phase diagram of oxygen order in the orthorhombic phase has been investigated by careful preparation of the oxygen content of high-quality single crystals of YBCO by the gas volumetric technique (chapter 2.2) that were subsequently characterized by high-energy synchrotron x-ray diffraction. The crystals studied were from two sources: either from University of British Columbia in Canada [33] or from Institut für Technische Fysik in Karlsruhe, Germany [34]. In a few cases of dubious results new samples were prepared in order to verify the experimental findings. Five orthorhombic oxygen superstructures have been found and their stability limits have been established. The ideal oxygen configurations for ortho-I,II,III,V,VIII are shown in Fig. 17.

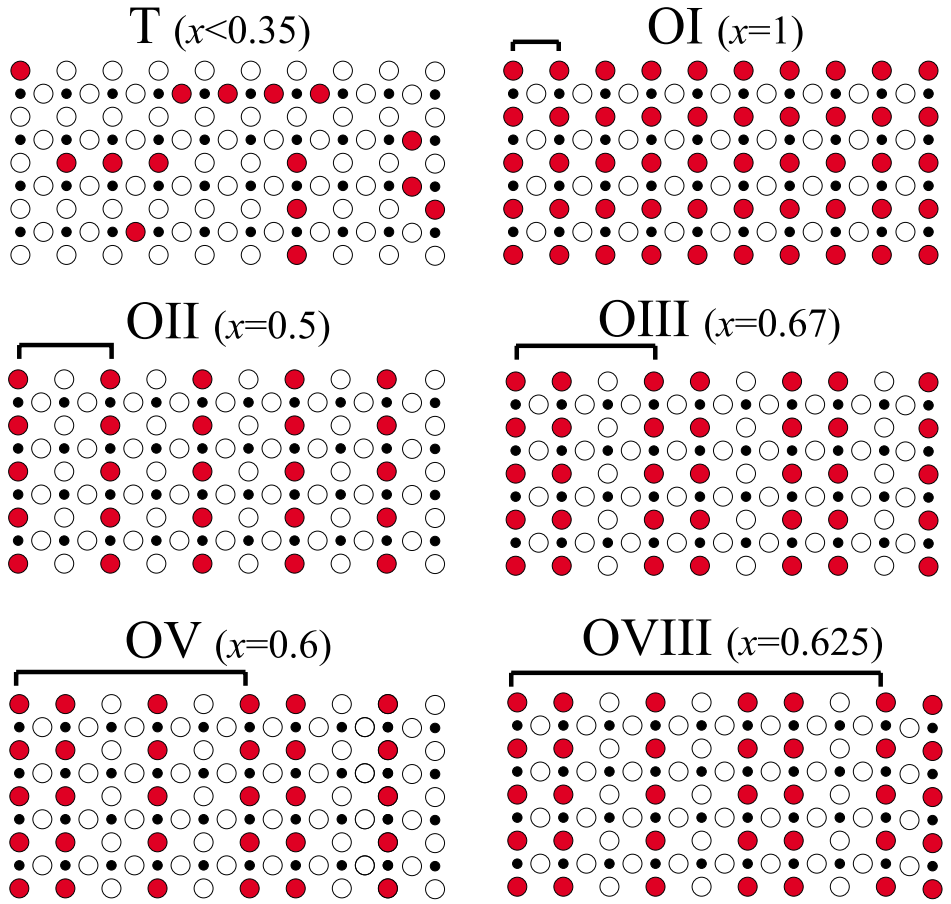

Figure 17. The disordered tetragonal phase and the five orthorhombic oxygen superstructures in $YBa_2Cu_3O_{6+x}$. The ideal oxygen concentration listed for each phase is not the same as the concentration for which the phase is actually observed, cf. Fig. 18.

Because of stacking faults where some oxygen atoms occupy sites in the empty chains the phases are observed at slightly higher oxygen concentrations than that corresponding to the ideal configurations. The experimentally established phase diagram is shown in Fig. 18. Note that the ortho-V phase only is found coexisting with the ortho-II phase. Only the ortho-II phase displays 3D ordering, the other orthorhombic superstructures are predominantly 2D.

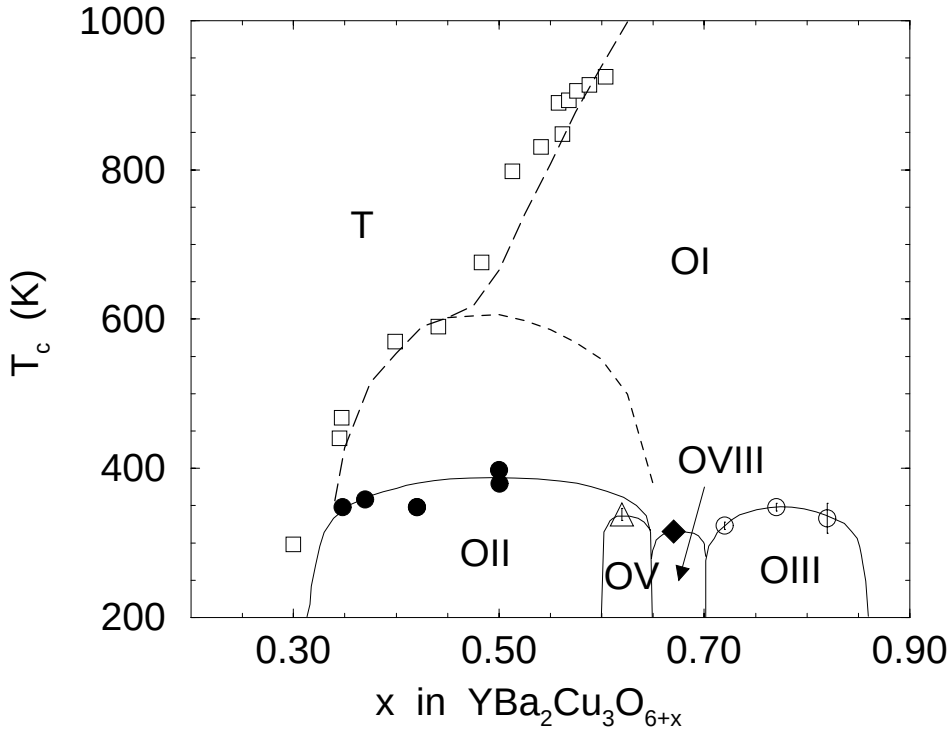

Figure 18. Structural phase diagram for $YBa_2Cu_3O_{6+x}$. Oxygen superstructures are determined by hard x-ray diffraction, the orthorhombic-tetragonal transition indicated by squares is determined by neutron diffraction. Solid lines are guides to the eye, dashed lines are predictions from the ASYNNNI model.

The results are described in detail in **Paper 1**. The appearance of the structural phases have been verified qualitatively by other techniques like neutron diffraction or transmission electron microscopy [35].

3.4 Dynamical behaviour of the Ortho-II phase

One of the first signs of the influence of oxygen ordering on the superconductive properties in YBCO came from quench experiments by Jorgensen *et al.* [36]. Here it was demonstrated that a fast quench of an underdoped YBCO crystal suppressed T_c, and by a subsequent room temperature annealing at constant oxygen content T_c started increasing with time accompanied by changes in the structural properties. As shown by Madsen *et al.* [37] the minimum temperature for the oxygen atoms to increase their order is 250K. We have performed quench experiments on a high-purity single crystal of YBCO with x=0.50, near the optimum oxygen content for formation of the ortho-II phase. The time development of the ortho-II phase after quenching into a disordered state was investigated over a couple of weeks by neutron diffraction. Here the time resolution was one hour, limited by the intensity of the neutron source. Quench studies were performed at the synchrotron with a time resolution of one second, and the superstructure peak profile

as function of time was determined the following way: By performing a number of identical quenches and measuring the intensity at different points along h, k and l for every quench the profile development could be calculated by fitting a Lorentzian squared to the points at equidistant time intervals. The resulting peak intensity, correlation length (proportional to the inverse peak width) and integrated intensity are shown in Fig. 19.

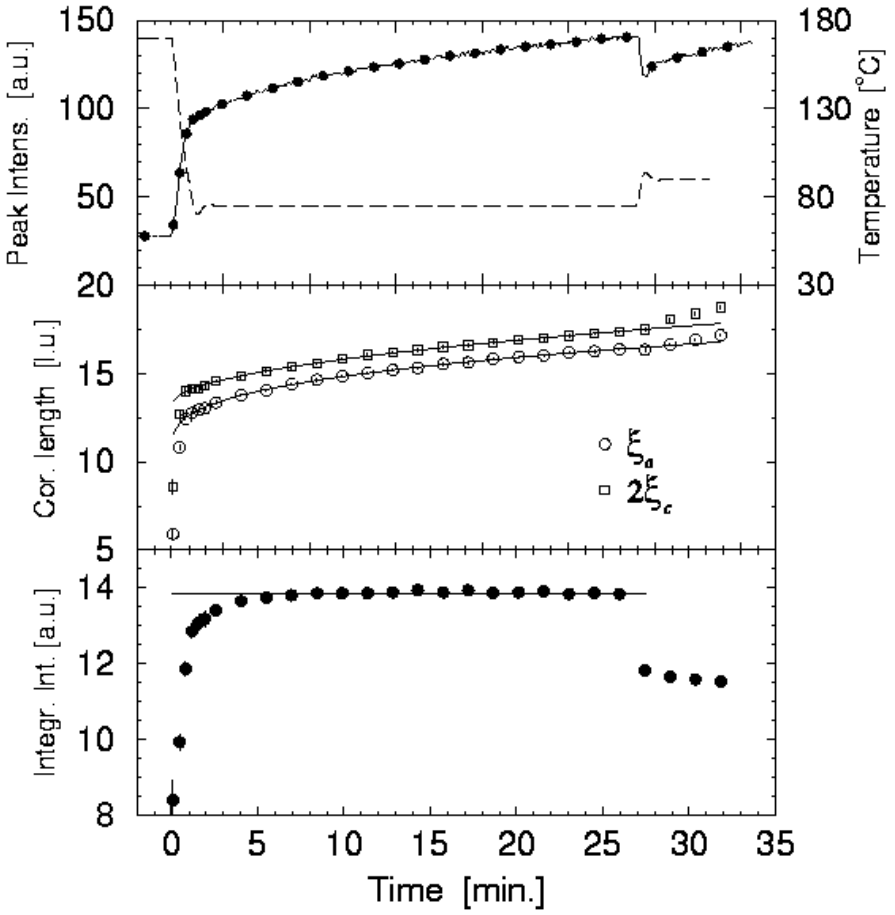

Figure 19. Ordering kinetics of the ortho-II superstructure observed by hard x-ray diffraction at (2.5 0 5)*. Upper panel shows the peak intensity (solid points, left ordinate) and temperature profile (dashed lines, right ordinate), middle panel shows the correlation lengths along the a-axis (ξ_a) and c-axis (ξ_c) and the lower panel shows the integrated intensity.*

Fig. 19 shows that dynamical scaling applies, i.e., for a fixed temperature the integrated intensity is constant but the correlation lengths increase with time while maintaining the anisotropy ratio. Thus, the volume occupied by the ortho-II phase is only a function of temperature while the correlation lengths depend on the history of the thermal treatment and the oxygen diffusion speed. More detailed information can be found in **Paper 2**. The paper also contains a relatively brief overview on the superstructure phase diagram and Monte Carlo simulations of the oxygen ordering using the ASYNNNI model.

3.5 A tetragonal $YBa_2Cu_3O_{6.62}$ single crystal - a freak of nature?

During the systematic studies of the orthorhombic phase diagram an unexpected feature appeared: a crystal prepared to an oxygen stoichiometry of x=0.62 turned out to be tetragonal when measured with the low resolution setup for superstructure studies. The crystal had prior been prepared for an oxygen concentration of x=0.50 and had displayed a clear ortho-II superstructure, so the unexpected tetragonal symmetry was not due to bad sample quality. Another YBCO crystal grown from less pure chemicals had been prepared simultaneously with the tetragonal crystal for reference purposes, the two crystals were positioned within one centimeter in the furnace during the gas volumetric annealing procedure. After the oxygen preparation was finished both crystals were annealed at 80 °C for one week to develop the oxygen superstructures. The value of 80 °C is taken from the dynamical studies of the ortho-II phase, see Paper 2.

The reference crystal was briefly characterized by recording the diffraction pattern on a 2D CCD detector, and it was clearly orthorhombic with twinning of the basal axes and an ortho-II superstructure. Thus, the tetragonality was not due to mistakes in the gas volumetric preparation, that could have lead to an oxygen concentration x <0.35 belonging to the tetragonal part of the phase diagram.

Superconducting properties

The mysterious tetragonal crystal was checked for superconductivity by AC susceptibility, and it turns out that it is superconducting with two transition temperatures: a minor volume with a T_c of 43K and a greater volume with T_c of 27K, see Fig. 20.

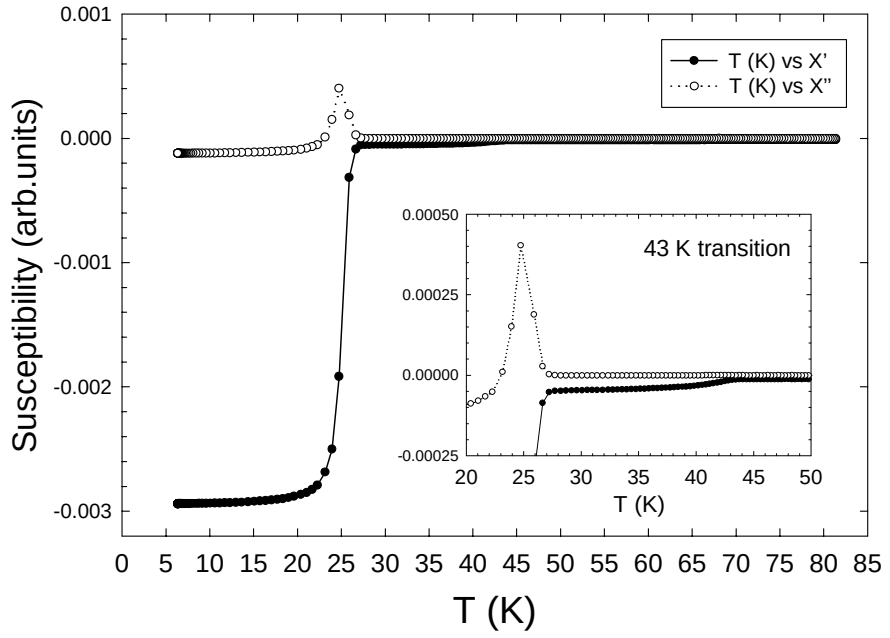

Figure 20. AC susceptibility of the tetragonal $YBa_2Cu_3O_{6.62}$ single crystal. Insert shows the susceptibility curve around 43K in greater detail. The applied field was 3 Gauss rms, frequency 125 Hz.

The next question was of course whether the crystal is bulk superconducting or if the superconductivity originates from a minor, orthorhombic part of the crystal. To settle this issue the sample was investigated by magneto-optical imaging. The sample was accidentally cleaved into two pieces along the *ab* plane when it was mounted for the MO investigations. The surfaces were slightly rugged, so the optimum spatial resolution of $\approx 2\mu$m was not obtained. Both pieces gave identical MO results.

The procedure used for the magneto-optical studies was typically as follows: The sample was cooled below T_c in zero field, and a small external field (≈ 1 mT) was subsequently applied. A defect-free crystal will totally shield off the applied field and the sample contour is seen as a dark shadow in the MO images. At increasing fields flux will begin to penetrate from the edges. If the sample contains non-superconducting defects as e.g. cracks the flux will penetrate along the defects at the lowest fields, and this is immediately seen as bright areas in the MO images. Weakly superconducting links as e.g. Josephson junctions can shield off low fields, but the flux will start to penetrate when the field is increased. When the field is decreased to zero, flux lines will be trapped because of pinning, cf. Fig. 3. This is called the *remanent state*. The remanent state can also be obtained by cooling from temperatures above T_c in an applied field and removing the field when the desired temperature $< T_c$ is reached.

The MO images show beyond doubt that the crystal is bulk superconducting as seen in Fig. 21. At fields lower than ≈3 mT the external field is completely shielded by the crystal (not shown in the figure). Between 3 and 5 mT the flux penetrates into the crystal and divides it into a major domain and an elongated edge domain (Fig 21b). Above 5 mT the crystal is divided into three domains, where the two larger sections have a T_c of 27K and the elongated edge domain has a T_c of 43K (Fig 21c-e), consistent with the AC susceptibility results. External fields greater than 75 mT could fully penetrate the sample at 16K.

Structural properties

With the knowledge of the superconductive domains the sample was characterized with hard x-rays again, this time in greater detail. A setup with optimum resolution was chosen. Perfect Si crystals were used as monochromator and analyzer. The Si (2 2 0) reflection was chosen to investigate the (0 2 0) reflection of the tetragonal crystal, as there is a close lattice match for these reflections. In this way we were close to the nondispersive setting that offers maximum resolution, see chapter 2.1. The lattice parameters of the YBCO crystal were determined to $a = b = 3.8652$ Å and $c = 11.7289$ Å. The d-spacings of the monochromator/analyzer crystals and sample crystal was $\mathrm{Si}_{220} = 1.92005$ Å and $\mathrm{YBCO}_{020} = 1.9326$ Å.

The size of the incoming beam was reduced to 0.4×0.4 mm^2 by a slit and the crystal was mounted with the *ab*-plane horizontally in the scattering plane. Because the 43K region was at the sample edge it was possible to illuminate essentially either the 27K domain or the 43K domain and determine the structure of the domains individually. Grid scans were performed for the (0 2 0) reflection, and the results are shown in Fig. 22. The peak shape was Lorentzian squared and the width of the 27K domain was $\Delta k = 4 \cdot 10^{-4}$, $\Delta h = 4 \cdot 10^{-4}$ Å^{-1}. For the 43K domain $\Delta k = 7 \cdot 10^{-4}$, $\Delta h = 8 \cdot 10^{-4}$ Å^{-1}. By orienting the sample with the *ac*-plane horizontally and scanning the sample itself through the monochromatic beam while monitoring the (2 0 0) reflection it became clear that near the center of the sample there was a local variation in the mosaicity distribution of 20″ in the

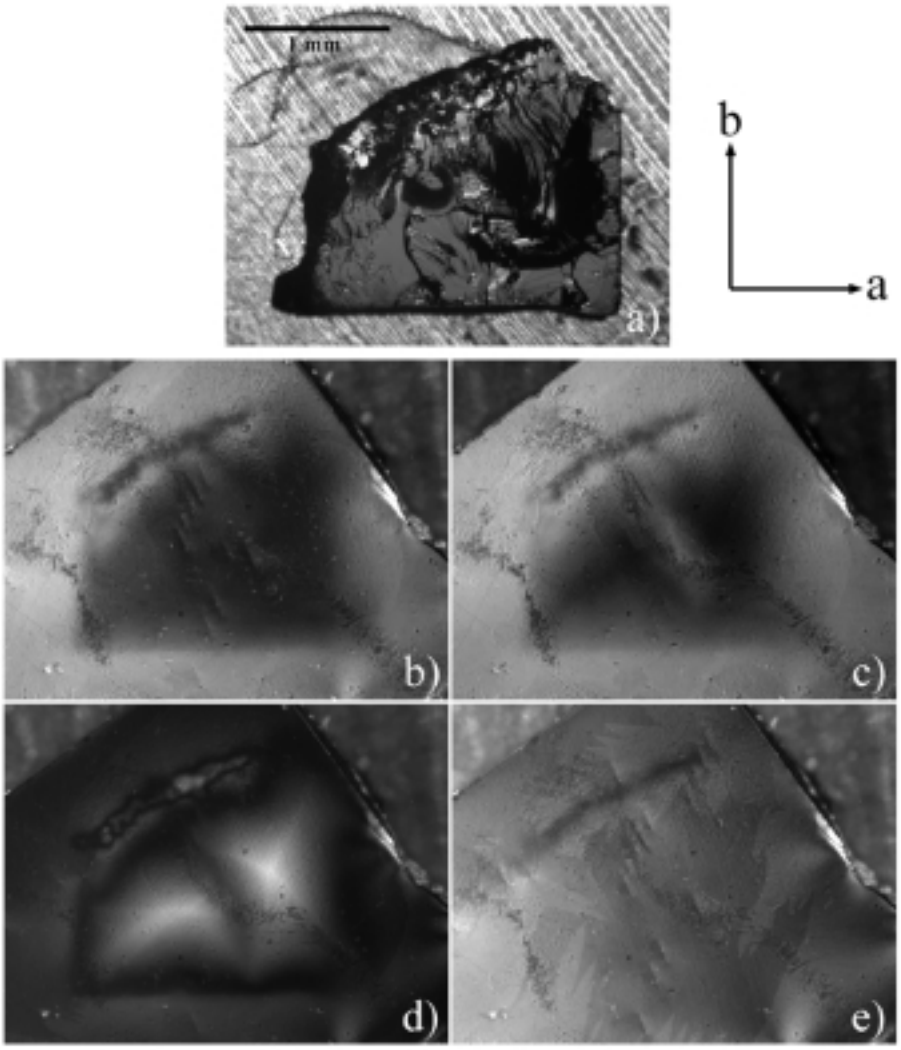

Figure 21. MO images of the tetragonal $YBa_2Cu_3O_{6.62}$ single crystal. a) The crystal mounted on the Cu plate. The scale bar is 1 mm long and the crystallographic axes are indicated to the right. b) Field shielding at 17K, B_a=5 mT. c) B_a increased to 10 mT. d) Remanent state after full penetration with B_a=100 mT. e) Only the edge domain is shielding at 26K, B_a=2.5 mT.

ac-plane. Thus, the superconducting weak link boundary separating the two 27K domains seen in Fig 21c,d is due to local variations in the mosaic distribution.

The transverse resolution is not affected by departures from the nondispersive setting (see chapter 2.1). The longitudinal resolution is reduced in the dispersive setting, but with the close lattice match we have, the approximate expression (equation (2.13)) is not valid, and we shall merely assume that the longitudinal resolution is a little larger than for the perfect nondispersive geometry. The longitudinal resolution for 100 keV photons using Si(2 2 0) perfect crystals in the nondispersive setting has been both calculated and determined experimentally by Bouchard *et al.* [13], and they find a longitudinal 2θ width with FWHM $0.56''$. With the transverse resolution being of the order 10^{-5} Å^{-1}, we should be able to detect an orthorhombic splitting of $\Delta h \approx 10^{-5}$ Å^{-1} ($\approx 0.05''$) and $\Delta k \approx 1.4 \cdot 10^{-4}$ Å^{-1} ($\approx 0.55''$).

We see that for the 27K domain Δk is resolution limited, while Δh is governed

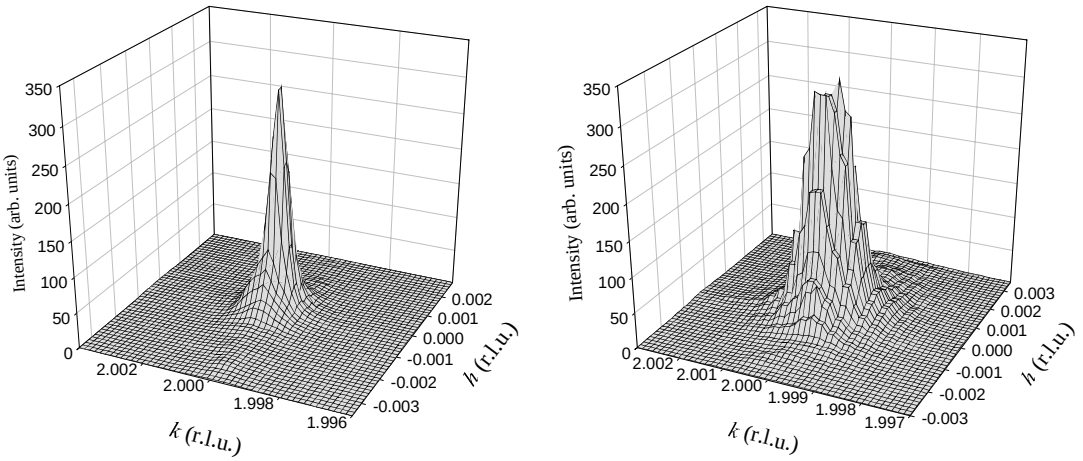

Figure 22. Grid scan of the (0 2 0) reflection for a) the 27K domain and b) the 43K edge domain.

by the mosaicity. It should be mentioned that the typical mosaicity for YBCO samples is of the order $200''$, meaning that this sample has an extremely low mosaicity. Compared to the 27K domain the 43K domain is broadened considerably, both transverse and longitudinally, and it may be a sign of a very weak orthorhombic splitting.

A search was carried out for superstructure reflections, using a setting with imperfect $Si/TaSi_2(1\ 1\ 1)$ crystals [16] as monochromator and analyzer. No diffraction reminiscent of the orthorhombic superstructures or herringbone type reflections was observed. Weak diffuse scattering with extremely low intensity was found close to some Bragg peaks, but we did not succeed in establishing a symmetry of the reflections, and the results were inconclusive.

An independent check of the oxygen concentration in the tetragonal crystal would be highly desirable if we want to conclude beyond doubt that the stoichiometry truly is $YBa_2Cu_3O_{6.62}$. The Risø Condensed Matter Physics and Chemistry Department has recently (March 1999) purchased a Time-Of-Flight Secondary-Ion-Mass-Spectrometer for element analysis, and work is in progress to determine the oxygen content of the crystal by use of this instrument.

A singularity in the structural phase diagram?

In 1988 it was still debated if the orthorhombic state was necessary for having superconductivity in YBCO.

Superconductivity with $T_c \approx 50$K has been observed in a tetragonal single crystal of composition $YBa_2Cu_{2.862}O_{6.62}$ in 1988 by Topnikov *et al.* [38]. In this careful crystallographic study the tetragonality of the sample was also well established. The sample preparation fundamentally differed from the gas volumetric method used by us; the sample was annealed in oxygen at high pressures - one to two bar - and cooled very fast to room temperature from 800-850 °C. The pressures involved in the gas volumetric procedure were typically less than 50 torr and the cooling was always very slow. As shown in Table 1 the lattice parameters for the anomalous $x = 0.62$ samples studied by us and Topnikov *et al.* agree very well but deviates significantly from the generally accepted values for normal YBCO samples in the orthorhombic state with $x = 0.62$ as well as in the underdoped tetragonal state ($x = 0.30$).

	This study	Topnikov *et al.*	$x = 0.62$ (normal)	$x = 0.30$ (normal)
a (Å)	3.8652	3.869	3.825	3.855
b (Å)	3.8652	3.869	3.880	3.855
c (Å)	11.7289	11.723	11.70	11.79

Table 1. Lattice parameters for the anomalous tetragonal $x = 0.62$ YBCO samples compared to "normal" sample values. First and second columns are this study and Topnikov et al. *[38], respectively. Third and fourth columns are generally accepted values from Andersen* et al. *[17] for orthorhombic YBCO with $x = 0.62$ and for tetragonal YBCO with $x = 0.30$.*

Do we have a singularity in the structural phase diagram at x =0.62? There are no indications in the Monte Carlo simulations of this, and studies of another crystal at this particular doping show a mixture of the ortho-II and ortho-V superstructures for x=0.62, see Paper 1. If we have a singularity in the phase diagram it must be sharp indeed.

There are also open questions with respect to the existence of superconductivity in the tetragonal sample. There is no long-range superstructure formation as in the orthorhombic state, and the superconductivity is strongly suppressed compared to orthorhombic samples with same oxygen concentration. We cannot expect the same type of orthorhombic superstructures as in "normal" samples, as these are strongly connected to the orthorhombic crystal symmetry, but we would expect some sort of chain formation in order to have a charge transfer from the basal plane to the CuO_2 planes (cf. Fig. 15). A higher mosaic spread or orthorhombic distortion has clearly a beneficial influence on the superconductive behavior, cf. Fig. 22.

3.6 Oxygen ordering in $NdBa_2Cu_3O_{6+x}$

Of the $ReBa_2Cu_3O_{6+x}$ type high-T_c cuprates, $NdBa_2Cu_3O_{6+x}$ (Nd-123) is perhaps the one most widely used for applications. Compared to YBCO it has superior processing properties as the crystal growth rate in the ab versus c direction is much less anisotropic. This facilitates the growth of large single crystals and especially melt-textured samples. Thin films of Nd-123 also have more smooth surface structure than YBCO thin films. Furthermore, at optimum oxygen doping the maximum T_c is a few degrees higher than in YBCO (close to 96K), and the flux pinning is often substantially stronger than in YBCO, especially at high fields and/or at temperatures close to T_c. The improved flux pinning is ascribed to the fact that Nd ions can occupy the Ba-sites in the crystal structure. This will locally suppress T_c on length scales that match the size of a single flux line, increasing the flux pinning when the Nd substituted areas enter the normal-conducting state [39].

Another distinction between Nd-123 and YBCO is the $T_c(x)$ dependence. Whereas YBCO becomes orthorhombic and superconducting at $x \approx 0.35$, Nd-123 remains tetragonal and insulating up to $x \approx 0.65$.

The superconducting and antiferromagnetic phase diagram as function of oxygen doping has been studied for various Re-123 compounds by Lütgemeier *et al.* [40]. Fig. 23 shows the $T_c(x)$ behavior for YBCO, Nd-123 and $LaBa_2Cu_3O_{6+x}$ (La-123). From Nuclear Quadrupole Resonance (NQR) measurements Lütgemeier *et al.* suggest that the different behaviour of T_N and T_c originates from other types of oxygen ordering taking place in the compounds with rare earth atoms having a larger ionic radius than Y. From the number of nearest neighbors estimated by the NQR frequencies Lütgemeier *et al.* suggest that at $x = 0.50$ the oxygen atoms in La-123 form the "herringbone" structure $2\sqrt{2}a \times \sqrt{2}b \times c$ while in Nd-123 they

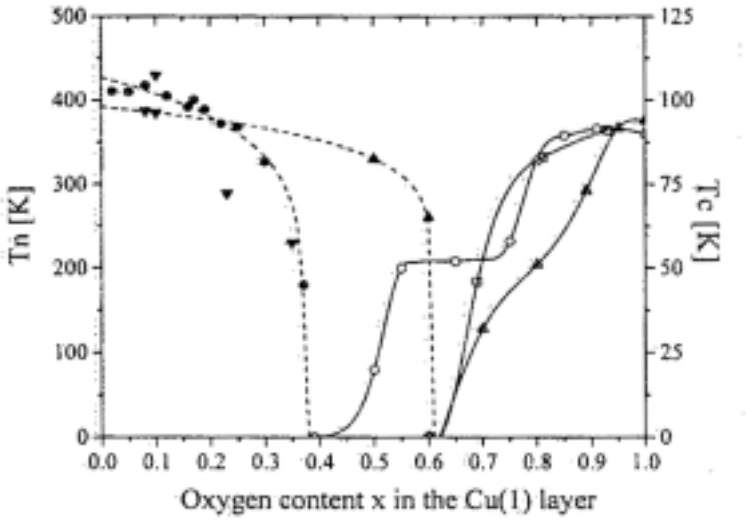

Figure 23. AF and SC transition temperatures T_N and T_c. Left scale: circles and down triangles YBCO, up triangles Nd-123. Right scale: circles Y, Gd and Tm 123 compounds, triangles Nd-123 and squares La-123. From Lütgemeier *et al.* [40].

For Nd-123, T_c has a "shoulder" at $x \approx 0.75$ which might be the signature of superstructure formation as for the 60K plateau in YBCO

are randomly distributed. Inspired by this work we have prepared single crystals of Nd-123 and La-123 to oxygen concentrations of Nd-123: x=0.41, 0.50, 0.76 and La-123: x=0.52, 0.76 and characterized the samples by hard x-ray diffraction. In Nd-123 ($x = 0.50$) we find a distinct oxygen superstructure with a symmetry fundamentally different from the orthorhombic phases in YBCO. The superstructure found cannot give rise to charge transfer to the CuO_2 layers.

Experimental

The samples were grown by a flux method in yttria stabilized zirconia crucibles [41]. The samples received an oxygen treatment optimized for YBCO. As mentioned in chapter 2.2 the oxygen equilibrium pressure as a function of temperature is known in detail for YBCO, but for Nd,La-123 the equilibrium curves are not known in the same detail. Since the equilibrium pressures in the Nd,La-123 compounds are a little higher for the same x as for YBCO [42] we expect the true oxygen content to be slightly smaller that the value aimed for. Three Nd-123 crystals with an oxygen concentration of $x = 0.5$ were investigated, one sample had some Nd substitution on the Ba-site, the other two samples were from the same piece of a crystal that had no Nd/Ba substitution. One of the Nd-123 (x=0.5) samples with no Nd/Ba substitution was investigated by AC susceptibility down to 5.5K, and there were no indications of superconductivity, as expected. The Nd-123 sample with x=0.76 had a T_c of 40K. This value is in good agreement with the $T_c(x)$ dependence shown in Fig. 23, indicating that the oxygen content is close to the concentration aimed for. No susceptibility measurements were performed on the La-123 samples.

For the hard x-ray diffraction experiments perfect Si(2 2 0) crystals were used for investigations of sample mosaicity, see preceding chapter of the *Tetragonal* $YBa_2Cu_3O_{6.62}$ sample, and imperfect $Si/TaSi_2$(1 1 1) crystals [16] with a mosaicity of 50″ were used as monochromator/analyzer for the superstructure investigations. The samples were wrapped in Al foil and mounted on a small furnace that was centered in an Eulerian cradle, as described in Paper 1.

Results

The three Nd-123 samples prepared to x=0.5 showed distinct superstructure reflections. The results from the three samples were qualitatively the same, but the superstructure was much stronger in the samples with no Nd/Ba substitution, and the results will be shown for these samples only. None of the other La-123 and Nd-123 samples showed any sign of superstructure reflections despite careful scans along a number of symmetry axes in reciprocal space. Only the Nd-123 $x = 0.5$ samples will be described in the following.

Crystal parameters were $a = 3.9117$ Å, $b = 3.9114$ Å, $c = 11.8423$ Å for the samples with no Nd/Ba substitution and $a = 3.9107$ Å, $b = 3.9102$ Å, $c = 11.8442$ Å for the sample with Nd on the Ba site. The mosaicity of the most studied Nd-123 sample (no Nd/Ba substitution) was determined from the grid scans of the (0 2 0) reflection using exactly the same setting as for the tetragonal $YBa_2Cu_3O_{6.62}$ sample, see chapter 3.5. The result is shown in Fig. 24. The sample mosaicity was found to be $\Delta h = 3 \cdot 10^{-4}$ Å^{-1} and $\Delta k = 3 \cdot 10^{-4}$ Å^{-1} was limited by the longitudinal resolution.

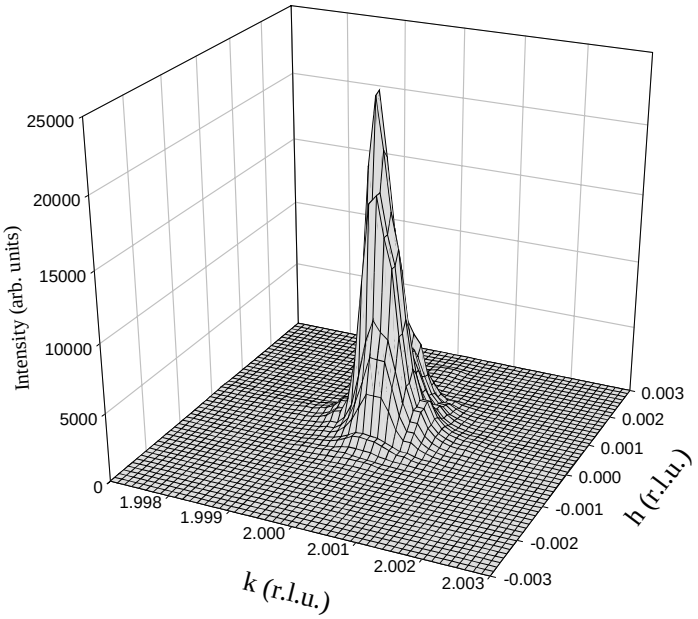

Figure 24. Grid scan of the (0 2 0) reflections of the $NdBa_2Cu_3O_{6.5}$ sample.

The intensity of the superstructure reflections was $\approx 10^{-4}$ of the fundamental Bragg peaks. The superstructures were found in all zones of reciprocal space investigated, but most scans were performed in the zone spanned by the (1 3 l) and (2 4 l) vectors because there was only little overlap with the Al powder lines in this part of reciprocal space.

Superstructure reflections were found along the diagonals of the zones, peaking at both integer and half-integer l (this will be discussed in detail later). Despite careful search no reflections were found along any of the principal axes, unlike for the orthorhombic superstructures in YBCO. Fig. 25 shows a scan along the $(1\ 4\ \frac{1}{2}) \rightarrow (2\ 3\ \frac{1}{2})$ diagonal, the insert shows the symmetry of the superstructure reflections in the $(h\ k\ \frac{1}{2})$-plane.

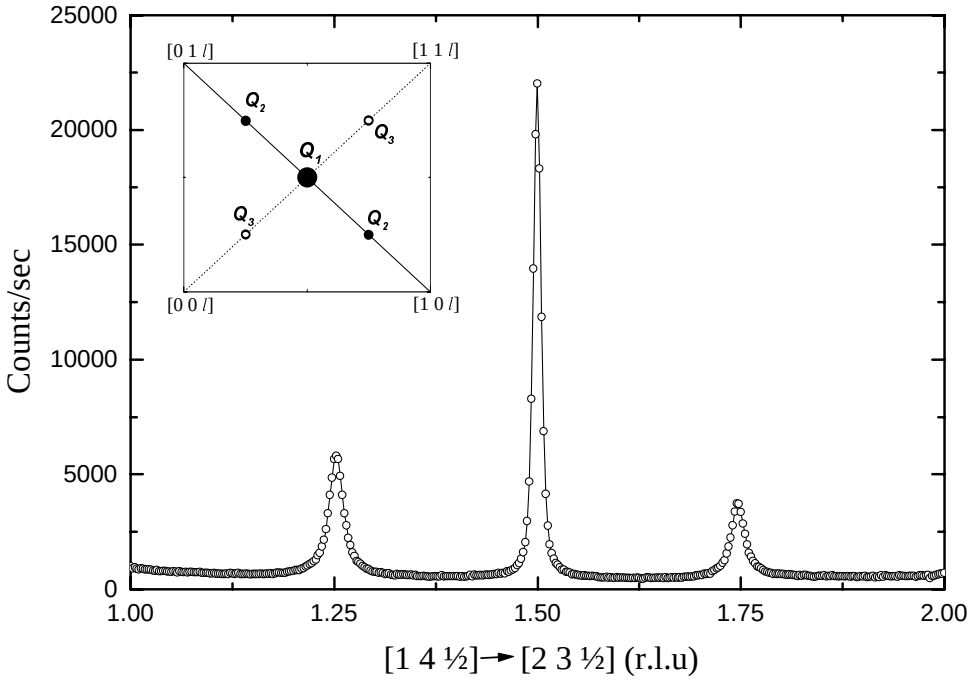

Figure 25. Diagonal scan from (1 4 $\frac{1}{2}$) to (2 3 $\frac{1}{2}$) of the oxygen superstructure. Insert shows the symmetry of the superstructure in the (h k) plane. The scan is probing the scattered radiation along the full drawn line through the $\boldsymbol{Q_1}$ *and* $\boldsymbol{Q_2}$ *vectors.*

The l-dependence for the superstructures at (1.5 3.5 l), (1.75 3.25 l) and (1.75 3.75 l) is shown in Fig. 26. From the l dependence of the remaining two superstructure reflections in the same zone, shown in Fig. 27, we find that there are three ordering vectors $\boldsymbol{Q_1}$, $\boldsymbol{Q_2}$ and $\boldsymbol{Q_3}$ (see insert in Fig. 25) describing the superstructure reflections with respect to the fundamental Bragg reflections given by

$$\begin{aligned} \boldsymbol{Q_1} &= (\frac{1}{2}\ \frac{1}{2}\ \frac{1}{2}) \\ \boldsymbol{Q_2} &= \pm(\frac{1}{4}\ \frac{3}{4}\ \frac{l}{2}) \\ \boldsymbol{Q_3} &= \pm(\frac{1}{4}\ \frac{1}{4}\ \frac{l}{2}) \end{aligned} \tag{3.1}$$

The $\boldsymbol{Q_1}$ ordering vector peaks are fundamentally different from the $\boldsymbol{Q_2}$ and $\boldsymbol{Q_3}$ peaks, with relatively narrow peaks at every half-integer l. The $\boldsymbol{Q_2}$ and $\boldsymbol{Q_3}$ peaks are much broader in l, indicating a shorter correlation length, and they tend to peak at both integer and half-integer l. The lineshape of the $\boldsymbol{Q_1}$ peaks is perfectly Lorentzian, $\boldsymbol{Q_2}$ is best fitted with Gaussians peaking at half-integer and integer l and $\boldsymbol{Q_3}$ can be fitted equally well with Gaussians, Lorentzians or Lorentzians squared peaking at half-integer and integer l. The intensity variation with l follows approximately the same trend for the three vectors. There are some differences however, most notably at $l = \pm 4.5$ where $\boldsymbol{Q_1}$ and $\boldsymbol{Q_2}$ have maximum intensity while $\boldsymbol{Q_3}$ is extinguished.

The temperature dependence of the superstructure reflections was determined from h and l scans of the $\boldsymbol{Q_1} = (\frac{3}{2}\ \frac{7}{2}\ \frac{1}{2})$, $\boldsymbol{Q_2} = (\frac{5}{4}\ \frac{15}{4}\ 0)$ and $\boldsymbol{Q_3} = (\frac{5}{4}\ \frac{13}{4}\ 0)$

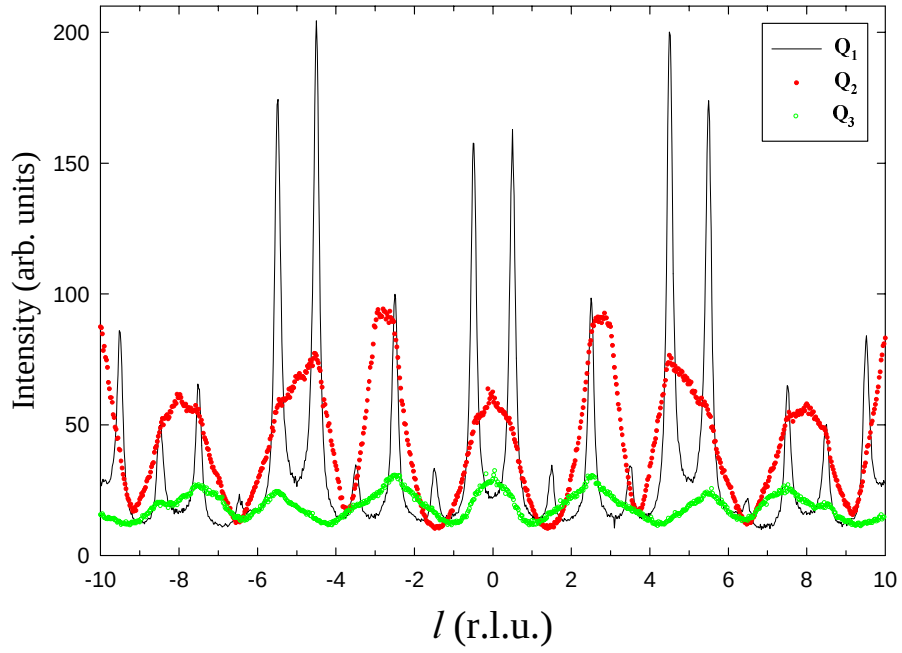

Figure 26. l-scan in reciprocal space of the oxygen superstructures with ordering vectors $\boldsymbol{Q_1}$*=(1.5 3.5 l),* $\boldsymbol{Q_2}$*= (1.75 3.25 l) and* $\boldsymbol{Q_3}$*=(1.75 3.75 l).*

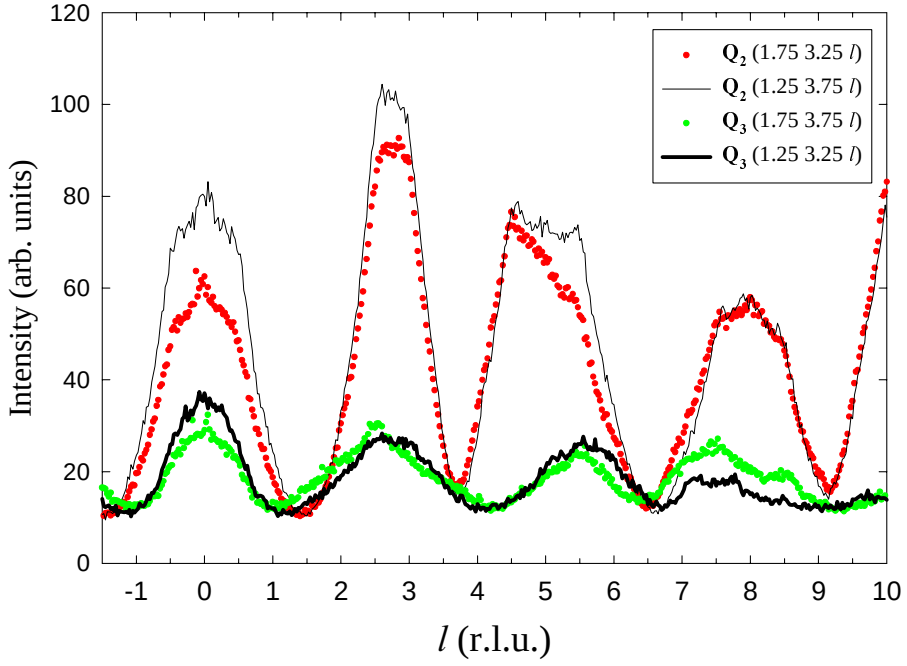

Figure 27. Four l-scans at the ordering vector positions $\boldsymbol{Q_2}$ *and* $\boldsymbol{Q_3}$*. Circles represent the same scans as shown in Fig. 26, lines represent scans at other positions in the same zone in reciprocal space. The intensities are normalized to the synchrotron current, as always.*

reflections. For the h correlations the peaks were fitted with a Lorentzian. For l $\boldsymbol{Q_1}$ was fitted with a Lorentzian, $\boldsymbol{Q_2}$ was fitted by five Gaussians centered at $l = 0, \pm\frac{1}{2}, \pm 1$ and $\boldsymbol{Q_3}$ was fitted with three Gaussians at $l = 0, \pm\frac{1}{2}$ with the Gaussians all having the same width. The result is shown in Fig. 28. For all three vectors the intensity drops close to zero at 50 °C ±1°. For the h-scans there is still residual scattering from the $\boldsymbol{Q_2}$ vector above 50 °C, that persists until ≈ 130 °C. Notably, the correlations and intensities along the c-axis persist well above 50 °C. This indicates that the correlation along c is quite (surprisingly) strong, consistent with the pronounced ordering along l. There is a significant broadening of the peaks at the 50 °C transition temperature, except for the l correlations of the $\boldsymbol{Q_2}$ vector that remains constant. The intensity did not return immediately when cooling to room temperature again, but after three days the superstructure reflections had regained 10% of the intensity, and they were broadened by a factor of 3. After six months annealing at room temperature the superstructure intensity had fully recovered.

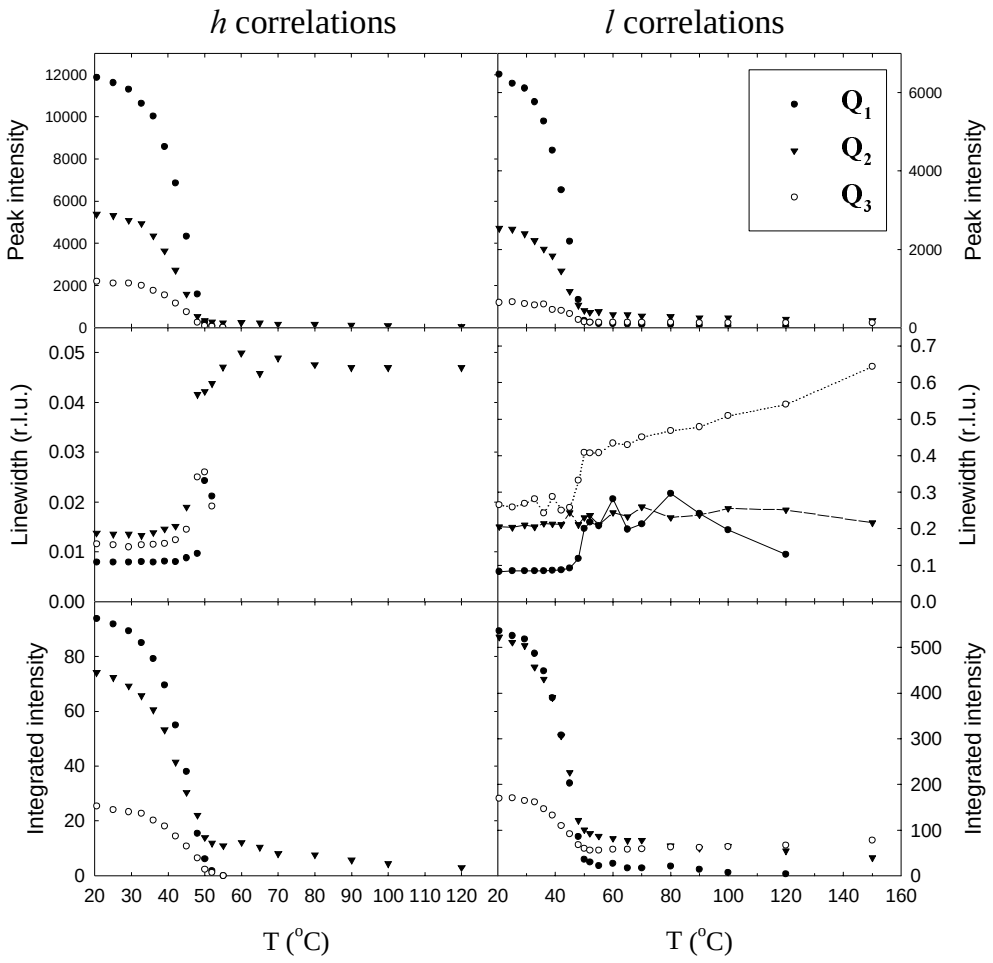

Figure 28. Temperature dependence for the three superstructure vectors. The linewidth is FWHM.

Two coexisting oxygen superstructures

The temperature dependence and long-time recovery at room temperature annealing demonstrates that the diffuse reflections truly originate from oxygen ordering, and not some impurity phase as e.g. observed in some YBCO samples [43, 44].

The symmetry of the superstructure reflections is different from the "herringbone" superstructure suggested by Lütgemeier *et al.* [40], as the two possible orientations of this structure can never give the $\boldsymbol{Q_2}$ and $\boldsymbol{Q_3}$ reflections in the same zone. A Fourier transform of the diffraction pattern to solve the structure was not attempted - besides the ever-existing problem with lack of knowledge of the phase, the number of reflections measured was too limited, and given the commensurate symmetry of the diffraction pattern a significant number of superstructure reflections would most likely be coinciding with the intense fundamental Bragg peaks, making any attempt to determine their intensity futile. Another approach was chosen: the superstructure unit cell could relatively easy be established, and assuming an oxygen concentration of exactly $x = 0.50$ the diffraction patterns for all possible oxygen configurations within the given unit cell were calculated numerically. Here is was also assumed that the oxygen occupied only the O(1) and O(5) sites in the basal plane. As it turns out two unique configurations in combination give the experimentally determined superstructure reflections. The implementation procedure for the numerical calculations is given in the appendix to this chapter, while the results are described in the following:

The smallest unit cell that reflects the symmetry of the superstructure reflections is a $2\sqrt{2}a \times 2\sqrt{2}b \times 2c$ unit cell with $a = b$ in the tetragonal state. This unit cell is rotated 45° with respect to the fundamental crystallographic unit cell in the ab-plane, and has a doubling of the c-axis. The transformation from the h, k, l indices in the reciprocal basal unit cell to the h_s, k_s, l_s indices of the reciprocal superstructure unit cell is given by

$$\begin{aligned} h &= \frac{1}{4}(h_s + k_s) \\ k &= \frac{1}{4}(-h_s + k_s) \\ l &= \frac{1}{2}l_s \end{aligned} \tag{3.2}$$

Assuming that we have an oxygen occupancy of exactly x=0.50, each plane within the superstructure unit cell will be occupied by four oxygen atoms, e.i., eight oxygen atoms in all. There are 16 available sites in each plane, in total 32 in the unit cell, and we can define that the first site is always occupied (relaxing this requirement will only give more symmetrically equivalent solutions in the end). This gives 455 combinations in the first plane and 1820 combinations in the second, since we cannot impose the same restriction of site occupancy here. The limited number of combinations, 828100 in total, makes it feasible to systematically try out all the combinations using the calculation power of a personal computer. Discarding all combinations that give reflections on the axes we find that there exist no single oxygen configuration that can give different l dependencies for ordering vectors $\boldsymbol{Q_1}$ and $\boldsymbol{Q_2}$,$\boldsymbol{Q_3}$, meaning that we have more than one single oxygen configuration in the sample. We also find that no valid configuration can give the $\pm(\frac{1}{4}\ \frac{1}{4}\ \frac{1}{2})$ reflections alone; for any configuration giving the $\boldsymbol{Q_3}$ ordering vector with peaks at half-integer l the $\pm(\frac{1}{4}\ \frac{3}{4}\ \frac{1}{2})$ reflections will also appear. Thus, the $\boldsymbol{Q_2}$ and $\boldsymbol{Q_3}$ ordering vectors originate from the same configuration. The intensity modulation along l clearly has a wave vector longer than that of the basal reciprocal lattice (it is approximately two reciprocal unit cells, cf. Figs. 26,27). A long wave vector in reciprocal space corresponds to a short-range modulation in direct space, and we must turn to small displacements within the basal unit cell to find sufficiently short ranged modulations. To a first approximation we shall disregard these modulations. This gives us the following requirements that must be fulfilled:

1. No reflections are allowed along the principal axes.
2. The $\boldsymbol{Q_1}$ domain gives reflections *only* at $(\frac{1}{2}\ \frac{1}{2}\ l+\frac{1}{2})$ with l integer.
3. The $\boldsymbol{Q_2}$+$\boldsymbol{Q_3}$ domain gives reflections at both half-integer and integer l, but *not* at $(\frac{1}{2}\ \frac{1}{2}\ l+\frac{1}{2})$.

Only two oxygen configurations exist that in combination give the right diffraction pattern. The configuration giving the $\boldsymbol{Q_1}$ vector is shown in Fig. 29a. It is simply the configuration with maximum distance between the oxygen atoms in the plane, shifted one unit cell along (1 0 0) between neighboring planes to avoid overlap along the c-axis. The other configuration is less obvious. Requirement 3 above gives an interlocked structure with two different configurations alternating from layer to layer. The simplest combination with minimal overlap along the c-axis giving the $\boldsymbol{Q_2}$ and $\boldsymbol{Q_3}$ vectors is shown in Fig. 29b.

In the following we shall refer to the oxygen structure shown in Fig. 29a as the $\boldsymbol{Q_1}$ *structure* and structure shown in Fig. 29b as the *interlocked structure* consisting of two oxygen configurations referred to as the "small squares" (green open circles) and "ragged stripes" (red filled circles) configurations, for obvious reasons. In the hk plane the "small squares" and "ragged stripes" configurations give reflections at

Color code: black, red and green atoms give the black, red and green diffraction patterns, respectively, in Figs. 26,27.

$$\boldsymbol{Q_{square}} = \pm(\frac{1}{4}\ \frac{1}{4}) \text{ and } \pm(\frac{1}{4}\ \frac{3}{4}) \tag{3.3}$$

$$\boldsymbol{Q_{stripe}} = \pm(\frac{1}{4}\ \frac{3}{4}) \tag{3.4}$$

with the l-dependence emerging from the stacking. Thus the "small squares" configuration will give reflections at both the $\boldsymbol{Q_2}$ and $\boldsymbol{Q_3}$ positions, while the "ragged stripes" configuration gives reflections at the $\boldsymbol{Q_3}$ positions only. With only one oxygen site overlap along the c-axis per unit cell, as shown in Fig. 29b, the "ragged stripes" reflections will peak at half-integer l. If the two configurations are shifted with respect to each other in the ab-plane so more than one site overlaps along c the intensity distribution will shift to integer l. The Gaussian lineshape of the $\boldsymbol{Q_2}$ reflections indicates that we do not exclusively have the structure depicted in Fig. 29b but rather a more or less random stacking of the two "squares" and "stripes" configurations dominated by the stacking shown in Fig. 29b.

Fig. 30 shows the structure factor squared calculated at the $\boldsymbol{Q_1}$, $\boldsymbol{Q_2}$ and $\boldsymbol{Q_3}$ positions as function of l. Here it is assumed that the two structures shown in Fig. 29a,b occupy equal volumes in the sample, i.e., the intensity is not scaled, it is given by the model. Comparing Figs. 30 and 26 the ratio of the intensities is very similar for the model and the experimental data. The ratio of the $\boldsymbol{Q_2}$ and $\boldsymbol{Q_3}$ intensities are fixed according to the model, but there are no *a priori* restraints on the relative intensity of $\boldsymbol{Q_1}$. Thus it seems that the two oxygen structures are equally well represented in the sample.

While the $\boldsymbol{Q_1}$ and "small squares" configurations both are invariant under a 90° rotation the "ragged stripes" would give reflections at the $\boldsymbol{Q_3}$ positions were they running along (1 $\bar{1}$ 0) and not (1 1 0) as shown in Fig. 29b. We see from Fig. 26,27 that the $\boldsymbol{Q_2}$ reflections are strongly dominating over the $\boldsymbol{Q_3}$ reflections, and we must conclude that the "ragged stripes" run almost exclusively in the (1 1 0) direction. The tetragonal symmetry does not favor the (1 1 0) direction over the (1 $\bar{1}$ 0), and we would expect that domains with "ragged stripes" running along (1 1 0) and (1 $\bar{1}$ 0) would be equally populated. Probably the preferred (1 1 0) orientation is an arbitrary sample dependent feature.

As an analogy: in twinned YBCO crystals one of the twin domains will often be strongly dominating

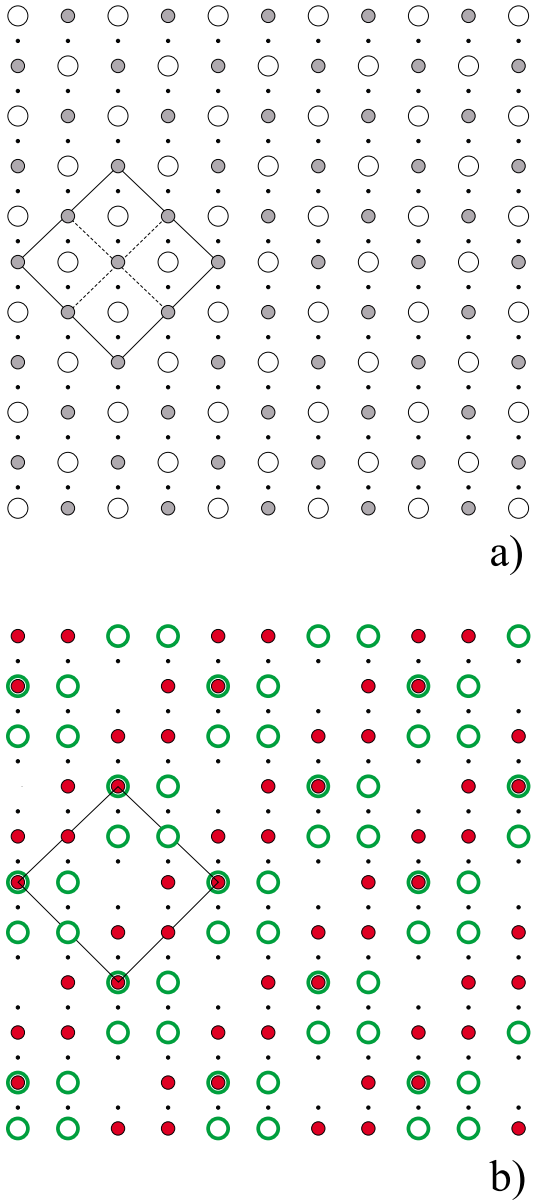

Figure 29. Oxygen configuration of the $\boldsymbol{Q_1}$ *domain a) and the stacked* $\boldsymbol{Q_2}$ *and* $\boldsymbol{Q_3}$ *domains b). Small filled circles are Cu atoms, large circles are occupied oxygen sites. Open and filled circles are shifted along the c-axis by one unit cell with respect to each other. Lines indicate the superstructure unit cell in the ab-plane. For a) the unit cell can be subdivided further as indicated by dotted lines.*

Let me emphasize that for the $2\sqrt{2}a \times 2\sqrt{2}b \times 2c$ superstructure unit cell and an oxygen concentration of x=0.50, the only configurations that will give the $\boldsymbol{Q_2}$ and $\boldsymbol{Q_3}$ reflections without giving $\boldsymbol{Q_1}$ reflections and/or reflections on the principal axes are the "small squares" and "ragged stripes" configurations. The asymmetric intensity distribution between the $\boldsymbol{Q_2}$ and $\boldsymbol{Q_3}$ reflections indicates that the "ragged stripes" configuration indeed is present in the crystal, as the "small squares" structure gives equally strong reflections on the $\boldsymbol{Q_2}$ and $\boldsymbol{Q_3}$ positions. From the temperature dependence (Fig. 28) the three ordering vector reflections also behave differently above 50 °C; an additional sign that they originate from different configurations. Be aware that the $\boldsymbol{Q_2}$ reflections are a superposition of the scattering from both "small squares" and "ragged stripes". Especially the

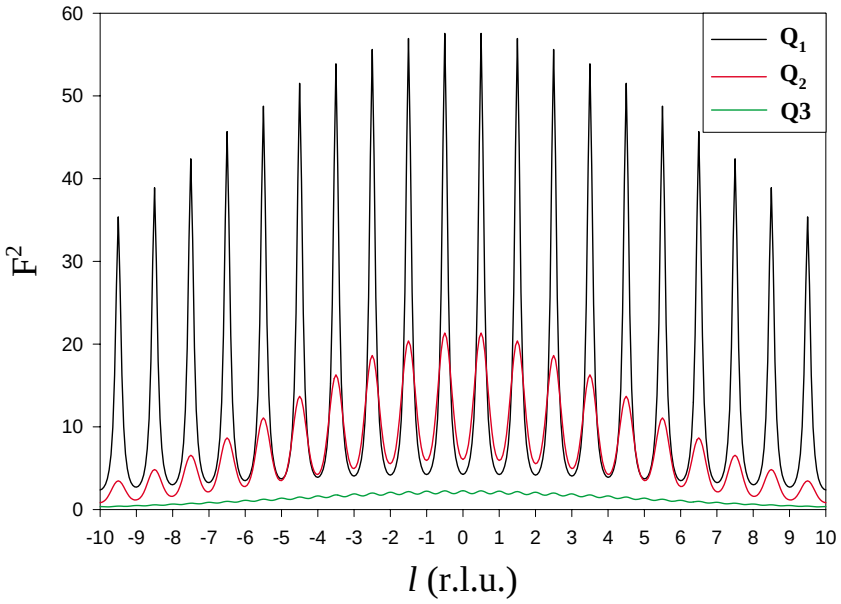

Figure 30. l-dependence of the calculated structure factor for the two oxygen superstructures in Fig. 29a,b including the atomic scattering factor f_n. The $\boldsymbol{Q_1}$ *reflection is folded with a Lorentzian,* $\boldsymbol{Q_2}$,$\boldsymbol{Q_3}$ *reflections are folded with a Gaussian. Compare with Fig. 26.*

constant linewidth below and above 50 °C along l for the $\boldsymbol{Q_2}$ reflection indicate that this configuration is very stable.

Modulation of the l-dependence

If we compare the modulation seen in Figs. 26,27 with the l-dependence of the orthorhombic oxygen superstructures in YBCO (Fig. 5,9 in Paper 1 and Fig. 2 in Ref. [45]) we find almost identical intensity modulations in the two systems. Crystallographic investigations of the ion displacements in YBCO have been made for samples with the ortho-II [46] and ortho-III [45] oxygen superstructures, and it is shown that the intensity modulation is due to small displacements of the atoms in the unit cell, induced by the oxygen ordering. Given the similarity of the intensity modulation for the YBCO and Nd-123 superstructure reflections, it might be possible to deduce the ion displacements in the Nd-123 samples using the information from [45, 46]. This would constitute an independent check whether the oxygen configurations found from symmetry considerations alone are correct, as there are some clear differences in the l-modulation for the $\boldsymbol{Q_1}$, $\boldsymbol{Q_2}$ and $\boldsymbol{Q_3}$ reflections. But the mixture of several configurations makes this a difficult task that most likely requires a more complete dataset than the one available.

Charge transfer

The oxygen superstructures in the $NdBa_2Cu_3O_{6+x}$ $x = 0.5$ samples cannot give rise to charge transfer, as there is no chain formation or clustering of oxygen atoms in domains of appreciable size (refer Fig. 15). The oxygen-oxygen interactions are mainly repulsive, but as Fig. 29b shows there must be some anisotropy, or we would only have the configuration shown in Fig. 29a. The anisotropy is most likely very weak, since the two types of oxygen ordering shown in Fig. 29a,b occupy equally large volumes in the sample, according to the model.

3.7 Conclusions

The study of oxygen ordering in the Re-123 cuprates is a fascinating topic, both the ordering in its own respect and the implications on the superconductive behavior. In the YBCO system the static and dynamical aspects of the phase diagram for the orthorhombic superstructures is by now established in such detail, both experimentally and theoretically, that I dare to say that there is not much left to do on this subject. Apart from explaining a few superconducting tetragonal samples, of course. Microscopic theories of the charge transfer mechanism in the high-T_c superconductors can be tested against a real system for which the average structural information in the superconducting state is available: $YBa_2Cu_3O_{6+x}$.

The study of oxygen ordering in $NdBa_2Cu_3O_{6+x}$ gives further support to the importance of the oxygen configuration. The arrangement at $x = 0.5$, fundamentally different from the chain structure in YBCO, will not allow superconductivity despite a rather high doping level. The co-existence of two oxygen superstructures is a beautiful and unexpected feature, especially the interlocked "small squares" and "ragged stripes" structures would be hard to believe was it not the only possible solution. The delicate nature of the configurations can be appreciated, when you consider that they will begin to melt if you keep the sample too long at the palm of your 37 °C warm hand.

3.8 APPENDIX: implementation of the numerical calculations

There are 16 different sites in each plane of the superstructure unit cell as shown in Fig. 31. For this unit cell the complex exponentials of the structure factor (equation (2.7)) can only assume four different values: ± 1, $\pm i$. This makes a very simple and fast numerical implementation possible. The Miller indices used refer to the superstructure h_s, k_s, l_s given by equation (3.2). We now have the following requirements that must be fulfilled in order to reproduce the symmetry of the experimentally determined diffraction pattern:

- Superstructure reflections are allowed to coincide with the fundamental Bragg reflections $\Rightarrow$ For $|h_s - k_s| = 4$, l_s must be even
- No reflections allowed on the principal axes $\Rightarrow$ $h_s = k_s$ forbidden for h_s, k_s uneven
- For vectors $\boldsymbol{Q_1}$ all h_s, k_s must be even. For $(h_s - k_s)/2$ uneven l_s must be uneven
- For vectors $\boldsymbol{Q_2}$,$\boldsymbol{Q_3}$ h_s or k_s must be uneven and all l_s allowed

The implementation was done on a personal computer using QBASIC (MS-DOS). The first site with fractional coordinates (x_s, y_s, z_s)=(0,0,0) is per definition always occupied. The program structure consisted of seven FOR...NEXT loops summing over the 32 sites in the superstructure unit cell, calculating the structure factor for all possible combinations. The atomic scattering factor f_n was set to 1. All configurations not complying with one or more of the requirements listed above were discarded. Calculation times were typically less than one minute.

The only configurations fulfilling the requirements was the $\boldsymbol{Q_1}$ domain shown in Fig. 29a and alternating layers of the "small squares" and "ragged stripes" structures shown in Fig. 29b. Solutions with the "ragged stripes" running along

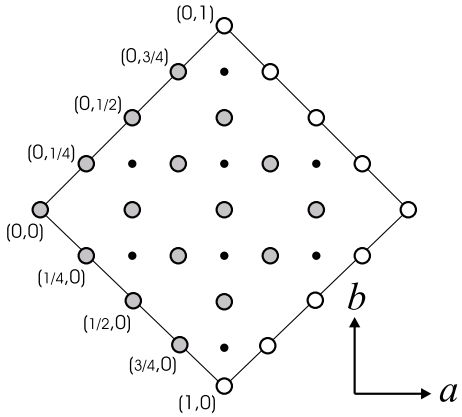

Figure 31. One plane in the oxygen superstructure $2\sqrt{2}a \times 2\sqrt{2}b \times 2c$ *unit cell with the 16 different oxygen sites shown by grey shading. Small black circles are Cu atoms. The fractional coordinates* (x_s, y_s) *are indicated.*

either (1 1 0) or (1 $\bar{1}$ 0) exists. No physically unlikely solutions were found, e.g. as simultaneous occupation of highly repulsive nearest-neighbor oxygen sites. If the calculations are performed for one plane only (455 combinations) and we only consider the h_s, k_s requirements we also get either the "small squares" or "ragged stripes" as the only solutions.

If x deviates slightly from 0.50 as we expect is the case, stacking faults will most likely be introduced. This will reduce the correlations and give a broadening of the superstructure peaks.

Finally it should be mentioned that the most intense superstructure reflections are those coinciding with the fundamental Bragg peaks, rendering a detection of these reflections virtually impossible.

4 Flux turbulence in the Re-123 system

With the high-resolution magneto-optical (MO) technique exciting new phenomena and information on flux penetration into the high-T_c materials have appeared. Especially time-varying effects can be visualized by MO imaging, as the data acquisition essentially is limited by the recorder speed and the intrinsic response time of the indicator films, which is of the order 0.1 sec [22]. The interaction of fluxlines of opposite polarity display turbulent features, which were discovered with the appearance of MO [47, 48]. In some optimally doped single crystals of YBCO the boundary zone dividing flux and antiflux behaves in a chaotic fashion, that has not yet been explained theoretically. The magneto-optical experiments described in this thesis were all performed at University of Oslo. Turbulent behavior in $NdBa_2Cu_3O_{6+x}$ and underdoped $YBa_2Cu_3O_{6+x}$ was seen, and the results are given in **Paper 3**. Here a number of parameters could be discarded as having significant influence on the turbulent behavior. Some of the results in the paper are mentioned rather briefly due to limitation in page number. These results will be shown in greater detail in the following.

4.1 Magneto-optical results

Flux front instabilities were observed in four samples: two $NdBa_2Cu_3O_{6+x}$ crystals at near-optimal doping and two underdoped $YBa_2Cu_3O_{6+x}$ crystals with $x = 0.50$ and $x = 0.82$, respectively. A non-turbulent Nd-123 crystal was also investigated in detail in order to establish the parameters governing the flux turbulence. The samples are referred to as sample I-V and they are described in more detail in Paper 3. Of the two YBCO crystals the dynamics of the oxygen ordering in sample IV ($x = 0.50$) has been studied in great detail, and the results are described in Paper 2. Structural studies of sample IV and V ($x = 0.82$) are included in Paper 1.

The chaotic behavior in sample I is shown in Fig. 32. Some extra images are included, compared to the ones also shown in Fig. 1 in Paper 3. The magnetic preparation was as follows: After zero-field cooling, the sample was totally penetrated applying a field of +100 mT. Flux of this polarity is colored green in the images. Then the field was removed, and an opposite field of -75 mT was applied. This results in a distribution of antiflux, colored as red, surrounding a small residual (positive) flux domain in the center. The first frame of Fig. 32. shows the remanent state generated by removing the -75 mT field. Note that this trapped flux has a positive return field visible as a green aura outside the crystal. A field of +25 mT was applied to the remanent state at $t = 0$ and the time development of the flux fronts is shown for the first 300 seconds. The most spectacular changes occur within the first 120 seconds, after that the flux fronts only move slightly.

There is a strong tendency for the turbulent fields to make "droplets" of flux that move in a spiral-like fashion and then disappear after a shorter or longer time [49]. Often these droplets separate from the flux front as seen in Fig. 32 at t=120 sec. The chaotic nature of the drop-formation is clearly seen in Fig. 33 showing flux-front instabilities for sample IV. Only a selected part of the crystal near the edge is shown. The field history is explained in the caption. Here the annihilation zone forms an uneven meandering shape as soon as the reverse field is applied. This shape is apparently stable for the first minute, when a flux droplet suddenly is created. The droplet persists for more than a minute, slowly wandering across

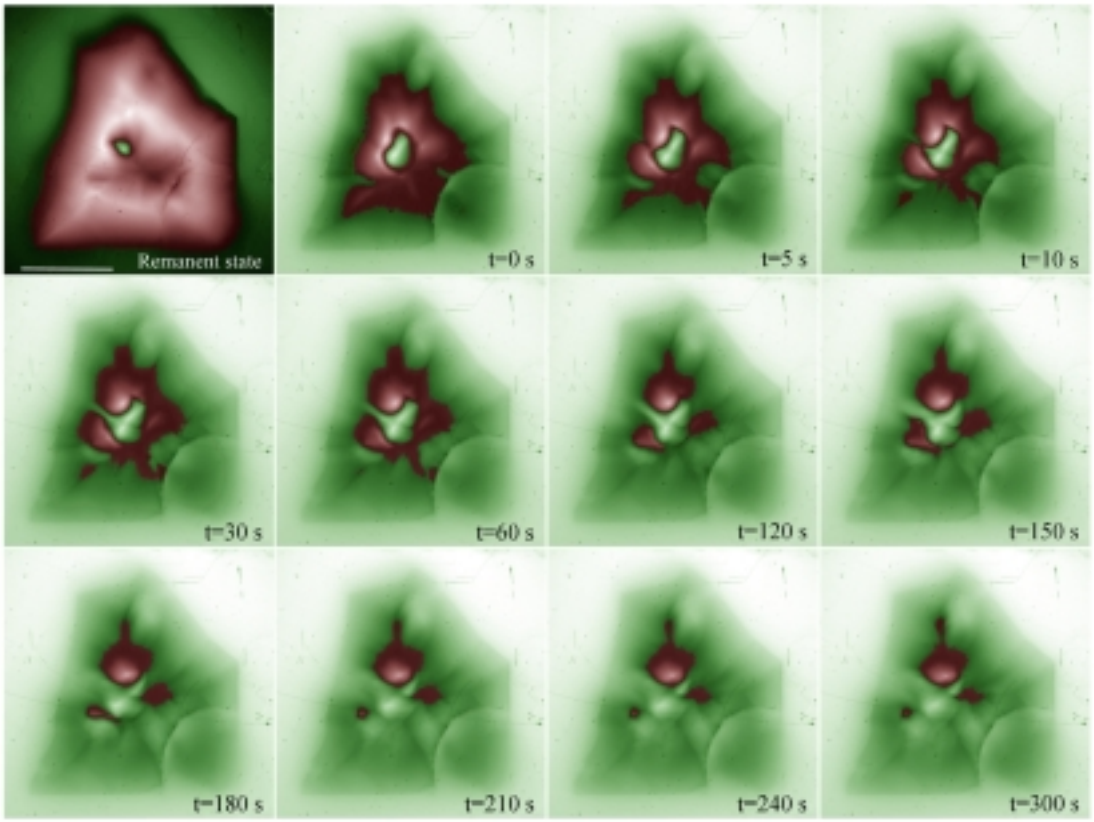

Figure 32. Flux front instabilities at T=78 K in a $NdBa_2Cu_3O_{6+x}$ single crystal (sample I). The instabilities were produced following the procedure described in the text. Bright areas correspond to areas of high flux, dark areas correspond to areas of low flux. Magnetic flux of opposite polarity is colored green (positive) and red (negative). The rounded feature in the lower right corner of the crystal is caused by a minor damage to the edge. The length of the white scale bar is 1 mm.

the crystal until it annihilates in a rotational fashion at t=150 s.

Imperfect flux shielding

A striking feature in Fig. 32 is how the central part of trapped flux (green) in the remanent state is expanding at $t = 0$ when the external field is applied. This is in contradiction to the Bean critical state model in which the induced currents always run to shield off the interior of the sample. We find that the area of the central (green) flux increases by a factor of 4 and the total flux in the area increases by a factor of 7 at t=0 compared to the remanent state, while the slope $\mathrm{d}B/\mathrm{d}x$ and thereby j_c remains constant. The images do not reveal any path where positive flux can penetrate into the central region from the outer part of the sample at t=0 sec. On the contrary the dark annihilation zone dividing the central positive flux from the surrounding negative flux persists for the first 10 seconds after which a channel of positive flux is branching the two regions of identical flux polarity. It seems that in the turbulent sample the flux shielding is imperfect, and the expansion of the central part of the flux is a signature that also the central part of the crystal experiences an effective field.

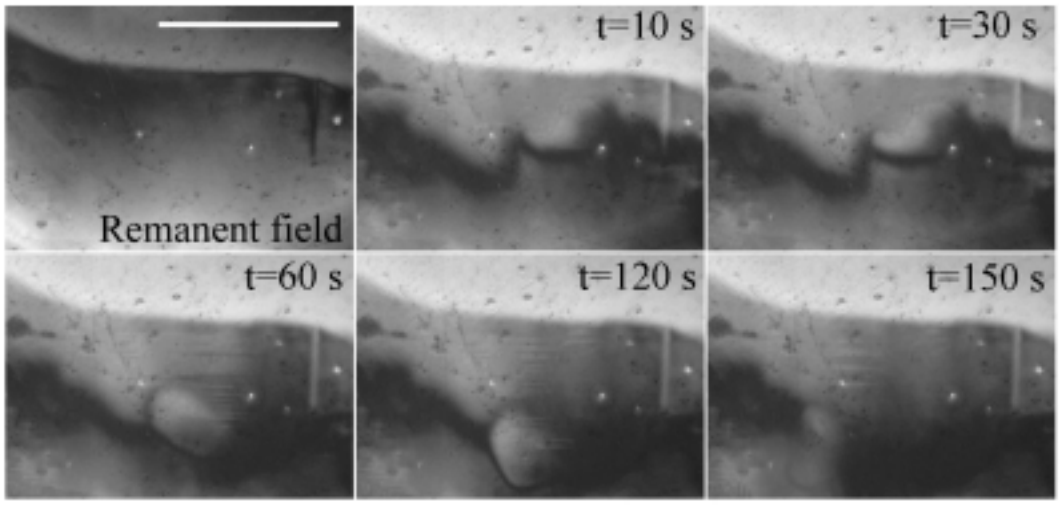

Figure 33. Flux front instabilities at T=38.5 K in a $YBa_2Cu_3O_{6+x}$ $x = 0.50$ single crystal (sample IV). The sample was zero-field cooled and fully penetrated with a field of 50 mT. A reverse field of -6 mT was applied at t=0 s. Only a selected part near the edge of the crystal is shown. The length of the white scale bar on the first image is 1 mm.

4.2 Unimportance of critical current density

It would be natural to assume that the existence of flux turbulence in a sample is related to the flux pinning. Since the flux turbulence is only observed in single crystals of high purity, one would assume that a low j_c is a prerequisite for having turbulence in a sample.

The critical current density for the three Nd-123 samples was calculated from the field profiles extracted from the MO images and from DC magnetization hysteresis loops. The sample shapes were approximately rectangular, and assuming the sample geometry to be an infinitely long slab of rectangular cross section in a parallel field with $2w$ and $2w/\alpha$ denoting the short and long side of the rectangle, respectively [50], the critical current density is calculated from the vertical width ΔM of the magnetization loop as

$$j_c(B) = \frac{\Delta M(B)}{w(1-\alpha/3)} \tag{4.1}$$

For the field profiles $\mathrm{d}B/\mathrm{d}x$ determined by MO, j_c is calculated as

$$\mu_0 j_c = 2\frac{\mathrm{d}B}{\mathrm{d}x} \tag{4.2}$$

where the factor of 2 enters equation (4.2) because the magnetization contribution is determined at the sample surface, while the DC magnetization integrates over the whole sample. To a very good approximation the flux profiles had perfectly linear slopes as shown in Fig. 3, indicating that no corrections for demagnetization were necessary.

The critical current as function of the applied field at various temperatures for samples I and III is shown in Fig. 34. The j_c curves show the fishtail effect characteristic for many Nd-123 samples [41, 51], with a temperature-dependent peak

at increasing fields. The critical current densities determined by the two methods are compared in Table 2. Note that for sample III, j_c is determined at a lower temperature than for sample I,II. The agreement of the j_c values determined by the two methods is not impressive.

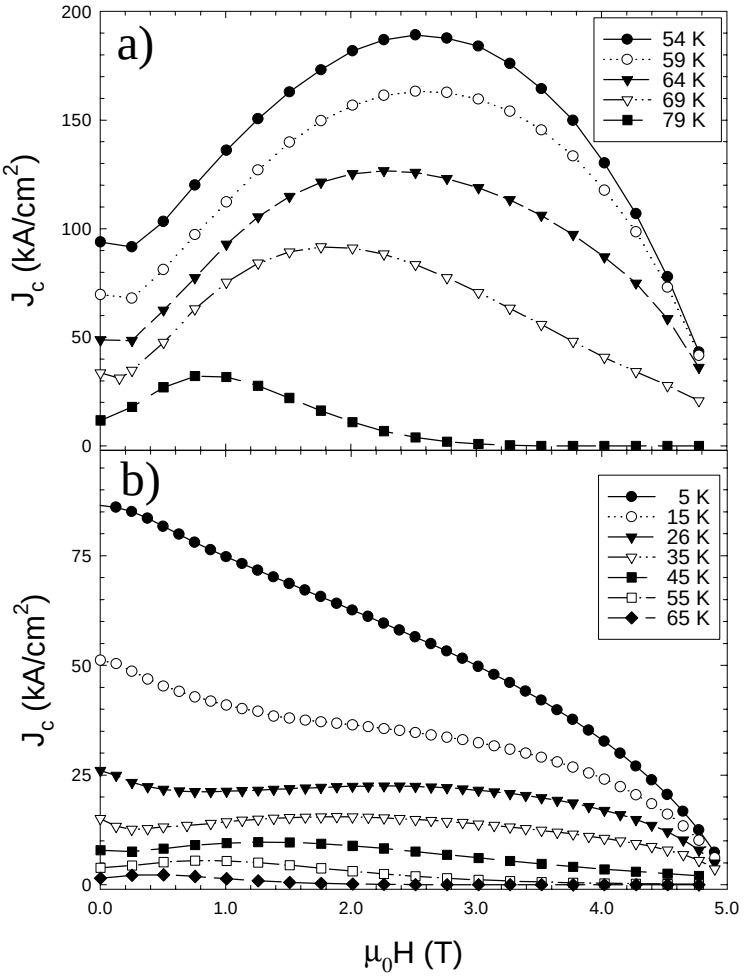

Figure 34. $j_c(B)$ determined by DC magnetization at various temperatures. a) the turbulent sample I and b) the non-turbulent sample III.

The magneto-optical images of sample I show that it contains no major defects (Fig. 32), but the sample shape is rather uneven with non-uniform thickness, and the rectangular approximation is probably too simple. The other two samples were much more rectangular shaped, especially sample III, and the discrepancy of the j_c values can not be ascribed to the sample shape. By inspection of the magneto-optical images from Fig. 2 in Paper 3 it is evident that sample II and III does not shield off the applied field as one single superconducting slab. Sample II is divided into three sections by two large weak links, and a major part of sample III is dominated by numerous defects where the flux penetrates even at the lowest applied fields. To extract more correct j_c values from the DC magnetization loops these defect structures should be taken into account. It is especially interesting to do so for the non-turbulent sample III, to better compare the influence of j_c on the turbulent instabilities with the turbulent samples. From the MO images the ratio of the total sample volume to the defect-free flux shielding volume is ≈ 3.5,

and taking this as the effective magnetization volume the critical current density determined by DC magnetization in Table 2 will be 9.8 kA cm^{-2} for sample III (as the cross section of both the total and the defect-free part of sample III is to a good approximation square shaped, j_c scales directly with the volume). This number agrees with the MO values within 10 % (the MO profile was determined from the defect-free part of the sample). Thus, to better compare Fig. 34a and b, the j_c values in b should be multiplied by 3.5. Even so, the j_c at a given temperature is much lower for sample III than for sample I. These results further support the conclusion in Paper 3 that there is little or no correlation between j_c and the occurrence of flux turbulence in a crystal.

Sample	I Nd-123	II Nd-123	III Nd-123
T_c (K)	91	87.5	81
Dimensions (mm^3)	$2.3 \times 2.7 \times 0.75$	$3.1 \times 2.5 \times 1.3$	$3.2 \times 3.2 \times 1.5$
Turbulent	Yes	Yes	No
j_c(MO) (kA cm^{-2})	6.9 at 78K	8.7 at 80K	10.5 at 60K
j_c(DC) (kA cm^{-2})	11.3 at 79K	4.0 at 79K	2.8 at 60K

Table 2. Critical currents determined from MO images and DC magnetization for $B = 0$. Further sample information can be found in the table in Paper 3.

Note on the anisotropy

As mentioned in Paper 3 it has been suggested that the electromagnetic anisotropy $\gamma = \xi_{ab}/\xi_c$ has an influence on the turbulent behavior. Recent measurements with torque magnetometry on an underdoped $YBa_2Cu_3O_{6.50}$ single crystal gives an anisotropy value of $\gamma = 53$ [52]. This value is likely to be more accurate than the value of $\gamma = 40$ for $x = 0.50$ listed in the table in Paper 3, which was estimated from various scaling arguments. This gives further support to the conclusion that also the anisotropy is of secondary importance to the turbulent phenomena.

5 Stripe phases and the $\frac{1}{8}$ problem

Shortly after the discovery of high-temperature superconductivity it was established [53] that an anomalous suppression of superconductivity occurs in the parent high-T_c compound $La_{2-x}Ba_xCuO_4$ around $x \simeq 0.125$. This is referred to as the "$\frac{1}{8}$ problem" as it has also been observed for several other compounds like Th-doped $La_{2-x}Ba_xCuO_4$ and Nd-doped $La_{2-x}Sr_xCuO_4$ [54, 55, 56] close to $\frac{1}{8}$ hole doping. The same suppression of T_c does not appear in $La_{2-x}Sr_xCuO_4$ (see Fig. 1), and this has been interpreted as related to the differences in the structural phase diagrams of the Ba and Sr doped compounds [57]. Both $La_{2-x}Sr_xCuO_4$ and $La_{2-x}Ba_xCuO_4$ undergo a structural phase transition from a High-Temperature-Tetragonal (HTT) state to a Low-Temperature-Orthorhombic (LTO) state around 180K [58]. In the $La_{2-x}Ba_xCuO_4$ compound an additional transition to a Low-Temperature-Tetragonal (LTT) phase occurs around 80K, and it seems that the $\frac{1}{8}$ problem is related to this particular LTT phase. By substitution of La with the smaller rare-earth ion Nd^{3+} in $La_{2-x-y}Nd_ySr_xCuO_4$ a similar LTT phase transition occurs around 70K, and the suppression of SC at $x \approx \frac{1}{8}$ also appears in $La_{2-x-y}Nd_ySr_xCuO_4$ with y=0.4. Band structure calculations for $La_{2-x}Ba_xCuO_4$ indicate that the density of states near the Fermi energy is relatively insensitive to the LTO-LTT transition [59], implying that it is unlikely that the suppression of T_c is related to an electronic modification by the structural transition.

The Sr content is controlling the hole doping (electronic properties) while the Nd content is controlling the structural properties.

Incommensurately splitted magnetic reflections appear in the superconducting state of $La_{2-x}Sr_xCuO_4$ in the Brilluoin zone center [60]. This resembles strongly magnetic scattering from the isostructural system $La_{2-x}Sr_xNiO_4$ in which the charges and holes segregate in stripe-like domains as shown in Fig. 35 [61, 62, 63]. This has inspired Tranquada *et al.* to search for stripe ordering in cuprates at $\frac{1}{8}$ doping [64, 65]. The concept is that if a segregation of holes and spins does take place in the cuprates as in the nickelates, one might expect that at $\frac{1}{8}$ hole filling the holes will lock commensurately to the crystal lattice, and a static correlation of immobile spin and charge stripes may occur. This could then account for the suppression of SC at $x = \frac{1}{8}$. If one considers horizontal charge stripes as depicted in Fig 35c and compare to the tilt of the CuO_6 octahedra (shown in Fig 36), one sees that in the LTT phase the charge stripes would tend to be pinned by the lattice potential, while in the LTO phase there is not a similar favorable distortion of the lattice. This is consistent with the observation that the LTT state and the $\frac{1}{8}$ problem are closely related. Two major differences between stripe ordering in cuprates (Fig. 35c) and the stripe ordering in the nickelates (Fig. 35b) should be emphasized: in the cuprates the stripes must run horizontally rather than diagonally with a 90° rotation between each plane as sketched in Fig. 37, and the charge stripes are half filled rather than fully occupied as for the insulating nickelates. A review of stripe ordering in nickelates and cuprates is given in Ref. [66].

It is not possible to perform neutron diffraction studies of stripe-phase formation in the $La_{2-x}Ba_xCuO_4$ compound, simply because it is exceedingly difficult to produce high quality single crystals of acceptable size. The situation is different with $La_{2-x-y}Nd_ySr_xCuO_4$ where rather large single crystal samples have been made.

Scattering from the stripe phases

A stripe-ordered superstructure as shown in Fig 35c following the tilt pattern in Fig. 36 will have ordering vectors $\boldsymbol{g}$ giving magnetic and charge reflections relative

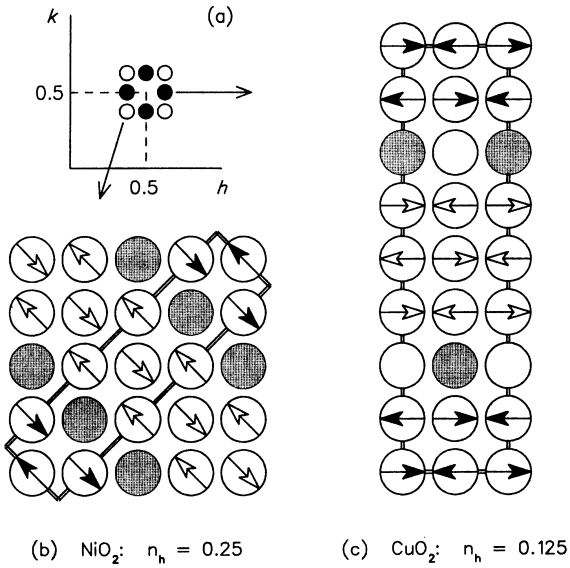

Figure 35. (a) Sketch of the (hk0) zone of the reciprocal lattice showing the positions of magnetic scattering peaks observed for hole-doped La_2CuO_4 (filled circles) and La_2NiO_4 (open circles). (b) Idealized diagram of the spin and charge stripe pattern within an NiO_2 plane with a hole density of n_h=$\frac{1}{4}$. (c) Proposed stripe pattern in a CuO_2 plane with n_h=$\frac{1}{8}$. The average charge occupancy in each charge stripe is only $\frac{1}{2}$ for the cuprate. Taken from Ref [67].

to the fundamental Bragg peaks as

$$\boldsymbol{g_{mag}} = (\frac{1}{2} \pm \epsilon, \frac{1}{2}, 0) \quad \text{and} \quad (\frac{1}{2}, \frac{1}{2} \pm \epsilon, 0) \tag{5.1}$$

$$\boldsymbol{g_{charge}} = (\pm 2\epsilon, 0, 0) \quad \text{and} \quad (0, \pm 2\epsilon, 0) \tag{5.2}$$

with $\epsilon \approx x$. Note that the splitting of the charge peaks is twice as large as for the magnetic peaks because the magnetic unit cell is twice as large as the charge-order unit cell.

Fourier analysis of the stripe configuration shows that higher order reflections from stripes will be very weak, $\approx 3\%$ of the intensity of the first order reflections, thus the absence of higher order reflections should not be in contradiction to the proposed stripe model [64] .

Results from neutron scattering

Neutron scattering studies on Nd-doped $La_{2-x-y}Nd_ySr_xCuO_4$ with y=0.4 and $x = \frac{1}{8}$ have shown incommensurate magnetic reflections towards the zone center and weak temperature dependent reflections at positions around the (2 0 0) reflection that are consistent with the stripe model [64, 65]. Unlike in the nickelates, the charge-ordering peaks have not been observed by TEM in the cuprates. The neutron scattering studies have been performed on a three-axis neutron spectrometer with a relaxed resolution in the vertical plane. There have been studies of the magnetic scattering in the l-direction, but no l-dependence of the charge-order peaks has been investigated in the neutron studies.

The implications of the stripe model may go much beyond just explaining the $\frac{1}{8}$ anomaly. Emery and Kivelson [68, 69] suggest that the phase separation of

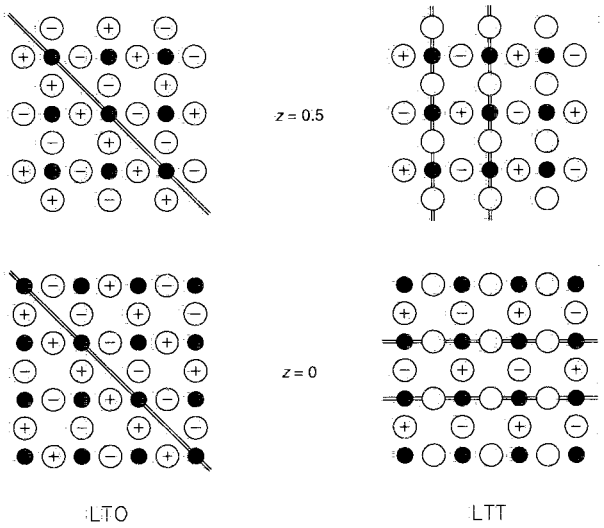

Figure 36. Displacement patterns within the two CuO_2 layers of an unit cell for the LTO and LTT structures. Open circles are oxygen atoms, closed circles are copper atoms. The oxygen atoms are displaced out of the plane (+ or -) by local rotations of square planar CuO_4 units about tilt axes shown by the double lines. In the LTT structure the tilt axes rotate by 90° from z=0 to z=0.5, where z is the height along the c axis in lattice units. Taken from Ref [64].

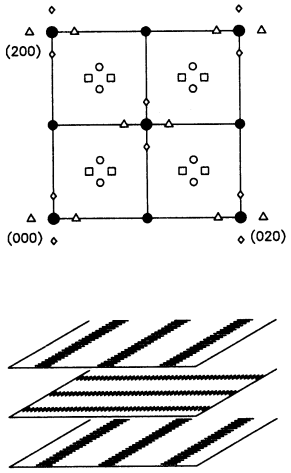

Figure 37. Magnetic reflections (open squares and circles) and charge-order reflections (triangles and diamonds) in the $(h, k, 0)$ zone in reciprocal space suggested by the stripe model. Unlike in the nickelates, the orientation of the stripes must rotate by 90° from layer to layer in order to follow the structural modulation associated with the tilting of the CuO_6 octahedra in the LTT phase, as shown in the lowest figure. Open circles and diamonds (squares and triangles) correspond to the same domain, respectively. Taken from Ref [65].

hole-rich and hole-poor regions with antiferromagnetic ordered antiphase domains constitutes the most important low energy collective excitations in the system. The interaction of mobile holes with these collective modes provides the mechanism of high-T_c superconductivity, as well as an explanation for many of the anomalous normal-state properties of the cuprates.

The experimental evidence for charge stripe formation from the neutron scattering experiments is very scarce: for the $La_{1.6-x}Nd_{0.4}Sr_xCuO_4$ x=0.12 sample only two reflections have been observed in at the positions (2±2ϵ,0,0) [64, 65], and an extremely weak peak was detected at the expected (2+2ϵ,0,0) position in a sample with x=0.15 [70]; in total two and a half peaks. It is therefore highly desirable to investigate the charge ordering by other experimental methods to verify the existence of the scattering attributed to charge ordering, and to extend the search for more peaks at positions predicted by the stripe model. There are several reasons for using high-energy x-ray scattering to search for the striped phases. The high penetration power permits the same samples to be studied with both neutrons and x-rays, as they are both bulk-probing techniques. The x-rays are much more insensitive to magnetic ordering then the neutrons, and one should observe scattering only if it originates from a change in the electron density. For the neutron studies the signals attributed to charge ordering are interpreted as coming from a distortion in the crystal lattice around the charge stripes. X-rays, on the other hand, are directly sensitive to variations in the charge density. The scattering from a single hole is very small, however, and also in the x-ray case one would expect that a diffracted signal would mainly arise from lattice distortions of the heavier ions around the holes. Also the flux from a synchrotron source is many orders of magnitude higher than that of neutron sources, and the resolution is considerably higher, although it can be discussed if a high resolution is any advantage at all in studies of broad, diffuse scattering.

5.1 Charge scattering from a nickelate

Stripe ordering was first discovered in the nickelates, where there is a significant scattering from the charge stripes when measured with neutrons. As a test case a nickelate crystal of composition $La_{2-x}Sr_xNiO_4$ with x=0.225 was investigated by hard x-ray diffraction. This particular sample had been thoroughly characterized by neutron scattering [63] and showed distinct stripe features. This constitutes an almost perfect model system for several reasons: The charge stripes are fully occupied and the coupling to the lattice is rather strong, which gives larger atomic displacements compared to the cuprates. The stripes are tilted 45° with respect to the fundamental crystal lattice, and with x=0.225 the splitting is quite large. Thus the charge peaks have the modulation vector

$$\boldsymbol{g} = (2\epsilon, 2\epsilon, 1) \tag{5.3}$$

with $\epsilon \approx x$. This implies that in reciprocal space the charge peaks are located at a convenient distance from the fundamental Bragg peaks, and can be observed without noticeably interference from the strong Bragg scattering. The basic idea was that if charge peaks cannot be observed by hard x-rays in this sample, then we could just as well forget about trying with the cuprates.

As it turns out, the charge scattering can be clearly observed with the x-rays. The results are given in **Paper 4**. Note that in the paper the tetragonal unit cell describing the stripe ordering is chosen as $\sqrt{2}a \times \sqrt{2}a \times c$ giving an ordering vector of $\boldsymbol{g} = (2\epsilon, 0, 1)$.

5.2 The $La_{1.6-x}Nd_{0.4}Sr_xCuO_4$ compounds

Sr=0.12

The sample studied by neutron scattering in Refs. [64, 65] was also studied by hard x-ray diffraction. The results for the $x = \frac{1}{8}$ sample are given in **Paper 5**. The primary results of this study was a confirmation of the existence of scattered radiation at the same location in q-space as observed with neutrons, and also weaker scattering from other locations consistent with the stripe model at (2±2ϵ, 2, $\frac{1}{2}$) and (1+2ϵ, 1, $\frac{1}{2}$). l-scans established that the charge-ordering unit cell is doubled along the c-axis, showing that there is a correlation between the next-nearest layers. Furthermore the temperature dependence was confirmed, and a peak broadening when entering the LTO phase was observed. The last observation could be interpreted as dynamic stripe correlations surviving in the LTO phase.

Additional l-scans with a slightly different crystal orientation from that used in Paper 5 were later performed: the ab plane was in the horizontal plane, and l-scans were performed perpendicular to the ab plane. This gives a reduced resolution but the scattered signal is now integrated along l. The results are shown in Fig. 38. Again we see superstructure reflections at $\pm\frac{1}{2}l$ that disappear with temperature. The intensity vanishes at ∼60K. One also observes enhanced scattering at $-\frac{5}{2}l$, but nothing at $-\frac{3}{2}l$. The intensity minimum at $l = 0$ is due to the minimum scattering of acoustic phonons at this symmetry point. A weak trace of the signal at $-\frac{5}{2}l$ can also be seen in Fig. 3 in Paper 5.

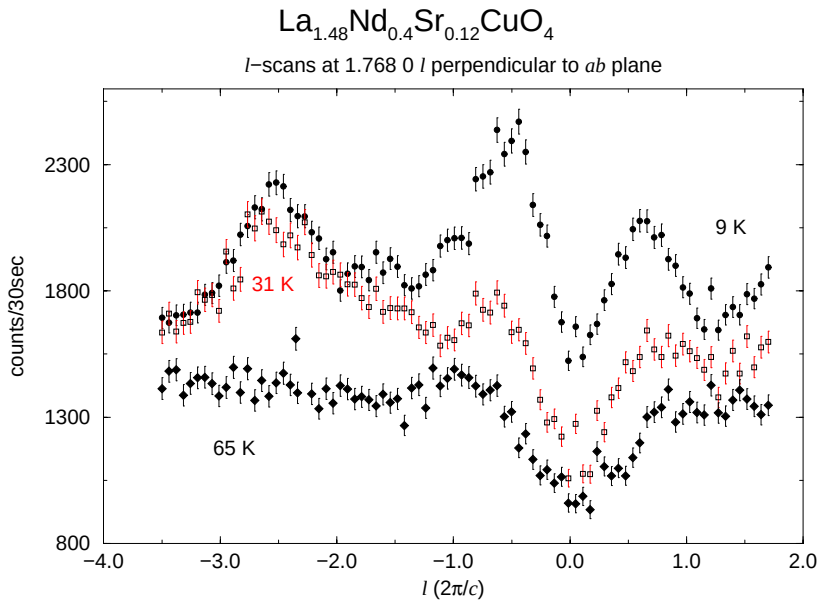

Figure 38. l scans perpendicular to the ab plane at the (0,2-2ϵ,l) superstructure position taken at 9, 31 and 65K.

Sr=0.15

Incommensurate magnetic peaks with $\epsilon = 0.13$ were measured with neutrons in this sample [70], and extremely weak traces of scattering were observed at (2+2ϵ,0,0), i.e. the position expected for charge scattering. The sample was investigated by hard x-rays, and temperature-dependent superstructure reflections were found at (2-2ϵ,0,$\frac{1}{2}$) and (0,2-2ϵ, $\frac{1}{2}$), with $\epsilon = 0.13$. Transverse and longitudinal scans are shown in Figs. 39,40. The temperature dependence is plotted in Fig.

41 together with the intensity of the (3 0 0) Bragg reflection, which is allowed in the LTT phase and forbidden in the LTO phase. The stripe correlations are seen to disappear around 60K. This is approximately 10K below the LTT-LTO transition and also a little lower than for the $x = 0.12$ sample, pointing to a suppression of static stripe pinning when the hole doping is larger than $\frac{1}{8}$. The temperature for the onset of charge stripe formation is higher than the onset of spin ordering [70], consistent with a charge-driven stripe ordering. For all these scans the sample was mounted with the c-axis almost vertical, so the scattered radiation was integrated along l.

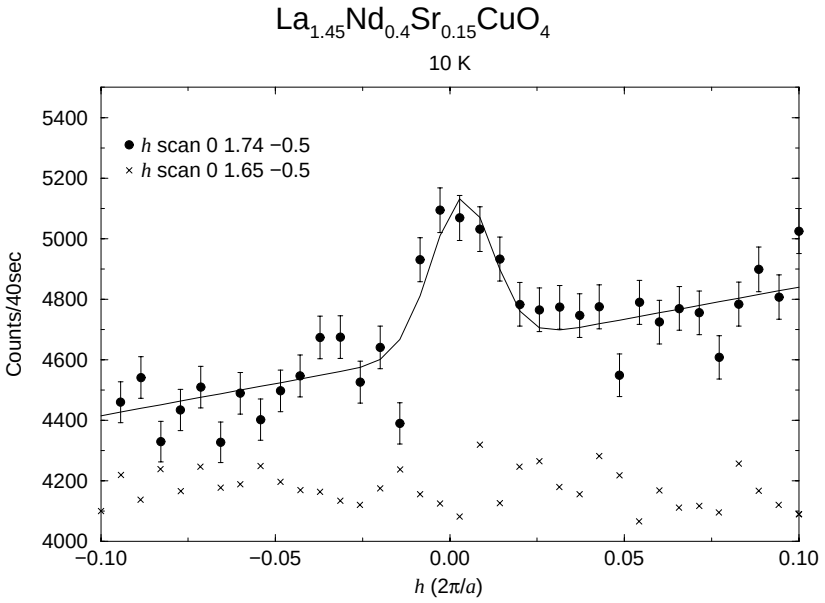

Figure 39. Transverse scan at the charge order peak position (circles) and slightly off the peak position (crosses). Temperature 10K.

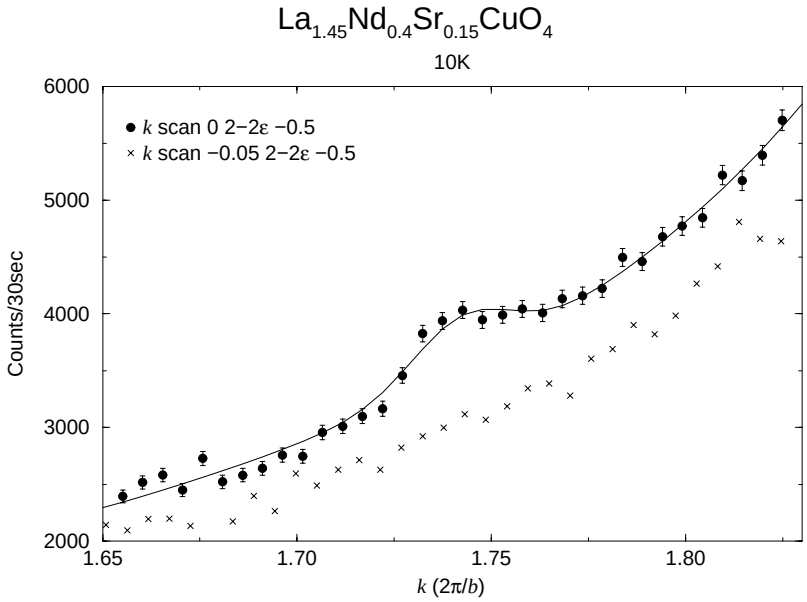

Figure 40. Longitudinal scan at the charge order peak position (circles) and slightly off the peak position (crosses). Temperature 10K.

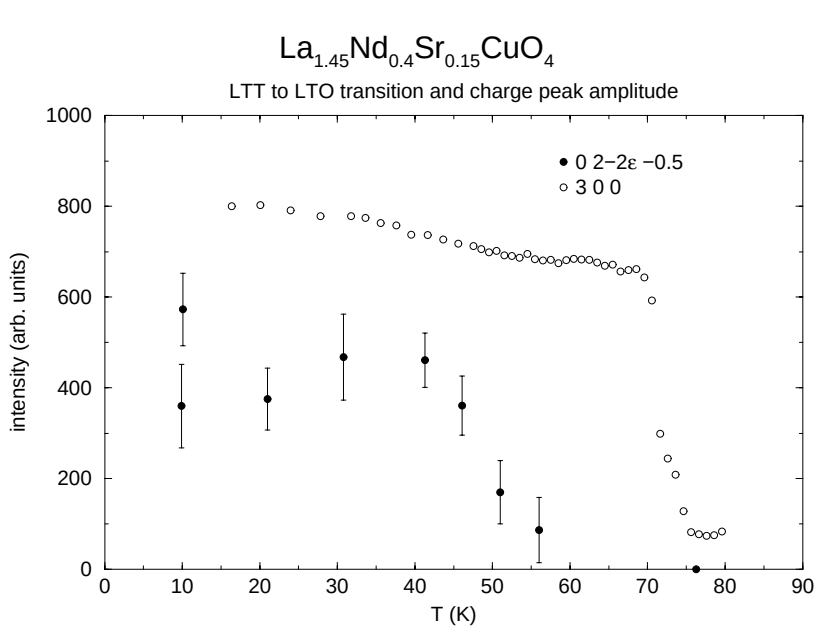

Figure 41. Temperature dependence of the superstructure reflections (full circles) and of the (3 0 0) reflection (open circles).

Naturally it would be interesting to follow the c-axis correlations as a function of temperature, as this so far haven't been done on any of the cuprates. The crystal was tilted so the scans could be performed in the bc-plane with optimum resolution, integrating along a. An l-scan of the (0,2-2ϵ,l) reflection is shown in Fig. 42, seemingly showing the same l dependence as for the x=0.12 sample. The temperature dependence is however by first sight confusing, see Fig. 43. Here the intensity is increasing linear with temperature up to 300K. An obvious guess would be that we are observing scattering by phonons instead of charge stripes. With x-ray scattering we are integrating over all phonon frequencies, and if $I(\boldsymbol{\kappa})_{dyn}$ is the scattered intensity including thermal diffuse scattering, it can be shown [71] that it can be written as a sum of zero-order, first-order, second-order, etc. intensities:

$$I(\boldsymbol{\kappa})_{dyn} = I_0(\boldsymbol{\kappa}) + I_1(\boldsymbol{\kappa}) + I_2(\boldsymbol{\kappa}) + ... \tag{5.4}$$

$I_0(\boldsymbol{\kappa})$ is the intensity from elastic Bragg scattering given by

$$\begin{aligned} I_0(\boldsymbol{\kappa}) &= N^2|f(\boldsymbol{\kappa})|^2\delta(\boldsymbol{\kappa}-\boldsymbol{\tau})\mathrm{e}^{-2W(\boldsymbol{\kappa})} \\ &= I(\boldsymbol{\kappa})_{static}\mathrm{e}^{-2W(\boldsymbol{\kappa})} \end{aligned} \tag{5.5}$$

where N is the number of atoms, $f(\boldsymbol{\kappa})$ is the atomic scattering factor, $\boldsymbol{\kappa}$ and $\boldsymbol{\tau}$ is the scattering vector and reciprocal lattice vector, respectively, and the exponential factor is the *Debye-Waller factor* given by

$$2W(\boldsymbol{\kappa}) = \frac{1}{Nm}\sum_{\boldsymbol{q}_j}|\boldsymbol{\kappa}\cdot\boldsymbol{\varepsilon}_{\boldsymbol{q}_j}|^2\frac{E(\boldsymbol{q}_j)}{\omega_j^2(\boldsymbol{q})} \tag{5.6}$$

Here m is the mass of the atom, $\boldsymbol{q}_j$ is the phonon wave vector with j indicating the polarization state, $\boldsymbol{\varepsilon}_{\boldsymbol{q}_j}$ is the polarization vector of the phonon, $\omega_j(\boldsymbol{q})$ is the phonon frequency and $E(\boldsymbol{q}_j)$ is the mean energy of the phonon. The term $I_1(\boldsymbol{\kappa})$ in equation (5.4) describes the *one-phonon* scattering process, $I_2(\boldsymbol{\kappa})$ the *two-phonon* scattering etc. The one-phonon term is usually dominating, and it can be written as

$$I_1(\boldsymbol{\kappa}) = \frac{N}{m}|f(\boldsymbol{\kappa})|^2 \mathrm{e}^{-2W(\boldsymbol{\kappa})} \sum_j |\boldsymbol{\kappa}\cdot\boldsymbol{\varepsilon}_{\boldsymbol{q}_j}|^2 \frac{E(\boldsymbol{q}_j)}{\omega_j^2(\boldsymbol{q})} \tag{5.7}$$

with $\boldsymbol{q} = \boldsymbol{\tau} - \boldsymbol{\kappa}$. The scans in Figs. 42,43 could be well fitted by the above expression using only the one-phonon term $I_1(\boldsymbol{\kappa})$.

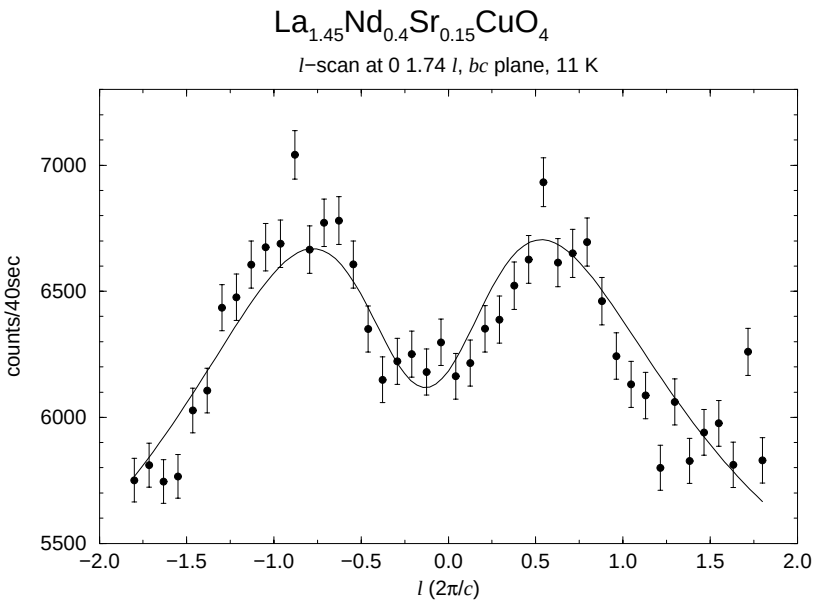

Figure 42. l scan in the bc plane at the (0,2-2ϵ,l) superstructure position. Temperature 11K. The line is a fit with equation (5.7).

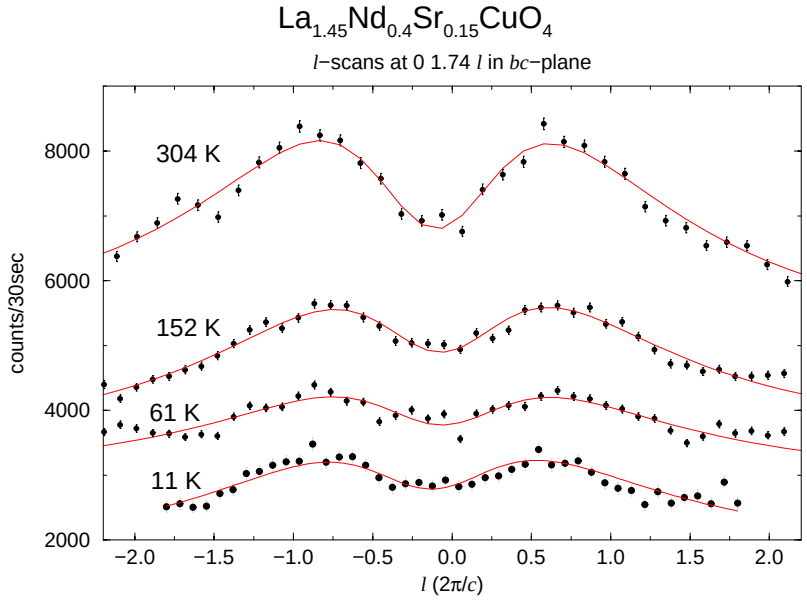

Figure 43. l scan in the bc plane at the (0,2-2ϵ,l) superstructure position. Temperature from 11K to 304K. The scans are displaced vertically to avoid overlap. Lines represent fits with equation (5.7).

In summary we observe charge peaks when integrating along l, but only phonon scattering when integrating along h, k, i.e., all l-scans must be performed with bad resolution, or we see only phonons. Superconductivity in this sample is suppressed with a T_c of 10K.

Note added: Very recent measurements on the Sr=0.15 sample [72] with an integration along l show peaks at $l = \pm\frac{1}{2}$ and nothing at $l = -1.5$.

Sr=0.12, Zn=0.02

A partial substitution of Zn for Cu is known to suppress superconductivity in $La_{2-x}Sr_xCuO_4$ and $YBa_2Cu_3O_{6+x}$, and it has been suggested that the Zn dopants might pin dynamical stripe correlations. Neutron scattering studies show that the magnetic scattering from Zn-doped $La_{2-x}Sr_xCuO_4$ and $YBa_2Cu_3O_{6+x}$ are consistent with the idea of pinning (references 83-85 in Ref [66]). A Zn-doping of 0.02 is just about where superconductivity is completely suppressed. A crystal of composition $La_{1.88}Sr_{0.12}Cu_{0.98}Zn_{0.02}O_4$ was investigated with hard x-rays. Magnetic peaks have been observed with neutrons in this sample [73], but despite *very* careful search we did not observed any trace of charge stripes at any of the expected positions.

5.3 Superstructures in $La_{2-x-y}Eu_ySr_xCuO_4$

Unlike Nd^{3+}, Eu^{3+} has no magnetic moment and will therefore not introduce any additional moments in the CuO_2 planes. Stripe ordering in Eu-doped samples would therefore not originate from effects induced by magnetic dopants, but should reflect the intrinsic properties of the material. Furthermore, the ionic radius of Eu is smaller than for Nd, and by making an Eu-substitution on the La site instead of a Nd substitution, the LTT phase is stable up to considerably higher temperatures (130K). As the charge-peaks seem to disappear around the LTT-LTO transition it is difficult to say if and how the charge ordering is related to the structural transition itself. By shifting the LTT-LTO transition temperature to a higher value, it may be possible to investigate if the charge ordering is following the structural transition temperature.

The Eu-doping level should not exceed $y \approx 0.2$ as the compound otherwise becomes structurally unstable. A sample of composition $La_{1.68}Eu_{0.20}Sr_{0.12}CuO_4$ (x=0.12, y=0.2) was studied for charge ordering. No neutron measurements of magnetic or charge ordering have been performed on this sample, as Eu unfortunately is highly absorbing to thermal neutrons.

A scan through the expected superstructure positions in reciprocal space quickly revealed surprisingly strong features. Longitudinal and transverse scans are shown in Fig. 44a,b. The reflections have a 2ϵ value of 0.265, which is a little higher than expected for a Sr doping of x=0.12.

The l dependence also shows how the superstructure reflections peak close to $l = \pm\frac{1}{2}$ (Fig. 45). The fit is two Gaussians. Unlike in the Nd-doped sample with Sr content of x=0.15 the superstructure reflections were so strong that the l scans could be performed in the *bc*-plane as transverse scans with good resolution. Both superstructure intensity and signal-to-background ratio are 40 times higher than in the Nd-doped x=0.12 sample.

Superstructure reflections were found at (h, k)=(2±2ϵ,0) (0, -(2-2ϵ)) (1-2ϵ, -1) (1, -1-2ϵ) (1+2ϵ, -1) (3+2ϵ, -1) and (1, -(1-2ϵ)). It is not as unambiguous to give the l positions also. While the l dependence follows the, by now, well known trend

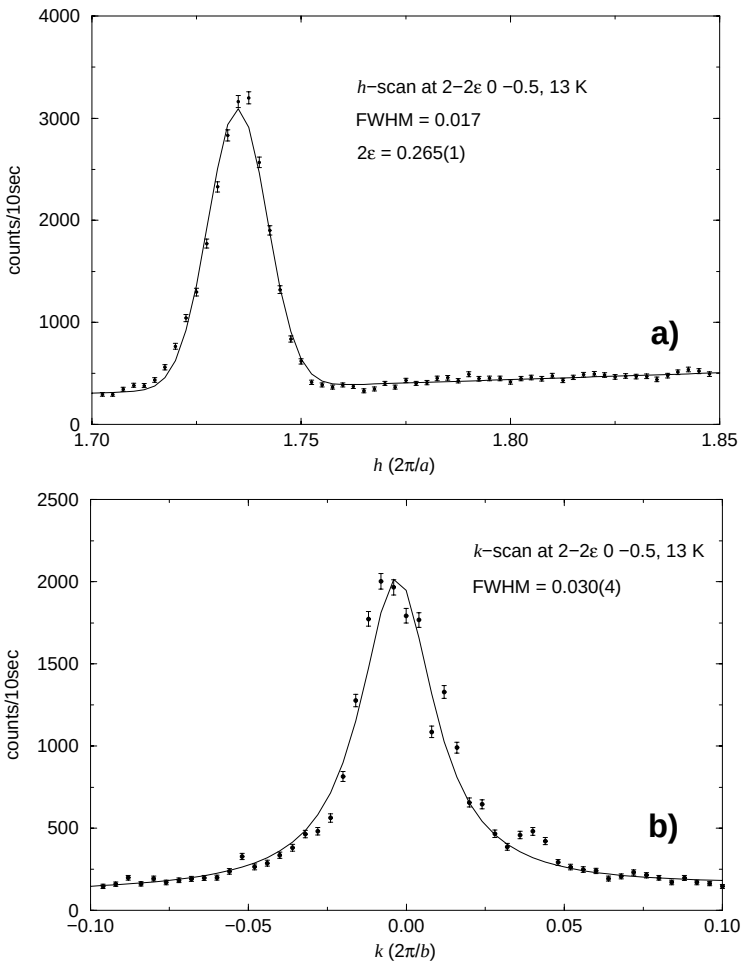

Figure 44. Longitudinal (a) and transverse (b) scans at the charge order peak position. Temperature 13K.

by peaking at $\pm\frac{1}{2}$ for the reflection shown in Fig. 45 a quite different dependence was seen at (2+2ϵ, 0, l). Here the superstructures peak at $l = \pm 0.3$, perhaps with some additional broader and less intense peaks at $l = \pm 0.8$.

The temperature dependence also revealed surprises. The integrated intensity does not decrease significantly with increasing temperature, as seen in Fig. 47. Even at temperatures as high as 460 K the superstructure reflections persisted.

The relative intensities of the charge-order peaks compared to the closest Bragg peak $\frac{(2-2\epsilon,0,\frac{1}{2})}{(2\ 0\ 0)}$ are listed for the investigated samples in Table 3.

Nd: y	Sr: x	rel. intensity
$y = 0.4$	$x = 0.12$	$9 \cdot 10^{-8}$
$y = 0.4$	$x = 0.15$	$3 \cdot 10^{-8}$
Eu: y	Sr: x	rel. intensity
$y = 0.2$	$x = 0.12$	$4 \cdot 10^{-6}$

Table 3. Relative intensity of the superstructure reflections compared to the closest Bragg peak.

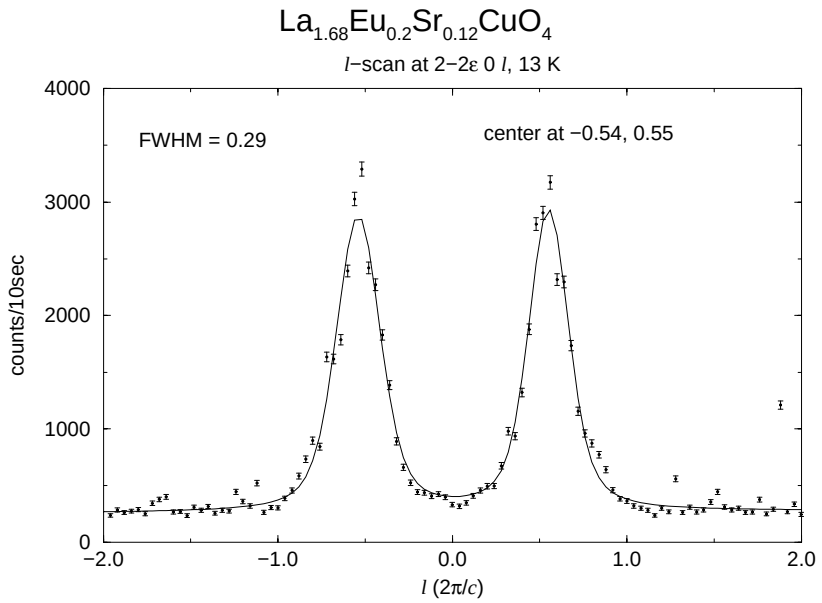

Figure 45. Transverse scan along l at (2-2ϵ,0,l). Temperature 13K.

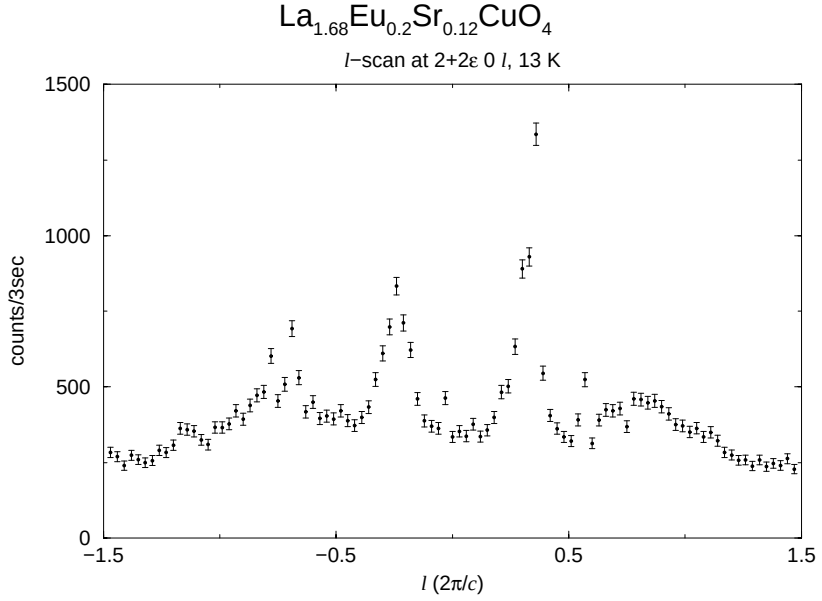

Figure 46. Transverse scan along l at (2+2ϵ,0,l). Temperature 13K.

5.4 Stripe phases?

The stripe-ordering model as proposed in Fig. 35c must be modified to include a stacking sequence along the c-axis with a next-nearest neighbor plane correlation in order to be consistent with the l dependence revealed by x-ray diffraction. Since the magnetic reflections peak at l=0 (cf. Fig. 9 in Ref. [65]) more modifications may be necessary. Taking these modifications into account the existing data for the Nd-doped samples with a Sr content of 0.12 and 0.15 are basically consistent with the stripe-ordering model. The same is not the case for the Eu-doped sample. Here the temperature persistent superstructure reflections do not easily comply with the

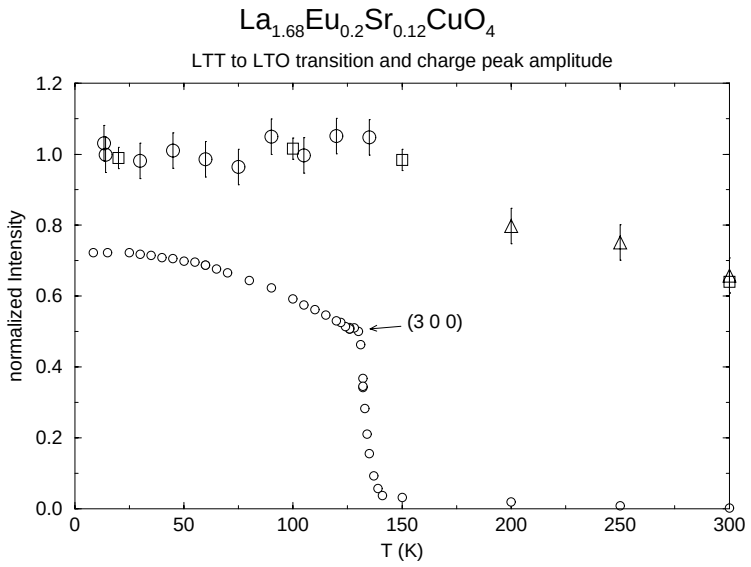

Figure 47. Temperature dependence of superstructure reflections. Large circles, squares and triangles correspond to l-scans, h-scans and k-scans, respectively. The (3 0 0) Bragg peak indicates the LTT-LTO transition.

idea of an interplay between electronic phase separation and the superconducting state. The pending question is now: are the features observed in the Nd-doped and Eu-doped samples of the same origin, or are the superstructures in the Eu-doped crystal merely an artifact with approximately the same symmetry as the proposed stripe phases?

A possible candidate for creating structural modifications that can give rise to superstructure reflections of the type observed here could be an ordering of the Sr dopants during the crystal growth. There are other examples of a rather long-range ordering of dopants in the cuprates; a well studied example is the modulation structures in the BSCCO compounds, and how they change with Pb doping [74] (the BSCCO compounds are described in section 6). Investigations by Simonov *et al.* on $La_{2-x}Sr_xCuO_4$ single crystals at various Sr dopings have shown that for some Sr concentrations the Sr atoms order on the La sites rather than occupying randomly distributed sites [75, 76] with a concomitant decrease in T_c. The T_c decrease was explained as coming from oxygen deficiencies induced by the Sr ordering. The ordering was observed for high doping levels with $x \approx 0.24$. To my knowledge no such studies have been performed on neither $La_{2-x}Ba_xCuO_4$ nor $La_{2-x-y}Nd_ySr_xCuO_4$.

Although the symmetry of the superstructures in the Nd-doped and Eu-doped samples are almost identical, the temperature dependencies are very different which strongly indicates that they are of different origin. As reported in Paper 5 the superstructure reflections in the Nd-doped samples do maybe not completely disappear at the LTT-LTO transition, but are broadened quite strongly in the LTO phase. The significance of this residual signal should not be exaggerated, as the peak intensity is very low and close to the detection limit, but it may be speculated if the superstructure intensity is completely disappearing with temperature, or if the LTO transition is merely broadening the diffuse scattering beyond the detection limit.

To resolve these questions more experimental work needs to be done. It would

be very interesting to attempt to detect magnetic neutron scattering from the Eu-doped lanthanate, and to gather structure-factor information at other $\boldsymbol{q}$ values in the Nd-doped samples. Also, given the relatively intense reflections in the Eu-doped sample it may be possible to record the diffraction pattern on a 2D detector, which would be an effective way to determine the symmetry of the superstructure on a much wider $\boldsymbol{q}$ range. Work is on progress on all these issues, and until we know the results any theories or arguments on the striped phases in the cuprates can only be of a speculative character.

Note added after proof. For the benefit of the interested reader I shall mention some recent x-ray measurements by Thomas Niemöller (April 1999) on a $La_{1.5}Nd_{0.4}Sr_{0.10}CuO_4$ crystal. This sample shows weak, temperature dependent reflections with $\epsilon \simeq 0.21$ that disappear at 64K, but it also shows much stronger temperature independent peaks with $\epsilon = 0.265$ as the ones observed in the Eu-doped sample, see Fig. 48. The l dependence of the strong peaks is also similar to the superstructure peaks in the Eu-doped sample with two peaks at $l = \pm 0.5$ at the (2-2ϵ,0,l) position and four peaks approximately at the $\frac{1}{3}$ positions at (2+2ϵ,0,l).

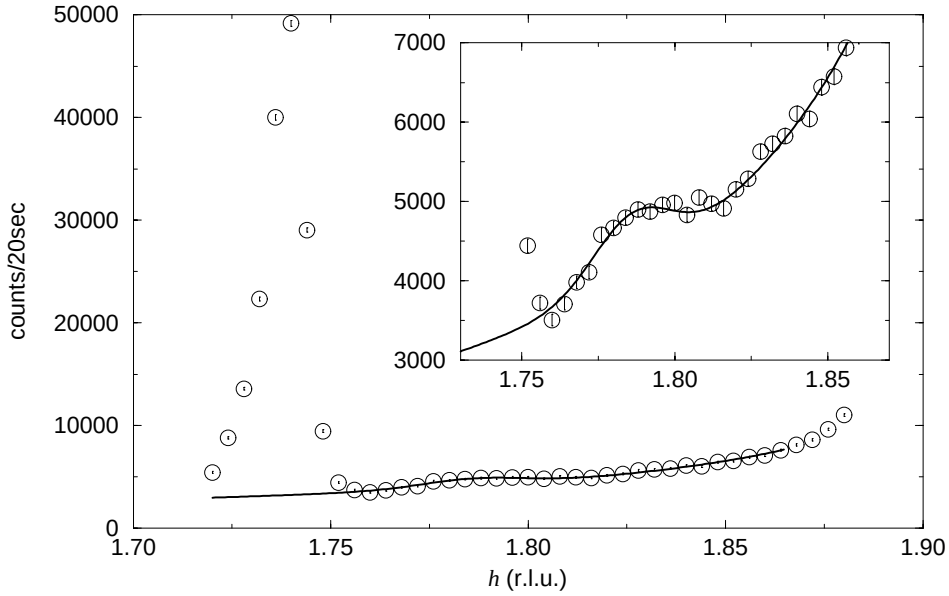

Figure 48. Superstructure reflections at (h,0,$\frac{1}{2}$) in a $La_{1.5}Nd_{0.4}Sr_{0.1}CuO_4$ sample. The insert is a magnification of the temperature dependent peak with $2\epsilon \simeq 0.21$. Temperature 13K.

These observations strongly implies that the strong peaks at $2\epsilon = 0.265$ in the Eu-doped sample and the stripe ordering superstructures in the Nd-doped compounds are of different origin.

6 BSCCO/Ag tapes

An obvious application of high-temperature superconductors is the use of superconducting wires for current transportation free of resistive energy loss. The high transition temperatures of the cuprates allows liquid nitrogen to be used as coolant, and this makes them immensely more economically attractive than the use of low-T_c superconductors which must be cooled by liquid helium. Making useful wires from the high-T_c materials is not a task without severe obstacles, however. The brittle ceramic nature of the cuprates makes the production and mechanical handling of long length wires difficult. Also, the complicated solid state chemistry and the two-dimensional nature of the cuprates pose major challenges to the development of wires with sufficiently high critical current densities. The main focus has been on the Powder-In-Tube technique (PIT) where a precursor power is filled into a metal matrix which is subsequently mechanically and thermally processed. This results in a so-called superconducting *tape* that, within certain limits, can be handled almost as a conventional wire.

Most research and development has been directed towards the bismuth-based high-T_c compounds $Bi_2Sr_2Ca_{n-1}Cu_nO_{2n+4+x}$ (BSCCO) that were discovered December 24, 1987. The BSCCO system has three structural phases for n=1,2,3: The $Bi_2Sr_2CuO_{6+x}$ phase (2201) with T_c $\leq$20K, the $Bi_2Sr_2CaCu_2O_{8+x}$ phase (2212) with T_c=85K and the $Bi_2Sr_2Ca_2Cu_3O_{10+x}$ phase (2223) with T_c =110K. The BSCCO compounds benefit from a rare combination of a high T_c and a low toxicity [77].

For all the high-T_c cuprates the superconducting properties are anisotropic. For BSCCO the anisotropy $\gamma = \xi_{ab}/\xi_c = H_{c2,ab}/H_{c2,c}$ is extremely high, of the order of 10^2-10^3 [78]. As a consequence hereof the CuO_2 layers are only weakly coupled, and the Flux-Line-Lattice tends to form disordered 3D "pancake" structures instead of a 2D columnar structure. The FLL melting temperature is very low causing energy dissipation at 77K even for very moderate fields.

Due to the highly anisotropic critical current ($j_{c,ab} \gg j_{c,c}$) c-axis tilt boundaries severely hamper the current flow. In order to obtain reasonable j_c values the c-axes of the BSCCO crystallites must be well aligned (well textured). Luckily the BSCCO grains are naturally flat with a micaceous morphology, and an uniaxial pressure will tend to align the grains by default. It is not possible to align the crystallites in the ab-plane, but this has much less influence on j_c. Normally the BSCCO compound is doped with lead; this facilitates the crystallization of the 2223 phase by increasing the temperature window for which the 2223 phase is stable. Also, the minimum temperature for which the transformation to the 2223 phase takes place is lowered. The lead substitutes Bi and has only little influence on the superconducting properties.

The Powder-In-Tube technique

The nominal composition of the precursor powder is an important research topic in its own respect

The PIT technique involves the following steps: a precursor powder containing the 2212 phase and additional secondary non-superconducting phases with a total nominal composition of the 2223 phase is filled into a silver tube. The tube is drawn to a long thin wire and rolled or pressed to a flat *tape* of typical cross section 4×0.2 mm^2. Alternatively the tube can be rolled flat directly by the use of profiled rollers. The tape is annealed at approximately 830 °C, whereby the 2212 phase reacts with the secondary phases to form the 2223 phase. The solid state reactions involve significant in- and outdiffusion of gaseous oxygen, and this is why Ag must be used as sheath material: at sufficiently high temperatures Ag becomes permeable to oxygen, and the necessary oxygen exchange is possible.

During the annealing the alignment of the c-axes is significantly improved which is also essential to the superconducting performance. The annealing procedure is mostly repeated with intermediate deformation steps.

One of the key points in obtaining high j_c values is the optimization of the thermal processing parameters. Both heating rate, annealing temperature, cooling rate and the oxygen partial pressure will influence the phase transformations and texture development. The end goal is a phase-pure 2223 core with a very good c-axis alignment. 2223 is thermodynamically unstable at lower temperatures [79], which makes the synthesis of a 100% pure 2223 phase exceedingly difficult. The performance of fully processed tapes is given by the *critical current* I_c, the *critical current density* j_c which is I_c divided by the cross section of the BSCCO core, and the *engineering critical current density* j_e defined as I_c divided by the total cross section of the tape, including both BSCCO and Ag. In the context of current transportation the values are almost always determined at 77K.

The first BSCCO tapes made were monofilamentary tapes with one continuous BSCCO core. Most tapes made today are of the multifilamentary type. Here a number of half-finished tubes are packed into a new Ag-tube which is subsequently drawn, rolled and annealed to make a tape containing many BSCCO filaments. The multifilamentary tapes offer several advantages: the critical current density is higher, defects in the individual filaments have less influence on the overall performance and they are less sensitive to mechanical handling. For research purposes both monofilamentary and multifilamentary tapes were investigated, as the monofilamentary tapes constitute a more simple system.

In-situ characterization of BSCCO tapes

To obtain an optimum thermal treatment a detailed knowledge of the solid state chemical reactions and the microstructure development is of utmost importance. The phase-space of tape processing is multi-dimensional, and every time one parameter is changed it may influence the entire phase- and texture development. An optimization of the process for a specific setting of the parameters might quickly turn out to be useless if any one of the processing steps are changed later. It is therefore highly desirable to obtain an understanding of the processes involved in the annealing procedure. In this way the optimization can be based on a knowledge of the basal mechanisms and reactions taking place, and if any processing steps at a later stage are changed it may be possible to adjust the other parameters accordingly with relative ease.

A major obstacle has been the silver cladding, which constitutes an effective shield against most experimental probes available for structural investigations. A complete removal of the silver cladding will of course open a window for structural investigations, but since the silver is known to have significant influence on the solid state chemistry and texture development in the BSCCO core [80] the information obtained from such *in-situ* studies will be of limited relevance. This is also why the information obtained from pressed pellets of BSCCO powder cannot be directly implemented for optimization of tape processing. Silver is absorbing to neutrons, and the count rates in neutron scattering experiments have been depressingly low [81]. Only recently *in-situ* investigations of the BSCCO core have been made with neutron diffraction [82], and this is only possible if special samples are prepared with a reduced amount of silver [82] or if the silver cladding is partially etched away [81]. Even so, the counting times of typically 40 minutes are rather long compared to the typical time constants when the transformations are running fast.

For x-ray investigations conventional photon energies of 10-20 keV do not posses the penetration power necessary to obtain acceptable detection rates in diffraction experiments on Ag-clad tapes. The use of high-energy synchrotron x-ray diffraction constitutes a unique tool for structural *in-situ* investigations of the BSCCO/Ag tapes. At 100 keV the penetration depth is 650 μm in Ag and 600 μm in pure 2223, and diffraction experiments can be performed in transmission geometry except when the incoming beam is almost parallel to the transverse direction. By using a furnace constructed from a low Z metal like Al the hard x-rays have sufficient penetration power to penetrate both furnace and tapes, and true *in-situ* characterizations of unmodified tape samples can be performed during annealing. The scattering angles will be small due to the short wavelength of the high-energy photons, and by using a two dimensional CCD detector of moderate size a considerable volume of reciprocal space can be covered in one single recording. The high photon flux permits exposure times of a few minutes which gives a high time resolution compared to the typical time span of several days for the annealing procedure.

For definition of the transverse direction (TD) and normal direction (ND) see Fig. 1 in Paper 6

6.1 Experimental setup, analysis and examples

The experimental setup and methods used for analyzing the 2D diffraction patterns are presented in **Paper 6**. The feasibility of the technique is demonstrated through examples and results from room temperature measurements and an *in-situ* experiment. The concentrations of the phases 2212, 2223, 2201 and $(Ca,Sr)_2PbO_4$ during annealing are shown in Fig. 49. We find that during heating the $(Ca,Sr)_2PbO_4$ additive dissolves at 820 °C. After approximately 19 hours of annealing at 835 °C there is no further development in the phase transformations from 2212 to 2223, and the 2212 phase is transformed 97.5%. During cooling there is an increase in both 2212 and 2223 concentrations and the secondary phases $(Ca,Sr)_2PbO_4$ and 2201 appear.

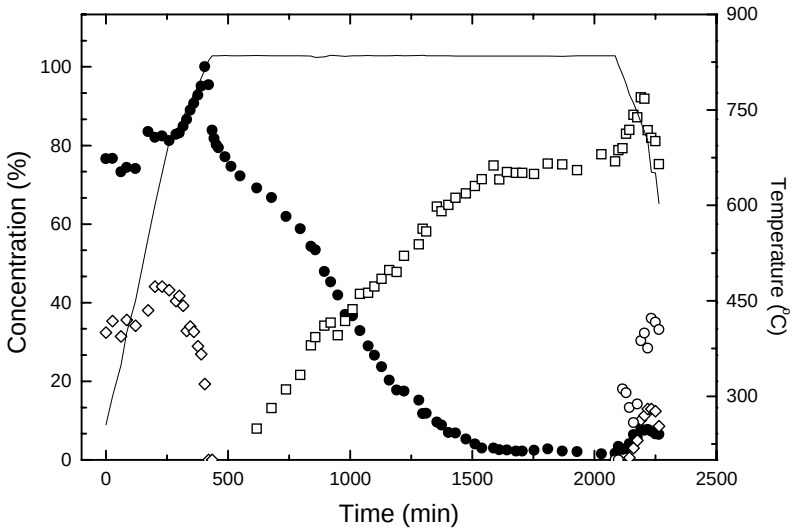

Figure 49. Relative concentrations of 2212 (•), 2223 (□), 2201 (○) and $(Ca,Sr)_2PbO_4$ (◇) during annealing. The 2201 concentration is multiplied by 10. The line marks the temperature profile with reference to the temperature scale at the right hand of the figure.

The texture is described by the FWHM of the *c*-axis angular distribution denoted $\Delta\alpha$; a low $\Delta\alpha$ value corresponds to a good texture. As shown in Fig. 50 the 2212 texture improves right from the beginning of the annealing procedure during the initial heating, with a sharp increase coinciding with the $(Ca,Sr)_2PbO_4$ dissolution temperature. The 2223 texture is essentially constant from the moment the phase starts to nucleate, and the final 2212 and 2223 textures are identical.

See also Paper 6 for definition of $\Delta\alpha$

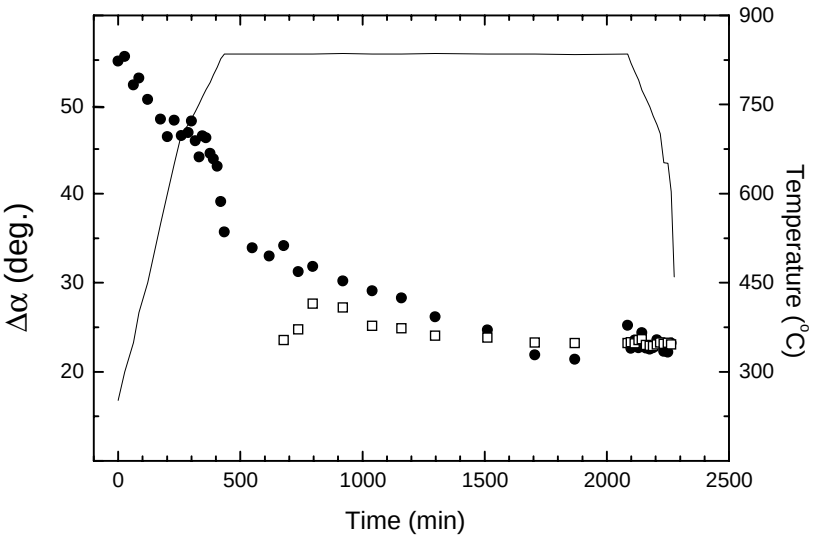

Figure 50. The width (FWHM) of the c-axis misalignment angle $\Delta\alpha$ *for the 2212 (●) and 2223 phases (□). The line marks the temperature profile.*

6.2 Detailed analysis of *in-situ* experiment

A detailed analysis of the data obtained from the first *in-situ* experiments can be found in **Paper 7**. The appearance of a $(Ca,Sr)_2CuO_3$ phase is observed when the operating temperature is reached. The variation of the 2θ midpoint of the 2212 (1 1 5) reflection is shown in Fig. 51. The lattice expansion during the annealing procedure cannot be explained solely by thermal expansion. We interpret this as stoichiometric changes in the Pb and/or Ca content with Pb entering the 2212 structure during the last part of the initial heating ramp and a steadily decreasing Pb and/or Ca content in the 2212 phase during the annealing.

From Avrami plots of the transformation kinetics and lack of strain or finite-size broadening in the 2212 phase during the transformation (Fig. 52) we find that only a few 2212 grains transform at a given time. This sets restrictions for the various transformation mechanisms possible. The most probable transformation consistent with our experimental findings is a nucleation-and-growth model that involves a fast decomposition of the individual 2212 grains, followed by a growth of the 2223 phase from 2212 melt reacting with $(Ca,Sr)_2CuO_3$.

6.3 Phase reactions

A very slow heating ramp followed by fast heating steps was used to investigate equilibrium phenomena and kinetics of the phase reactions in a BSCCO/Ag tape. The results are presented in **Paper 8**. For the first time, the concentration of a partial liquid is directly monitored. The reactions between the BSCCO phases and

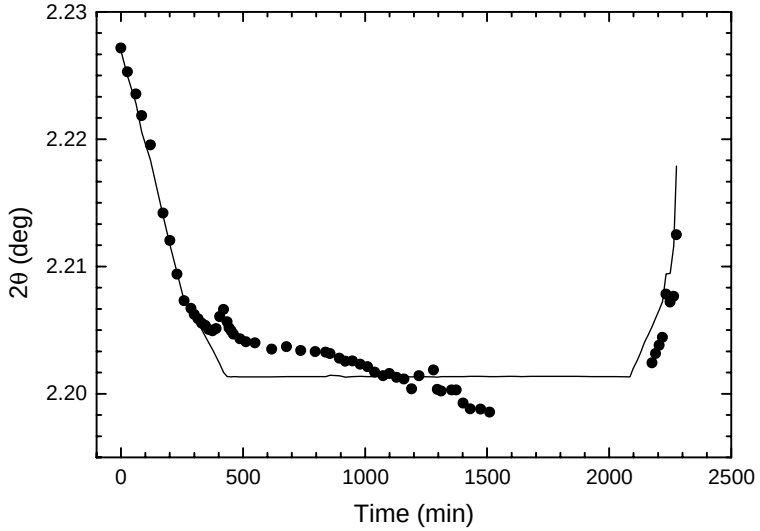

Figure 51. The lattice expansion of the 2212 phase during in-situ annealing. Data points are left out when fitting becomes unreliable, due to vanishing intensities. A theoretical curve based on a shift caused only by thermal expansion is shown as a line.

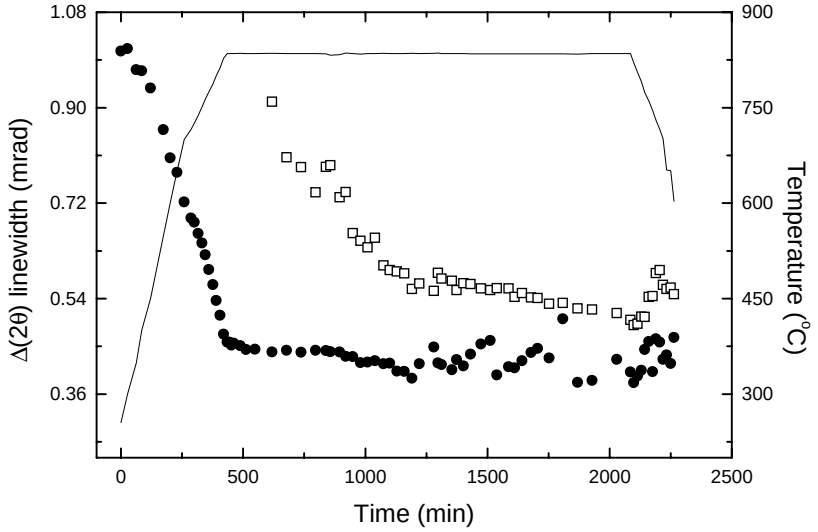

Figure 52. Evolution of the x-ray line-widths with the 2θ FWHM of 2212 (•) and 2223 (□) shown. The data points are not corrected for an instrumental broadening of estimated width 0.35 mrad. The erratic behaviour of the Bi-2212 data between 1200 and 2000 minutes is an artefact of the fitting caused by the low concentration of this phase in this region.

secondary phases $(Ca,Sr)_2PbO_4$, $(Ca,Sr)_2CuO_3$, the "3321" phase and the liquid phase are shown in Fig. 53. By cycling the temperature at elevated temperatures, fast, quasi-reversible changes are observed, and the incorporated Ca and/or Pb is lost irreversibly.

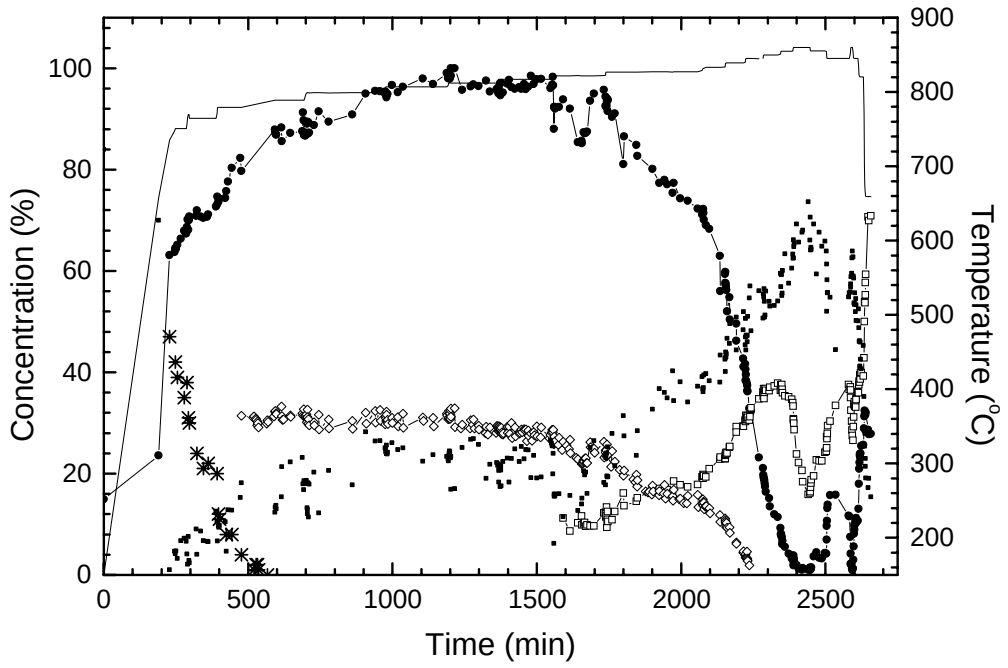

Figure 53. Relative concentrations of 2212 (•), 2223 (□) and $(Ca,Sr)_2PbO_4$ (◇) during annealing. Points proportional to the amounts of 3321 and liquid in the tape are marked by (∗) and (■), respectively. The line marks the temperature profile with reference to the temperature scale at the right hand of the figure.

6.4 Flux penetration and microstructure of BSCCO tapes

In order to improve the critical current the current limiting factors must be identified. We must distinguish between the *intragrain* critical currents, i.e., the current density within a single BSCCO grain, and the *intergrain* critical currents, i.e., the current density across grain boundaries. The *intragrain* critical current density is limited by T_c and the pinning of the flux lines, while the *intergrain* critical current density is also limited by the grain connectivity and the c-axis misalignment angle. Non-superconducting secondary phases and weak links or cracks in the ceramic core can also reduce I_c. While a high critical current is the end goal in tape processing, a measurement of the critical current alone does not tell us how we should proceed to improve the quality of the tape.

We have combined magneto-optical (MO) imaging and hard x-ray diffraction to investigate the influence of various tape deformation procedures and annealing steps. The tapes were produced in two ways: either by drawing and rolling the Ag tube containing the precursor powder, or by rolling the tube directly using profiled rollers followed by uniaxial pressing.

Sample preparation

Results for three monofilamentary tapes will be shown. The samples referred to as I, II and III have been processed the following way:

- Tape I has been drawn, rolled, annealed, rolled and annealed again
- Tape II has been profile rolled, annealed, pressed and annealed again
- Tape III has been profile rolled and annealed once

The dimensions and critical currents determined by transport measurements are shown in Table 4. For sample I the BSCCO core was ~ 3.1 mm wide, for sample II and III the core was ~ 3.3 mm wide. The T_c determined by magneto-optics was 105-107K for all the tapes.

Dealing with samples of almost identical dimensions I have not made any effort to distinguish between I_c and j_c

Tape thermomech. processing	Width (mm)	Thickness (μm)	I_c (A)
I : drawn, rolled, annealed twice	3.5	160	23
II : rolled, pressed, annealed twice	4.5	200	33
III : rolled, annealed once	4.5	230	12

Table 4. Tape dimensions and critical current at 77K.

In order to obtain a high spatial resolution in the MO measurements the Ag sheathing was ground away to expose the BSCCO core. The tape was cast into resin to facilitate the handling and grinding was done in three steps starting with coarse grinding cloths and ending with fine grinding cloths. Approximately half the tape was ground away exposing the central part of the ceramic core. The resin was removed by acetone and the tape was glued to a small Cu-plate with low-temperature varnish and mounted on the cold finger of the MO cryostat (see Fig. 11). The magnetic field was applied perpendicular to the tape surface, i.e., parallel to the preferred c-axis orientation.

Pieces cut from the same tapes investigated by MO imaging were characterized by hard x-ray diffraction at room temperature, using the setup described in Paper 6. The angle ω was 75°.

For definition of ω see Fig. 1 in Paper 6

Magneto-optical results

Images were recorded at 15K and 77K. The field shielding behavior of the tapes was qualitatively the same at the two temperatures, but quantitatively the field shielding properties were reduced an order of magnitude going from 15K to 77K. The contrast in the images is better at 15K because of the larger fields used, and mainly 15K results will be presented.

Field penetration in sample I (drawn and rolled) at 15K and 77K is shown in Fig. 54. At low fields (2.5 mT, 15K) the entire tape is shielding off the applied field, meaning that all the grains are electrically coupled and a supercurrent is flowing freely throughout the sample. As the field is increased the flux is penetrating from the edges in accordance with the Bean model, and a quasi-periodic defect structure is seen with cracks running towards the center. Where the field has penetrated a large number of dark grains are seen. The individual dark spots have dimensions of 15-30 μm which is the size reported for 2223 grains in annealed precursor powders investigated by SEM [83, 84]. We therefore interpret the dark spots as the 2223 crystallites being closest to the MO indicator film. A substantial part of the tape is still shielding off the applied field at 50 mT, and the remanent state was obtained after penetration with 100 mT. The last image showing field penetration at 77K should be compared to the first image at 15K.

The field penetration in sample II (rolled and pressed) is shown in Fig. 55. The large crack running across the tape is not representative of the sample, and should be disregarded. A defect structure as in tape I with small cracks running from the edge towards the center is not seen, only the grain structure. For $B \geq 38$ mT the field has penetrated the entire tape indicating that all the BSCCO grains are decoupled and there can be no net transport of supercurrents through the tape.

I dropped it on the floor

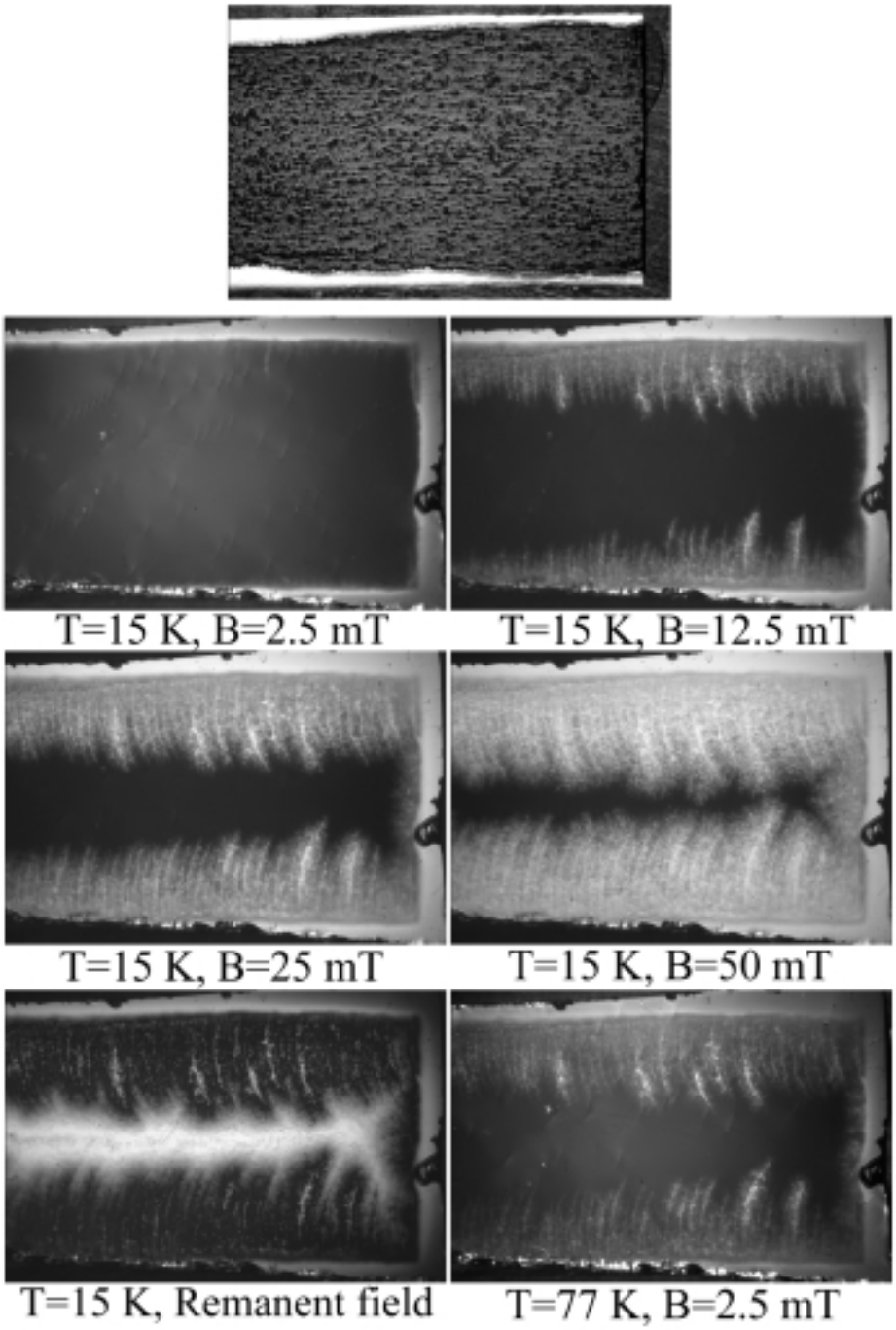

Figure 54. Flux penetration in tape I (drawn and rolled) after zero-field cooling. Temperatures and applied fields are given below each image. Top image is a direct picture of the grinded tape. The defects visible in the MO images are not seen in the direct picture. The rolling direction is from right to left in the images. For all images the width corresponds to 5.6 mm.

Field penetration in tape II and III is compared in Fig. 56. Tape III, which had been annealed only once, does clearly not shield off the field as effectively as tape II. At 4 mT only a minor central part of tape III has not been penetrated by the flux, while the major part of tape II is flux free. Compare also with Fig. 55. Again there are no signs of a defect structure as in tape I.

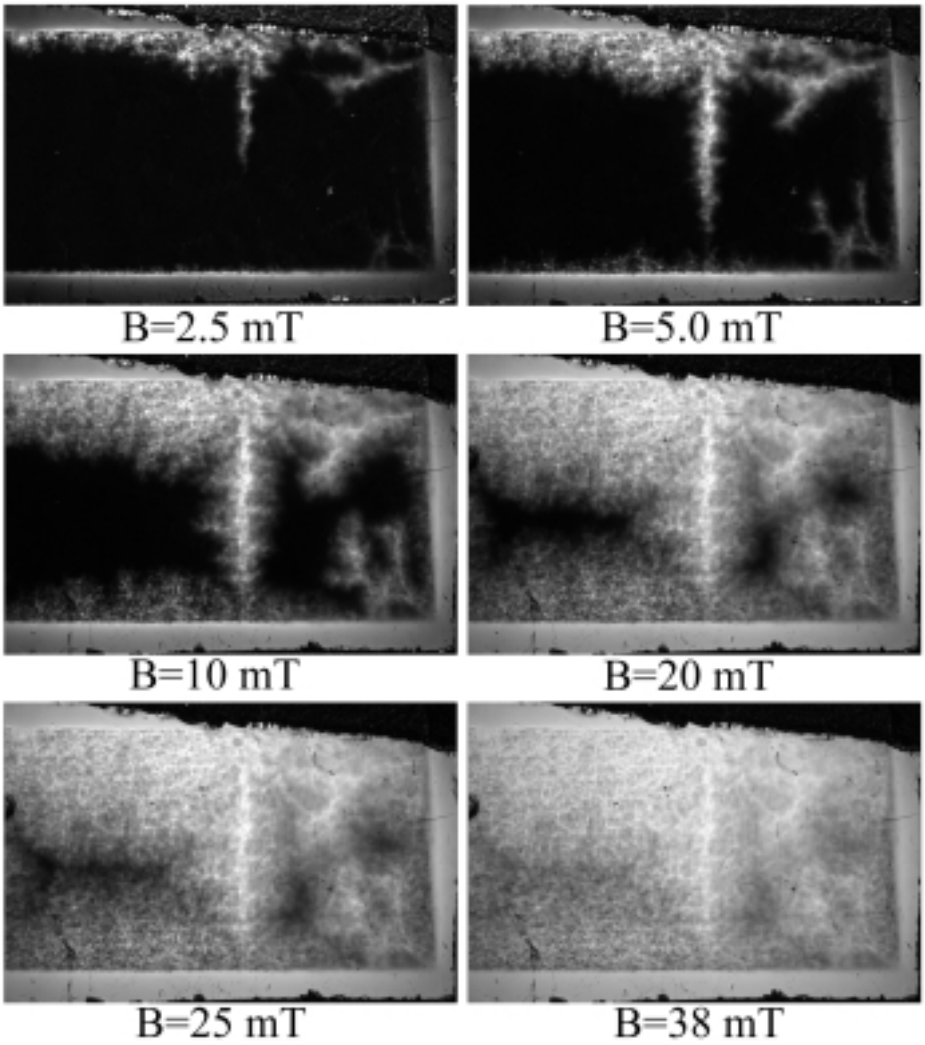

Figure 55. Flux penetration in tape II (pressed tape) after zero-field cooling. All images are taken at 15K. For all images the width corresponds to 5.6 mm.

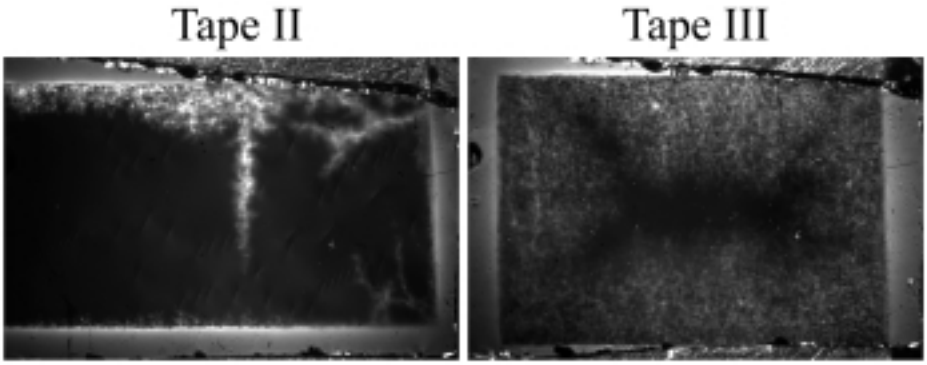

Figure 56. Flux penetration in tape II and III at 15K with an applied field of 4 mT.

As an attempt to distinguish between the *intragrain* and the *intergrain* critical currents a single grain was selected near the edge of the tape, and the grey level intensity as function of applied field was determined. As the flux always penetrates from the edges, according to the Bean model (cf. chapter 1.3), the grains near the

edge are the first to become electrically decoupled, and the shielding here is governed by the intragrain j_c. The same analysis was performed in the tape center where the flux was completely shielded off for low field values. Here the shielding strongly depends on the intergrain j_c. The results are shown in Figs. 57a,b.

This analysis is only valid because the samples have almost identical dimensions.

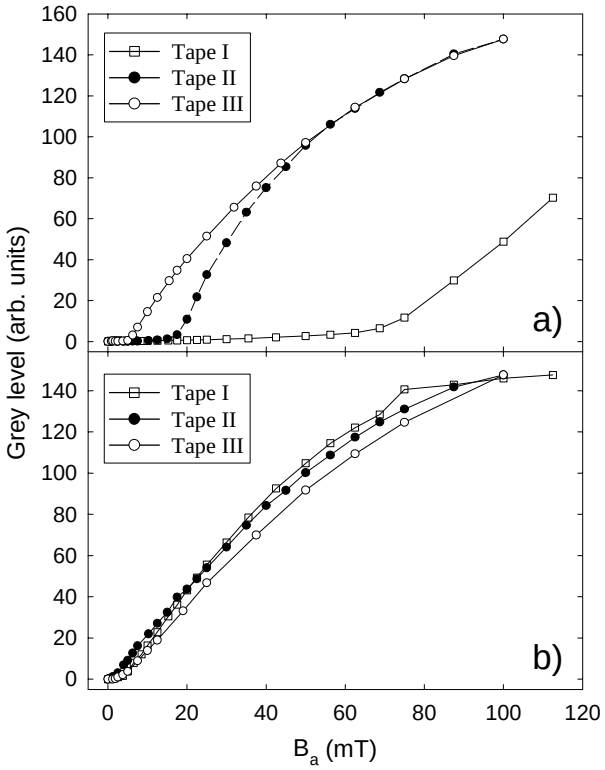

Figure 57. Applied field versus grey level recorded at a) the tape center (intergrain) and b) the tape edge (intragrain).

X-ray results

The diffraction patterns were analyzed as described in Paper 6. The concentrations were determined from the integrated intensities of the (1 1 5) reflections using the constraint $C_{2212}+C_{2223}+C_{2201}=100\%$. The structure factors are not known precisely for the 2223 phase, but referring to Table I in Paper 6 the integrated intensity of the 2223 (1 1 5) reflection must be multiplied with ≈ 1.47 in order to estimate the relative concentrations. Results of the analysis are shown in Table 5. The intensities can only be compared on a relative scale.

The radial linewidth $\Delta 2\theta$ and c-axis texture $\Delta\alpha$ for the 2212 and 2223 phases are listed in Table 6. Note that the 2212 and 2223 textures are almost identical, in agreement with the findings in Paper 6. The diffraction patterns from tape I and tape II are shown in Fig. 58. Notice that for tape II the powder ring of the 2212 phase is quite diffuse while for tape I it is more grainy, implying that there is a relatively limited number of 2212 grains in tape I. Referring to tables 5 and 6 we see that the 2212 concentration is approximately the same in the two tapes, and the $\Delta 2\theta$ linewidth of the 2212 phase is more narrow for the rolled tape. From this we may conclude that there are fewer but larger 2212 grains in the rolled tape (tape I) than in the pressed tape (tape II).

Tape	Integrated Intensities			Concentration (%)		
	Bi-2201	Bi-2212	Bi-2223	Bi-2201	Bi-2212	Bi-2223
I	7.9	82	217	1.9	20.0	78.0
II	14.3	67	194	3.9	18.3	77.8
III	13.5	46.3	179	4.2	14.3	81.5

Table 5. Integrated intensities and phase concentrations for tapes I-III.

Tape	$\Delta 2\theta$ (mrad)		$\Delta\alpha$ (deg)	
	Bi-2212	Bi-2223	Bi-2212	Bi-2223
I	0.44	0.49	24.6	22.7
II	0.51	0.51	33.5	29.3
III	0.64	0.58	31.8	30.0

Table 6. Microstructural properties of tapes I-III determined from the (1 1 5) reflections.

Discussion

Looking first at tape II and III the I_c is increased by almost a factor of three by the extra pressing and annealing step, cf. Table 4. This is also reflected in Figs. 56 and 57a (intergrain shielding) showing a strong increase of the flux shielding abilities. There is no significant difference between the tapes in Fig. 57b (intragrain shielding) which we may take as a sign that the intragrain j_c has not improved substantially by the extra annealing step. Looking at the structural properties there are no major differences in the phase composition and texture for tape II and III, cf Table 5 and 6. The only difference is in the $\Delta 2\theta$ linewidth, which indicates that a grain growth has taken place. We may conclude that the effect of an extra pressing and annealing step is to increase the intergrain connectivity, and possibly also to reduce the number of grain boundaries by a grain growth.

Comparing tape I and II we find from the MO images that tape I has superior j_c on a local scale, cf. Figs. 54 and 57a, but this is not reflected in the transport critical current I_c. The slightly smaller dimensions of tape I compared to tape II,III (Table 4) cannot account for the difference in I_c, and the obvious current limiting factor must be the defect structure that is running almost perpendicular to the current path. Judging from the remanent state in Fig. 54 the effective current carrying cross section is only $\frac{1}{4}$ of the width of the ceramic core, and without the

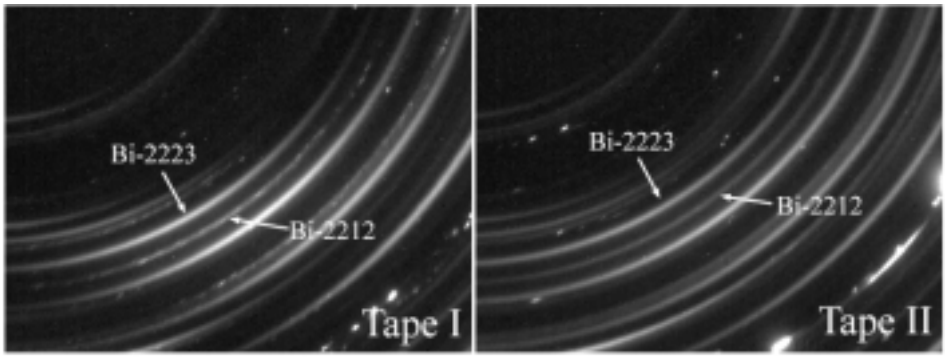

Figure 58. Diffraction images of tapes I and II. The (1 1 5) reflections for the 2212 and 2223 phases are indicated by the white arrows.

defects I_c would be enhanced by a factor of three to four.

The cross section of the ceramic core is elliptic rather than rectangular, so I_c does not scale directly with the core width

The large difference of the superconducting properties for tape I and II,III can be related to the structural properties: The texture is considerably better in tape I and the 2201 content is smaller (it is known that the 2201 phase has greater importance than the 2212 phase as a current limiting factor [85]). In tape I there are fewer but larger 2212 grains as discussed previously, and this might also have a beneficial influence in form as a reduced number of grain boundaries. It could be argued, however, that this would mainly effect the current flow at low temperatures where the 2212 phase is highly superconducting, while at LN_2 temperature the 2212 grains themselves may act as weak links.

From our data we conclude that

- The grey level analysis indicates that the intragrain j_c, i.e. the flux pinning, is approximately the same for the three tapes. Comparing tape II and III the extra annealing step apparently only improves flux pinning very little or none at all.
- The 2212/2223 phase purity is less important than the 2201 content and/or the *c*-axis texture. From our data alone we cannot say whether the 2201 phase or the texture is the more important current limiting parameter.
- The defects in tape I is a major current limiting parameter. On a local scale the tape has superior superconducting properties.
- Deformation by profile rolling and pressing (tapes II and III) does not introduce defects as deformation by drawing and rolling does (tape I), but the texture and local j_c for the rolled+pressed tapes is not as good as for the drawn+rolled tape.
- The improved intergrain coupling is maybe due to a grain growth (smaller $\Delta 2\theta$) reducing the number of grain boundaries.

6.5 Conclusions

From the *in-situ* studies information on strain relaxation, grain growth, phase transformations, stoichiometric changes and texture development is obtained. The reaction route of the 2212→2223 transformation involving primarily $(Ca,Sr)_2PbO_4$, $(Ca,Sr)_2CuO_3$ and a liquid phase is established. The transformation kinetics and lack of finite-size broadening of the 2212 peaks helps to distinguish between various models proposed for the detailed phase transformation mechanism. The texture is seen to develop almost exclusively in the 2212 phase, and the 2223 texture depends on the final 2212 texture obtained. This opens for the possibility to optimize texture and phase transformation independently, to some degree. It is worth emphasizing that all studies are performed on "real" tapes taken directly from the production line - no special sample treatment is required when high-energy photons are at hand.

The importance of various current limiting parameters is identified by combining direct space and reciprocal space investigations, using magneto-optical imaging and diffraction studies. Mechanical defects are detrimental to the performance of the tape, and the mechanical deformation procedure giving the optimum texture and local j_c may also be one introducing a large number of defects in the BSCCO core.

Today the BSCCO/Ag tapes have already obtained an impressively high quality, and with the continuous increase of knowledge of all aspects of the BSCCO

system and the continuous efforts put into further development, the question is only whether superconducting wires will be a part of everyday life soon or even sooner.

The low Flux-Line-Lattice melting temperature and anisotropic nature of BSCCO makes it a less obvious candidate for use in applications involving high magnetic fields at liquid nitrogen temperatures. The challenge is formidable, and it will require an inventive combination of the knowledge of the superconductive and materials properties of BSCCO before high-field applications will appear. But to quote the discoverer of the BSCCO system Hiroshi Maeda [86]:

"In the near future, we shall be obligated to develop some useful applications, such as high-field superconducting magnets operated in liquid nitrogen, because the excellent Bi-oxide superconductors have been presented to all in the world by God on Christmas Eve."

7 Summary and concluding remarks

Oxygen ordering in $ReBa_2Cu_3O_{6+x}$

The oxygen ordering in the $ReBa_2Cu_3O_{6+x}$ system has fundamental importance for the superconducting properties and is at the same time a fascinating topic in its own respect. The ordering is a dynamical process, and the appearance of the structural phase diagram is closely related to the kinetics of the ordering process. For $YBa_2Cu_3O_{6+x}$ we have established the existence of five different types of orthorhombic superstructures: ortho-I,II,III,V and VIII. Of these the ortho-V structure is a mixed phase coexisting with ortho-II, and ortho-VIII can be described as a transition phase between ortho-V and ortho-III. The stability limits with respect to oxygen concentration and temperature is found, and the results are summarized in a phase diagram. The experimental findings are supported by Monte Carlo simulations incorporating the ASYNNNI model. We see no indications of other superstructures as e.g. the $2\sqrt{2}a \times 2\sqrt{2}a \times c$ or herringbone type that have tentatively been ascribed to oxygen ordering. I dare to say that with Paper 1 the canonical orthorhombic phase diagram for YBCO has now been established. In theory other superstructures could exist at lower temperatures, but here the diffusion kinetics are so slow that it will require exceedingly troublesome preparation procedures to obtain such superstructures.

The existence of the anomalous tetragonal $x = 0.62$ YBCO crystal is a completely unexpected feature. We have shown that superconductivity can exist in tetragonal YBCO, but the origin of both the anomalous structural behavior and the charge transfer in the crystal is a mystery. The studies of the tetragonal $x = 0.62$ crystal is an example of the strength of combining different experimental analysis techniques; measurements of only structure or superconductivity would be marginally interesting, but the magneto-optical imaging elegantly and unambiguously shows that the superconductivity in this sample is truly a bulk phenomenon.

The oxygen superstructures in Nd-123 with $x = 0.5$ is a very nice complementary study to the YBCO phase diagram. We demonstrate by numerical calculations that a mixture of three oxygen configurations is required to account for the observed diffraction pattern. Two of the configurations are interlocked in an alternating sequence stacked along the c-axis. The structures found cannot give rise to charge transfer, showing why a higher oxygen content is needed in Nd-123 than in YBCO to make the compound superconducting. This further emphasizes the importance of the oxygen ordering for the charge transfer. It is interesting to note that for both YBCO and Nd-123 the superstructure formation is of a three-dimensional nature only around $x = 0.5$. The other orthorhombic superstructures in YBCO are all 2D-like, and no superstructures are observed at higher or lower oxygen content in Nd-123.

The dynamical studies of the ortho-II phase confirm that dynamical scaling applies, i.e., The volume of the ortho-II phase is constant at a given temperature but the correlation lengths increase with time while maintaining the anisotropy ratio. These studies are performed at elevated temperatures, since the kinetics slow down dramatically around room temperature. But if we assume that dynamical scaling also applies to samples quenched to cryogenic temperatures the implications for the charge ordering mechanism is intriguing: several studies have shown that T_c scales with the oxygen ordering [36, 37] when quenched samples are annealed at room temperature between measurements of T_c. According to the

dynamical scaling the ortho-II volume is constant, and T_c does therefore not scale with the amount of ortho-II phase present but with the correlation length of the ortho-II. This points to the charge transfer mechanism being a collective (coherent) effect, much like the condensation of Cooper pairs into the superconducting state is a collective phenomenon.

Flux turbulence in $ReBa_2Cu_3O_{6+x}$

Flux turbulence is seen in Nd-123 and underdoped YBCO single crystals. This type of chaotic flux interactions has previously only been reported for optimally doped YBCO samples. A high chemical purity of the crystals is necessary for the flux turbulence to exist, while a number of other characteristic parameters like the critical current density j_c, the anisotropy γ and type of oxygen superstructure are at most marginally important for the turbulent behavior. This indicates that the chaotic flux behavior is a relatively common phenomenon in the Re-123 system. We also see indications that for a sample in the turbulent state the field shielding is incomplete, in contradiction to the Bean critical state model.

Stripe phases

We have demonstrated the strength of hard x-ray diffraction for studies of charge stripe ordering in the nickelates and cuprates. The x-ray experiments confirm the neutron diffraction results for the cuprate sample with 1/8 hole doping and additional information of the stripe symmetry is obtained with the observation of next-nearest-neighbor layer correlations in the l-scans. Charge-order reflections in the $x = 0.15$ sample, which were at the detection limit for neutron investigations are clearly observed with hard x-rays. The importance of a proper scattering configuration in which the reflected intensity is integrated along c is demonstrated, as the phonon contribution dominates when c is mounted in the horizontal scattering plane. In a sample with 1/8 Sr doping where La is substituted by Eu instead of Nd, we observe surprisingly strong reflections close to the expected charge-ordering positions in reciprocal space. The reflections are essentially temperature independent, which is in contradiction to the stripe model. It is unknown whether the origin of these strong reflections is the same as for the reflections ascribed to charge-ordering in the Nd-substituted samples.

BSCCO/Ag tapes

For the Ag-clad BSCCO tapes the *in-situ* measurements yield new information of the transformation path, the secondary phases involved in the solid state reactions, the transformation dynamics, restraints on possible transformation models and texture development. Several of the secondary phases involved in the transformation of 2212 to 2223 only appear during the annealing, as e.g. the liquid phase and the crystallization of the 3321 and $(Ca,Sr)_2CuO_3$ phases. The fact that the 2212 linewidth is constant throughout the transformation procedure points to a transformation process in which the 2212 grains transform very fast, but only a few at a time. This is hard to reconcile with the intercalation mechanism being responsible for the main transformation, but points more in the direction of a nucleation-and-growth mechanism. The texture improvement mainly takes place for the 2212 phase with a substantial part of the improvement happening before the phase transformation begins, and the final 2212 and 2223 textures are almost identical. Thus, one might attempt to achieve a good 2223 texture through an optimization of the 2212 texture before the 2212 to 2223 transformation begins.

Combined magneto-optical imaging and x-ray studies show that defect structures in form of weak-link cracks induced by the mechanical deformation have great importance as a current limiting parameter. Deformation by rolling and uniaxial pressing gives essentially no defect structures, but gives a poorer texture and lower j_c on a local scale than deformation by drawing and rolling. The main importance of a second thermomechanical processing step is to improve the grain coupling and thereby enhance the intergrain j_c, while the intragrain j_c governed by flux pinning is hardly affected.

Concluding remarks

The structural aspects of the high-T_c superconductors studied in this thesis are of widely different origin. The oxygen superstructures in $YBa_2Cu_3O_{6+x}$, the electronic phase separation in the lanthanum cuprates and the texture of the BSCCO tapes represent structural properties that all strongly influence the superconductivity on different scales, ranging from weak electronic and magnetic interactions to an alignment of macroscopic crystallites. Both basal studies and applied research must take the very special anisotropic nature of the cuprates into account, in order to understand and optimize the superconducting behavior.

Perhaps the title of this thesis should have been "Structural, Superconducting and *Non-superconducting* Properties of High-T_c Superconductors" since some of the most interesting samples I have studied are displaying reduced superconductivity or no superconductivity at all, i.e. the $NdBa_2Cu_3O_{6.5}$ crystals, the 1/8 suppression of superconductivity in the lanthanum cuprates and anomalously suppressed superconductivity in the tetragonal $x = 0.62$ YBCO sample. The basic goal in high-T_c research is to understand why the strange cuprates are superconducting at all, and how to use this knowledge to perhaps create new materials with improved superconducting properties. So far I have helped demonstrating why some of the cuprates are lousy superconductors, and I hope that this will be a step on the road.

Publications

Chronological list of publications related to my Ph.D. work.

Regular papers

H.F. Poulsen, S. Garbe, T. Lorentzen, D.J. Jensen, F.W. Poulsen, N.H. Andersen, T. Frello, R. Feidenhansl & H. Graafsma. Applications of high-energy synchrotron radiation for structural studies of polycrystalline materials. *J. Synchrotron Radiation* **4**, 147-154 (1997).

A. Vigliante, M. von Zimmermann, J.R. Schneider, T. Frello, N.H. Andersen, J. Madsen, D.J. Buttrey, D. Gibbs & J.M. Tranquada. Detection of charge scattering associated with stripe order in $La_{1.775}Sr_{0.225}NiO_4$ by hard X-ray diffraction. *Phys. Rev. B* **56**, 8248-8251 (1997).

M. von Zimmermann, A. Vigliante, T. Niemöller, N. Ichikawa, T. Frello, J. Madsen, P. Wochner, S. Uchida, N.H. Andersen, J.M. Tranquada, D. Gibbs & J.R. Schneider. Hard-X-ray diffraction study of charge stripe order in $La_{1.48}Nd_{0.4}Sr_{0.12}CuO_4$. *Europhys. Lett.* **41**, 629-634 (1998).

H.F. Poulsen, T. Frello, N.H. Andersen, M.D. Bentzon & M. von Zimmermann. Structural studies of BSCCO/Ag-tapes by high-energy synchrotron X-ray diffraction. *Physica C* **298**, 265-278 (1998).

M. Käll, M. Osada, M. Kakihana, L. Börjesson, T. Frello, J. Madsen, N.H. Andersen, R. Liang, P. Dosanjh, & W.N. Hardy. CuO-chain Raman scattering and photoinduced metastability in $YBa_2Cu_3O_x$. *Phys. Rev. B, Rapid Communications* **57**, 14072-14075 (1998).

M.R. Koblischka, T. Higuchi, S.I. Yoo, M. Murakami, T. Frello, M. Baziljevich, T.H. Johansen, T. Wolf & P. Diko. Magnetic measurements in $NdBa_2Cu_3O_{7-\delta}$ single crystals: Magnetization, flux pinning and creep. *Applied Superconductivity* **6**, 225-234 (1998).

T. Frello, M. Baziljevich, T.H. Johansen, N.H. Andersen, T. Wolf & M.R. Koblischka. Flux turbulence in $NdBa_2Cu_3O_{6+x}$ and underdoped $YBa_2Cu_3O_{6+x}$ single crystals. *Phys. Rev. B, Rapid Communications* **59**, R6639-R6642 (1999).

T. Niemöller, M. von Zimmermann, S. Uhlenbruck, O. Friedt, B. Büchner, T. Frello, N.H. Andersen, P. Berthet, L. Pinsard, A.M. De Léon-Guevara, A. Revcolevschi & J.R. Schneider. The charge ordered phase in $La_{1-x}Sr_xMnO_3$ studied by means of high energy X-ray diffraction. *Eur. Phys. J. B* **8**, 5-8 (1999).

H.F. Poulsen, L. Gottschalck Andersen, T. Frello, S. Pratontep, N.H. Andersen, S. Garbe, J. Madsen, A. Abrahamsen, M.D. Bentzon & M. von Zimmermann. In-situ study of equilibrium phenomena and kinetics in a BiSCCO/Ag tape. *Physica C* **315**, 254-262 (1999).

T. Frello, H.F. Poulsen, L. Gottschalck Andersen, N.H. Andersen, M.D. Bentzon & J. Schmidberger. An in-situ study of the annealing behaviour of BiSCCO/Ag tapes. *Supercond. Sci. Technol.* **12**, 293-300 (1999).

Conference proceedings

T. Frello, N.H. Andersen, J. Madsen, M. Käll, M. von Zimmermann, O. Schmidt, H.F. Poulsen, J.R. Schneider & T. Wolf. Dynamics of oxygen ordering in $YBa_2Cu_3O_{6+x}$ studied by neutron and high-energy synchrotron X-ray diffraction. *Physica C* **282**, 1089-1090 (1997).

M. von Zimmermann, A. Vigliante, T. Frello, J. Madsen, D.J. Buttrey, N.H. Andersen, J.R. Schneider, D. Gibbs & J.M. Tranquada. X-ray scattering study of charge scattering associated with stripe order in $La_{1.775}Sr_{0.225}NiO_4$. *Journal of Superconductivity* **10**, 447-450 (1997).

T. Frello, H.F. Poulsen, N.H. Andersen, A. Abrahamsen, S Garbe, M.D. Bentzon & M. von Zimmermann. Annealing of Ag-clad BiSCCO tapes studied in-situ by high-energy synchrotron X-ray diffraction. *Applied Superconductivity 1997, Inst. Phys. Conf. Ser.* **158**, 1363-1366 (1997).

J.-C. Grivel, H.F. Poulsen, L.Gottschalck Andersen, T. Frello, N.H. Andersen, E. Giannini, P.D. Grindatto & R. Flükiger. Investigations on the formation mechanism of the Bi(2223) phase in bulk samples and Ag-sheathed tapes. *Program and extended abstracts. 1998 international workshop on superconductivity*, Okinawa, Japan (International Superconductivity Technology Center (ISTEC)), 50-53 (1998).

M. Käll, M. Osada, J. Bäckstrøm, M. Kakihana, L. Börjesson, T. Frello, J. Madsen, N.H. Andersen, R. Liang, P. Dosanjh & W.N. Hardy. Resonance Raman scattering as a probe of oxygen dynamics in $YBa_2Cu_3O_{6+x}$ *J. Phys. Chem. Sol.* **59**, 1988-1990 (1998).

N.H. Andersen, M. von Zimmermann, T. Frello, M. Käll, D. Mønster, P.-A. Lindgård, J. Madsen, T. Niemöller, H.F. Poulsen, O. Schmidt, J.R. Schneider, T. Wolf, P. Dosanjh, R. Liang & W.N. Hardy. Superstructure formation and the structural phase diagram of $YBa_2Cu_3O_{6+x}$. *Physica C* **317-318**, 259-269 (1999).

L. Gottschalck Andersen, H.F. Poulsen, T. Frello, N.H. Andersen & M. von Zimmermann. Cooling behavior of BSCCO/Ag tapes. *IEEE Trans. Appl. Superconduct.* **9**, 2758-2761 (1999)

J.K.S. Christiansen, N.H. Andersen & T. Frello. Pinning of magnetic flux lines in Y-Ba-Cu-O superconductors by neutron irradiation and chemical route. *IEEE Trans. Appl. Superconduct.* **9**, 2304-2307 (1999).

Papers in other fields

O.K. Andersen, T. Frello & E. Veje. Photoinduced synthesis of porous silicon without anodization. *J. Appl. Phys.* **78**, 6189-6192 (1995).

T. Frello, O. Leistiko & E. Veje. Observation of time-varying photoconductivity and persistent photoconductivity in porous silicon *J. Appl. Phys.* **79**, 1027-1031 (1996).

T. Frello & E. Veje. Time-varying phenomena in the photoelectric properties of porous silicon. *J. Appl. Phys.* **81**, 6978-6985 (1997).

Acknowledgements

The results obtained during my three years as Ph.D. student do certainly not represent the work of one man only. I have had the great fortune of being part of the very active and internationally minded high-T_c group here at Risø National Laboratory. First of all I must thank my supervisor senior scientist Niels Hessel Andersen here at the Condensed Matter Physics and Chemistry Department and senior scientist Henning Friis Poulsen from the Materials Research Department. It has been a challenging and immensely rewarding experience to work with some of the leading experts in the field of high-T_c superconductivity and high-energy synchrotron x-ray diffraction, and both on a scientific and on a personal basis it has been a pleasure. The interaction with the other students and Post-Docs in the high-T_c group at Risø has always been enjoyable and worth-while experience and I would like to thank Asger Abrahamsen, Mikael Käll, Jesper Madsen, and Ole Schmidt for a very fruitful collaboration. From the Materials Research Department I would like to thank the other people involved in the BSCCO tape project: Lotte Gottschalck Andersen (with whom I have also shared some very intense roller-coaster rides in Disneyland), Carsten Bagger, Stephan Garbe, Jean-Claude Grivel, Bruno Kindl and Yi-Lin Liu.

The project on the superconducting tapes would of course never have existed without the bold decision of NKT Research Center A/S to begin the development of high-T_c wires in Denmark. From these efforts the company Nordic Superconductor Technologies has emerged and I would like to thank the researchers here for the inspiring collaboration on the tape project, in particular Michael Deluran Bentzon, Per Vase, Peter Bodin, Zenghe Han and Wei Guo Wang.

During the long shifts at odd working hours at the HASYLAB synchrotron it can be hard to suppress the darkest sides of human nature. Nevertheless the beamtimes with Martin von Zimmermann, Thomas Niemöller, Heiko Hünnefeld, and Noryia Ichikawa have always been an (almost) exclusively pleasant experience. In particular, significant part of my knowledge of single crystal diffraction comes from working with Martin, and I have had great benefit from the discussions with Thomas on the stripe phases. The success of the hard x-ray studies owes much to the personal involvement of Prof. Jochen R. Schneider in both the instrumental development of beamline BW5 and the scientific outcome. His involvement in especially the studies of oxygen ordering and the stripe phases has been invaluable.

A big thanks goes to Tom Henning Johansen and Michael Baziljevich for providing not only liquid helium, magneto-optical indicator films and accommodation, but also a very friendly and pleasant atmosphere during my stay at the University of Oslo. During my stay I also much enjoyed conversations with Michael R. Koblischka on the fascinating topics of flux penetration, flux pinning and model trains. I am grateful for the hospitality of Assunta "Titti" Vigliante, Peter Wochner, Doon Gibbs and John Tranquada during my visit to Brookhaven National Laboratory.

The skillful and dedicated technicians at Risø have made it a pleasure to be an experimentalist. It would be highly unfair to mention someone in particular, but I'll do it anyway: a special thanks to Steen Nielsen and Torben Kjær from *Spacelab*; the success of the *in-situ* experiments at HASYLAB depended much on their clever modifications of the furnaces that were used. I much appreciated being involved in the project of improvement of flux pinning in melt textured YBCO

by neutron irradiation with Jens Christiansen from the Technical University of Denmark. The high-quality single crystals that were the backbone of the success of the oxygen ordering studies were supplied from Thomas Wolf, Karlsruhe and R.X. Liang, P. Dosanjh and W.N. Hardy from University of British Columbia. And thanks to Morten Ring Eskildsen for some very useful LaTeX tips and handy style files for the writing of this thesis.

I am most grateful for the Ph.D. scholarship granted by the Danish Technical Research Council (under grant number 28813). The financial support from DANSYNC covering travel expenses for the synchrotron studies is also highly appreciated.

I sincerely thank all my colleagues for the sympathy and understanding they showed when my younger brother Simon unexpectedly died of a heart attack in August 1998. And last but in no way least the biggest thanks to my loving parents Otto and Stence for their unlimited support during my studies.

References

[1] Neil W Ashcroft & N David Mermin. *Solid State Physics*. W B Saunders Company, (1976).

[2] J G Bednorz & K A Müller. Possible High T_c Superconductivity in the Ba-La-Cu-O System. *Z. Phys. B* **64**, 189–193 (1986).

[3] J Bardeen, L N Cooper & J R Schrieffer. Theory of Superconductivity. *Phys. Rev.* **108**(5), 1175–1204 (1957).

[4] V D Shabetnik, S Yu Butuzov & V I Plaksii. High-temperature superconducting compound $YBa_2Cu_3Se_7$ with $T_c = 371$ K. *Tech. Phys. Lett.* **21**(5), 382–384 (1995). [Pis'ma Zh. Fiz. **21**, 67-71 (1995)].

[5] J B Torrance, A Bezinge, A I Nazzal, T C Huang, S S P Parkin, D T Keane, S J LaPlaca, P M Horn & G A Held. Properties that change as superconductivity disappears at high-doping concentrations in $La_{2-x}Sr_xCuO_4$. *Phys. Rev. B* **40**(13), 8872–8877 (1989).

[6] M R Eskildsen. *Small Angle Neutron Scattering Studies of the Flux Line Lattices in the Borocarbide Superconductors*. Ph.d. thesis, Risø National Laboratory, DK-4000 Roskilde, Denmark, (1998).

[7] V L Ginzburg & L D Landau. *Zh. Eksp. Theor. Fiz.* **20**, 1064 (1950).

[8] A A Abrikosov. On the Magnetic Properties of Superconductors of the Second Kind. *Soviet Phys. JETP* **5**, 1174 (1957). [*Zh. Eksp. Theor. Fiz.* **32**, 1442 (1957)].

[9] C P Bean. Magnetization of hard superconductors. *Phys. Rev. Lett* **8**(6), 250–253 (1962).

[10] C P Bean. Magnetization of High-Field Superconductors. *Rev. Mod. Phys.* **36**, 31–39 (1964).

[11] J E Evetts. *Concice Encyclopaedia of Magnetic and Superconducting Materials*. Ed. Pergamon Press Ltd., (1992).

[12] V I Grebennikov & V Ye Naysh. Diffraction in randomized structures and space correlation functions. *Phys. Met. Metall.* **71**(1), 124–138 (1991).

[13] R Bouchard, D Hupfeld, T Lippmann, J Neuefeind, H-B Neumann, H F Poulsen, U Rütt, T Schmidt, J R Schneider, J Süssenbach & M von Zimmermann. A Triple-Crystal Diffractometer for High-Energy Synchrotron Radiation at the HASYLAB High-Field Wiggler Beamline BW5. *J. Synchrotron Rad.* **5**, 90–101 (1998).

[14] H-B Neumann, U Rütt, R Bouchard, J R Schneider & H Nagasawa. The resolution function of a triple-crystal diffractometer for high energy synchrotron radiation in nondispersive Laue geometry. *J. Appl. Cryst.* **27**, 1030–1038 (1994).

[15] U Rütt, H-B Neumann, H F Poulsen & J R Schneider. The resolution function of a triple-crystal diffractometer for high energy synchrotron radiation. II. Dispersive Laue geometry. *J. Appl. Cryst.* **28**, 729–737 (1995).

[16] H-B Neumann, J R Schneider, J Süßenbach, S R Stock & Z U Rek. Si-$TaSi_2$ in situ composites: a new monochromator material for hard X-rays. *Nucl. Instrum. Methods Phys. Res. A* **372**, 551–555 (1996).

[17] N H Andersen, B Lebech & H F Poulsen. The structural phase diagram and oxygen equilibrium partial pressure of $YBa_2Cu_3O_{6+x}$ studied by neutron powder diffraction and gas volumetry. *Physica C* **172**, 31–42 (1990).

[18] P Schleger, W N Hardy & B X Yang. Thermodynamics of oxygen in $Y_1Ba_2Cu_3O_x$ between 450°C and 650°C. *Physica C* **176**, 261–273 (1991).

[19] H Casalta, P Schleger, P Harris, B Lebech, N H Andersen, R X Liang, P Dosanjh & W N Hardy. Neutron-scattering determination of the structural parameters versus oxygen content of $YBa_2Cu_3O_{6+x}$ single crystals. *Physica C* **258**(3-4), 321–330 (1996).

[20] Michael Baziljevich. *Investigation of Magnetic Flux Behavior in $YBa_2Cu_3O_{7-\delta}$ Thin Films and Single Crystals Using Magneto-Optic Imaging.* Ph.d. thesis, University of Oslo, Department of Physics, P.O. Box 1048, Blindern, 0316 Oslo, Norway, (1996).

[21] M R Koblischka & R J Wijngaarden. Magneto-optical investigations of superconductors. *Supercond. Sci. Technol.* **8**, 199–213 (1995).

[22] Petriina Paturi. *Laser ablation of superconducting YBCO films from nanopowder target and preparation of mesoscopic YBCO/Au interfaces.* Ph.d. thesis, University of Turku, Department of Physics, 20014 Turku, Finland, (1998).

[23] T H Johansen, M Baziljevich, H Bratsberg, Y Galperin, P E Lindelof, Y shen & P Vase. Direct observation of the current distribution in thin superconducting strips using magneto-optic imaging. *Phys. Rev. B* **54**(22), 16264–16269 (1996).

[24] R J Wijngaarden, K Heeck, H J W Spoelder, R Surdeanu & R Griessen. Fast determination of 2D current patterns in flat conductors from measurement of their magnetic field. *Physica C* **295**, 177–185 (1998).

[25] Ch Jooss, R Warthmann, A Forkl & H Kronmüller. High-resolution magneto-optical imaging of critical currents in $YBa_2Cu_3O_{7-\delta}$ thin films. *Physica c* **299**, 215–230 (1998).

[26] M K Wu, J R Ashburn, C J Torng, P H Hor, R L Meng, L Gao, Z J Huang, Y Q Wang & C W Chu. Superconductivity at 93 K in a New Mixed-Phase Y-Ba-Cu-O Compound System at Ambient Pressure. *Phys. Rev. Lett.* **58**(9), 908–910 (1987).

[27] H F Poulsen, N H Andersen, J V Andersen, H Bohr & O G Mouritsen. Relation between superconducting transition temperature and oxygen ordering in $YBa_2Cu_3O_{6+x}$. *Letter to Nature* **349**, 594–596 (1991).

[28] C Chaillout, M A Alario-Franco, J J Capponi, J Chenavas, J L Hodeau & M Marezio. Oxygen-vacancy ordering in the $Ba_2YCu_3O_{7-x}$ ($0 \leq x \leq 1$) superconducting system. *Phys. Rev. B* **36**(13), 7118–7120 (1987).

[29] G J McIntyre, A Renault & G Collin. Domain and crystal structure of superconducting $Ba_2YCu_3O_{8-\delta}$ at 40 and 100 K by single-crystal neutron diffraction. *Phys. Rev. B* **37**(10), 5148–5157 (1988).

[30] G Uimin & J Rossat-Mignod. Role of Cu-O chains in the charge transfer mechanism in $YBa_2Cu_3O_{6+x}$. *Physica C* **199**, 251–261 (1992).

[31] D de Fontaine, L T Wille & S C Moss. Stability analysis of special-point ordering in the basal plane in $YBa_2Cu_3O_{7-\delta}$. *Phys. Rev. B* **36**(10), 5709–5712 (1987).

[32] N H Andersen, M von Zimmermann, T Frello, M Käll, D Mønster, P-A Lindgård, J Madsen, T Niemöller, H F Poulsen, O Schmidt, J R Schneider, Th Wolf, P Dosanjh, R Liang & W N Hardy. Superstructure formation and the structural phase diagram of $YBa_2Cu_3O_{6+x}$. *Physica C* **317-318**, 259–269 (1999).

[33] Ruixing Liang, P Dosanjh, D A Bonn, D J Baar, J F Carolan & W N Hardy. Growth and properties of superconducting YBCO single crystals. *Physica C* **195**, 51–58 (1992).

[34] Th Wolf, W Goldacker, B Obst, G Roth & R Flükiger. Growth of Thick $YBa_2Cu_3O_{7-x}$ single crystals from Al_2O_3 crucibles. *J. Cryst. Growth* **96**, 1010–1018 (1989).

[35] R Beyers, B T Ahn, G Gorman, V Y Lee, S S P Parkin, M L Ramirez, K P Roche, J E Vazquez, T M Gür & R A Huggins. Oxygen ordering, phase separation and the 60-K and 90-K plateaus in $YBa_2Cu_3O_x$. *Nature* **340**, 619–621 (1989).

[36] J D Jorgensen, Shiyou Pei, P Lightfoot, Hao Shi, A P Paulikas & B W Veal. Time-dependent structural phenomena at room temperature in quenched $YBa_2Cu_3O_{6.41}$. *Physica C* **167**, 571–578 (1990).

[37] J Madsen, N H Andersen, M von Zimmermann & T Wolf. Evidence for Enhancement of T_c by Ortho-II Ordering in $YBa_2Cu_3O_{6.5}$. Annual Progress Report of the Department of Solid State Physics 1 January - 31 December 1996, (1997). Risø Report R-933(EN).

[38] V N Topnikov, V I Simonov, L A Muradyan, V N Molchanov, A V Zvarykina, V N Laukhin, L P Rozenberg, R P Shibaeva & B Yagubskii. Structure of tetragonal superconducting $YBa_2Cu_{2.862}O_{6.62}$ single crystals with $T_c \approx$50K. *JETP Lett.* **46**(11), 577–580 (1988).

[39] M Murakami, Sang-Im Yoo, T Higuchi, N Sakai, J Weltz, N Koshizuka & S Tanaka. Flux pinning in melt-grown $NdBa_2Cu_3O_y$ and $SmBa_2Cu_3O_y$ superconductors. *Jpn. J. Appl. Phys.* **44**(5B), L715–L717 (1994).

[40] H Lütgemeier, S Schmenn, P Meuffels, O Storz, R Schöllhorn, Ch Niedermayer, I Heinmaa & Yu Baikov. A different type of oxygen order in $REBa_2Cu_3O_{6+x}$ HT_c superconductors with different RE ionic radii. *Physica C* **267**, 191–203 (1996).

[41] Th Wolf, A-C Bornarel, H Küpfer, R. Meier-Hirmer & B Obst. High irreversibility fields and current densities in $NdBa_2Cu_3O_{7-\delta}$ single crystals and melt-textured samples. *Phys. Rev. B* **56**, 6308–6319 (1997).

[42] T B Lindemer, E D Specht, P M Martin & M L Flitcroft. Nonstoichiometry, decomposition and T_c of $Nd_{1+z}Ba_{2-z}Cu_3O_y$. *Physica C* **255**(1-2), 65–75 (1995).

[43] A Bertinotti, J Hammann, D Luzet & E Vincent. Structure of a new type of satellite phase in $YBa_2Cu_3O_{7-\delta}$. *Physica C* **160**, 227–234 (1989).

[44] F Yakhou, V Plakhty, A Stratilatov, P Burlet, J P Lauriat, E Elkaim, J Y Henry, M Vlasov & S Moshkin. The $2\sqrt{2}a_0 \times \sqrt{2}b_0 \times c_0$ herringbone phase of $YBa_2Cu_3O_{6+x}$. No oxygen ordering but an alien oxide, $BaCu_3O_4$. *Physica C* **261**, 315–322 (1996).

[45] A Stratilatov, V Plakhty, Yu Chernenkov & V Fedorov. The structure of the ortho-III phase of $YBa_2Cu_3O_{6+x}$ by x-ray scattering. *Phys. Lett. A* **180**(1,2), 137–140 (1993).

[46] E Straube, D Hohlwein & F Kubanek. The ortho-II superstructure of $YBa_2Cu_3O_{6.5}$ - temperature behaviour, oxygen ordering and T_c. *Physica C* **295**, 1–14 (1998).

[47] M V Indenbom, T Schuster, M R Koblischka, A Forkl, H Kronmüller, L A Dorosinskii, V K Vlasko-Vlasov, A A Polyanskii, R L Prozorov & V I Nikitendo. Study of Flux Distributions in High-T_c Single Crystals and Thin Films Using Magneto-Optic Techniques. *Physica C* **209**(1-3), 259–262 (1993).

[48] V K Vlasko-Vlasov, V I Nikitendo, A A Polyanskii, G W Crabtree, U Welp & B W Beal. Macroturbulence in High-T_c superconductors. *Physica C* **222**(3-4), 361–366 (1994).

[49] M R Koblischka, T H Johansen, M Baziljevich, H Hauglin, H Bratsberg & B Y Shapiro. Turbulent relaxation in the vortex lattice. *Europhys. Lett.* **41**(4), 419–424 (1998).

[50] T H Johansen & H Bratsberg. Critical-state magnetization of type-II superconductors in rectangular slab and cylinder geometries. *J. Appl. Phys.* **77**(8), 3945–3952 (1995).

[51] M R Koblischka, A J J van Dalen, T Higuchi, K Sawada, S I Yoo & M Murakami. Observation of multiple peaks in the magnetization curves of $NdBa_2Cu_3O_7$ single crystals. *Phys. Rev. B* **54**(10), R6893–R6896 (1996).

[52] T Ishida, K Kitamura, K Okuda, A I Rykov & S Tajima. Anisotropy of Underdoped $YBa_2Cu_3O_{6.5}$ Single Crystal. To be published in Advances in Superconductivity Vol XI (Springer), (1999).

[53] A R Moodenbaugh, Youwen Xu, M Suenaga, T J Folkerts & R N Shelton. Superconducting Properties of $La_{2-x}Ba_xCuO_4$. *Phys. Rev. B* **38**, 4596–4600 (1988).

[54] Y Maeno, N Kakehi, M Kato & T Fujita. Effects of Th Doping on Structural and Superconductive Properties of $La_{2-x}Ba_xCuO_4$. *Phys. Rev. B* **44**, 7753–7756 (1991).

[55] M K Crawford, R L Harlow, E M McCarron, W E Farneth, J D Axe, H Chou & Q Huang. Lattice instabilities and the effect of copper-oxygen-sheet distortions on superconductivity in doped La_2CuO_4. *Phys. Rev. B* **44**(14), 7749–7752 (1991).

[56] A R Moodenbaugh, L H Lewis & S Soman. Superconductivity of polycrystalline $La_{2-x-y}Nd_ySr_xCuO_4$. *Physica C* **290**, 98–104 (1997).

[57] J D Axe, A H Moudden, D Hohlwein, D E Cox, K M Mohanty & A R Moodenbaugh. Structural Phase Transformations and Superconductivity in $La_{2-x}Ba_xCuO_4$. *Phys. Rev. Lett.* **62**(23), 2751–2754 (1989).

[58] R M Fleming, B Batlogg, R J Cava & E A Rietman. Temperature and composition dependence of the tetragonal-orthorhombic distortion in $La_{2-x}Sr_xCuO_{4-d}$. *Phys. Rev. B* **35**(13), 7191–7194 (1987). Rapid Communication.

[59] M R Norman, G J McMullan, D L Novikov & A J Freeman. Effect of structure on the electronic density of states of doped lanthanum cuprates. *Phys. Rev. B* **48**(13), 9935–9937 (1993).

[60] T R Thurston, P M Gehring, G Shirane, J R Birgeneau, M A Kastner, Y Endoh, M Matsuda, K Yamada, H Kojima & I Tanaka. Low-energy spin excitations in superconducting $La_{1.85}Sr_{0.15}CuO_4$. *Phys. Rev. B* **46**(14), 9128–9131 (1992).

[61] J M Tranquada, D J Buttrey, V Sachan & J E Lorenzo. Simultaneous ordering of holes and spins in $La_2NiO_{4.125}$. *Phys. Rev. Lett.* **73**(7), 1003–1006 (1994).

[62] J M Tranquada, J E Lorenzo, D J Buttrey & V Sachan. Cooperative ordering of holes and spins in $La_2NiO_{4.125}$. *Phys. Rev. B* **52**(5), 3581–3595 (1995).

[63] J M Tranquada, D J Buttrey & V Sachan. Incommensurate stripe order in $La_{2-x}Sr_2NiO_4$ with x=0.225. *Phys. Rev. B* **54**, 12318–12323 (1996).

[64] J M Tranquada, B J Sternlib, J D Axe, Y Nakamura & S Uchida. Evidence for stripe correlations of spins and holes in copper oxide superconductors. *NATURE* **375**, 561–563 (1995).

[65] J M Tranquada, J D Axe, N Ichikawa, Y Nakamura, S Uchida & B Nachumi. Neutron-scattering study of stripe-phase order of holes and spins in $La_{1.48}Nd_{0.4}Sr_{0.12}CuO_4$. *Phys. Rev. B* **54**(10), 7489–7499 (1996).

[66] J M Tranquada. Stripe correlations of spins and holes in cuprates and nickelates. *Ferroelectrics* **177**, 43–57 (1996).

[67] J M Tranquada. Stripe correlations of spins and holes in copper oxide superconductors. *Neutron News* **7**(1), 17–20 (1996).

[68] V J Emery & S A Kivelson. Collective Charge Transport in High Temperature Superconductors. *Physica C* **235-240**, 189–192 (1994).

[69] V J Emery, S A Kivelson & O Zachar. Spin-gap proximity effect mechanism of high-temperature superconductivity. *Phys. Rev. B* **56**(10), 6120–6147 (1997).

[70] J M Tranquada, J D Axe, N Ichikawa, A R Moodenbaugh, Y Nakamura & S Uchida. Coexistence of, and competition between, superconductivity and charge-stripe order in $La_{1.6-x}Nd_{0.4}Sr_xCuO_4$. *Phys. Rev. Lett.* **78**(2), 338–341 (1997).

[71] P Brüesch. *Phonons : Theory and experiments - 2: Experiments and interpretation of experimental results*, volume 65 of *Springer series in solid-state sciences*. Springer, Berlin, (1986).

[72] T Niemöller. Private communication. February (1999).

[73] J M Tranquada, N Ichikawa & K Kakurai. Private communications. (1997). Summary of Experiment at Tokai, Dec. 1997.

[74] S Horiuchi & E Takayama-Muromachi. *Crystal Structure*, chapter 2, 7–32. Volume 6 of *Applied physics* [86] (1996).

[75] V I Simonov, L A Muradynan, R A Tamazyan, O K Mel'nikov, A B Bykov & B K Vaishtein. Ordering of Sr atoms and loss of superconductivity in $(La,Sr)_2CuO_{4-\delta}$ crystals. *JETP Lett.* **48**(5), 323–326 (1988).

[76] V I Simonov, L A Muradynan, R A Tamazyan, V V Osiko, V M Tatarintsev & K Gamayumov. Distribution of Sr atoms in single crystals of $(La,Sr)_2CuO_{4-\delta}$ and the superconducting transition temperature. *Physica C* **169**, 123–132 (1990).

[77] P P Edwards, G B Peacock, J P Hodges, A Asab & I Gameson. *High-T_c Superconductivity 1996: Ten Years after the Discovery*, volume 343 of *NATO ASI Series E: Applied Sciences*. Kluwer Academic Publishers, P.O. Box 17, 3300 AA Dordrecht, The Netherlands, (1997). Proceedings of the NATO Advanced Study Institute on High-T_c Superconductivity 1996. Delphi, Greece 19-31 August 1996.

[78] Gilles Triscone & Alain Junod. *Thermal and Magnetic Properties*, chapter 3, 33–74. Volume 6 of *Applied physics* [86] (1996).

[79] Peter J Majewski. *Phase Equilibria and Crystal Chemistry of the High-Temperature Superconducting Compounds of the System Bi_2O_3-SrO-CaO-CuO*, chapter 6, 129–151. Volume 6 of *Applied physics* [86] (1996).

[80] R Flükiger, G Grasso, B Hensel, M Däumling, R Gladyshevskii, A Jeremie, J-C Grivel & A Perin. *Thermodynamics, Microstructure, and Critical Current Density in Bi,Pb(2223) Tapes*, chapter 15, 319–367. Volume 6 of *Applied physics* [86] (1996).

[81] H-R Wenk, D Chateigner, M Pernet, J Bingert, E Hellstrom & B Ouladdiaf. Texture analysis of Bi-2212 and 2223 tapes and wires by neutron diffraction. *Physica C* **272**, 1–12 (1996).

[82] E Giannini, E Bellingeri, R Passerini & R Flükiger. Direct observation of the Bi,Pb(2223) phase formation inside Ag-sheathed tapes and quantitative secondary phase analysis by means of in situ high-temperature neutron diffraction. *Physica C* **315**, 185–197 (1999).

[83] J-C Grivel & R Flükiger. Formation mechanism of the Pb free $Bi_2Sr_2Ca_2Cu_3O_{10}$ phase. *Supercond. Sci. Technol.* **11**, 288–298 (1998).

[84] F Marti, G Grasso, J-C Grivel & R Flükiger. Effects of the reaction time on various properties of $(Bi,Pb)_2Sr_2Ca_2Cu_3O_x$ tapes. *Supercond. Sci. Technol.* **11**, 485–495 (1998).

[85] W G Wang, J Horvat, B Zeimetz, H K Liu & S X Dou. Effect of $(Bi,Pb)_2Sr_2CuO_6$ phase on critical current density of Ag/$(Bi,Pb)_2Sr_2Ca_2Cu_3O_{10}$ tapes. *Physica C* **291**, 1–7 (1997).

[86] Hiroshi Maeda & Kazumasa Togano. *Bismuth-based high-temperature superconductors*, volume 6 of *Applied physics*. Marcel Dekker, Inc., 270 Madison Avenue, New York, New York 10016, (1996).

List of Papers

The following papers constitute together with the main text the thesis:

Paper 1
Oxygen Ordering Superstructures and Structural Phase Diagram of $YBa_2Cu_3O_{6+x}$ Studied by Hard X-ray Diffraction.

Paper 2
Superstructure formation and the structural phase diagram of $YBa_2Cu_3O_{6+x}$.

Paper 3
Flux turbulence in $NdBa_2Cu_3O_{6+x}$ and underdoped $YBa_2Cu_3O_{6+x}$ single crystals.

Paper 4
Detection of charge scattering associated with stripe order in $La_{1.775}Sr_{0.225}NiO_4$ by hard X-ray diffraction.

Paper 5
Hard-X-ray diffraction study of charge stripe order in $La_{1.48}Nd_{0.4}Sr_{0.12}CuO_4$.

Paper 6
Structural studies of BSCCO/Ag-tapes by high-energy synchrotron X-ray diffraction.

Paper 7
An in-situ study of the annealing behaviour of BiCCO/Ag tapes.

Paper 8
In-situ study of equilibrium phenomena and kinetics in a BiSCCO/Ag tape.

Bibliographic Data Sheet **Risø–R–1086(EN)**

Title and author(s)

Structural and Superconducting Properties of High-T_c Superconductors

Thomas Frello

ISBN	ISSN
87–550–2476–9; 87–550–2477–7 (internet)	0106–2840

Dept. or group

Groups own reg. number(s)

Condensed Matter Physics and Chemistry Department

Project/contract No.

Pages	Tables	Illustrations	References
96	6	58	86

Abstract (Max. 2000 char.)

The report describes experimental investigations of high-T_c materials using high-energy x-ray diffraction, neutron diffraction, magneto-optical imaging, bulk magnetization and gas volumetric sample preparation. The compounds and aspects studied are divided into three categories: In compounds of the type Re-123, (Re=Rare Earth element) the oxygen ordering in the CuO_x basal plane has been studied as a function of oxygen content x and Re-dopant by x-ray diffraction. The orthorhombic phase diagram for $YBa_2Cu_3O_{6+x}$ is established and an anomalous deviation from the $YBa_2Cu_3O_{6+x}$ structural phase diagram is observed for a sample with an oxygen concentration of $x = 0.62$. Three co-existing oxygen configurations are discovered in non-superconducting $NdBa_2Cu_3O_{6.5}$. Magnetic flux front instabilities are observed with magneto-optical imaging in single crystals of near-optimally doped $NdBa_2Cu_3O_{6+x}$ and underdoped $YBa_2Cu_3O_{6+x}$. In nickelates and lanthanum cuprates stripe ordering is investigated by single crystal x-ray diffraction. The results confirm the existence of temperature-dependent charge stripes in nickelates and Nd-doped lanthanates and new information on the stripe symmetry is obtained. In an Eu-doped lanthanate temperature-independent reflections are observed at locations in reciprocal space consistent with the stripe-ordering model. Solid state reactions and texture changes in superconducting BSCCO/Ag tapes for current transport applications are investigated by *in-situ* x-ray diffraction studies during annealing. By combining x-ray diffraction and magneto-optical imaging the influence of mechanical deformation procedures on the superconducting properties are investigated, and the importance of various current limiting parameters is identified.

Descriptors INIS/EDB

Barium oxides; bismuth oxides, copper oxides; critical current; crystal-phase transformations; europium oxides; high-tc superconductors; images; lanthanum oxides; magneto-optical effects; neodymium oxides; neutron diffraction; nickel oxides; strontium oxides; superconductivity; synchrotron radiation; x-ray diffraction; yttrium oxides.

Available on request from:
Information Service Department, Risø National Laboratory
(Afdelingen for Informationsservice, Forskningscenter Risø)
P.O. Box 49, DK–4000 Roskilde, Denmark
Phone (+45) 46 77 46 77, ext. 4004/4005 · Fax (+45) 46 77 40 13
E-mail: infserv@risoe.dk